Politecnico di Torino

M.Sc. AgriTech Engineering

September 2026

Managed Aquifer Recharge planning and modelling to support sustainable groundwater exploitation for irrigation

Supervisors:

Tiziana TOSCO

Rajandrea SETHI

Alessia AMENDOLA

Candidate:

Chanaka Sandakelum PERAMUNE ARACHCHILAGE

Abstract

Managed Aquifer Recharge (MAR) is the intentional recharge of water into aquifers for subsequent environmental benefits, including replenishing depleted aquifers, seasonal storage, and water quality improvement. Agricultural Managed Aquifer Recharge (Ag-MAR) is MAR implemented on actively cultivated agricultural fields, allowing implementation without further allocation of land. In Northern Italy, extensive rice fields traditionally flooded for several weeks during growing seasons - creating unintentional aquifer replenishment - alongside irrigation systems offer significant opportunity for Ag-MAR, especially through winter flooding when surface water is abundant and the paddy fields lie fallow. However, the risk of contaminants — organic and inorganic chemicals, residual agrochemicals, and pathogens — leaching under intense infiltration conditions remains a major environmental concern. Furthermore, clogging of the soil matrix and alterations due to prolonged waterlogging are also remarkable challenges for MAR operations.

The main aim of this study is to determine the hydraulic conductivity (K) and porosity (θ) that govern field infiltration rates, and ultimately the aquifer recharge capacity. Hydraulic conductivity was evaluated through field infiltration experiments in Mortara and Beinette (Northern Italy) alongside laboratory column tests, and the methods were compared to identify suitable approaches for future studies. Porosity was evaluated through inverse modelling by fitting breakthrough curves from laboratory tracer tests. Furthermore, tracer performance and the transport kinetics of the herbicide Imazamox were analysed through laboratory-scale tests for further investigation. Building upon these experimental parameters, numerical and analytical simulations were performed to evaluate the groundwater level response in mounding, and dissipation, as well as the sensitivity of numerical modelling to input parameters obtained by different experimental methods.

Supplementary physical soil properties, including Total Organic Carbon (TOC), and particle size distribution, were analysed on collected disturbed soil samples. Soil column infiltration experiments - including tracer tests with KBr and Rhodamine as well as an Imazamox leaching test - were performed on undisturbed shallow and deep soil cores

extending to a depth of 38.5 cm, followed by inverse numerical modelling using HYDRUS-1D.

Granulometric analysis showed that all soil samples were classified as sandy soil (>96% sand content). Among the field surveys, falling-head tests provided more reliable results than constant-head tests on these sandy soils. Regarding tracer suitability, fluorescein was found to be unsuitable as a tracer for quantitative analysis due to matrix-induced peak wavelength shifts, whereas Rhodamine exhibited non-conservative retardation. Furthermore, Imazamox displayed high transport mobility with zero residual detected in the soil matrix after continuous leaching over an extended period. Corresponding organic carbon-normalized partition coefficients (K_{oc}) were determined as 0.64 cm^3/g (for shallow samples) and 7.84 cm^3/g (for deeper ones). Moreover, Ag-MAR numerical modelling demonstrated that the ponding layer height does not affect the infiltration rate under free drainage lower boundary conditions when the groundwater table is well below and infiltration is governed primarily by less permeable underlying stratigraphical layers. However, simulation outputs exhibited high variability corresponding to parameter inputs, confirming that the experimental methods used to obtain them are very important.

Ultimately, while a high infiltration capacity in sandy soil makes the test site undoubtedly suitable for Ag-MAR, it inherently carries the risk of leaching agrochemicals, encouraging further analysis for a groundwater quality risk assessment of MAR operations and highlighting the need for a robust and prompt quality monitoring and alert system.

Table of Contents

Abstract 2
Table of Contents 4
List of Figures 6
List of Tables 10
1 Introduction 12
1.1 Global Water Scarcity and Ground Water Table Decline 12
1.2 Impacts of Climate Change on Groundwater in North-Western Italy 14
1.3 Managed Aquifer Recharge (MAR) and Agricultural MAR (Ag-MAR) 18
1.4 Thesis Structure and Research Objectives 22
2 Study Area 24
2.1 Mortara Site 26
2.2 Beinette Site 28
3 Materials and Methods 31
3.1 Water Flow and Solute Transport Dynamics 31
3.2 Imazamox 35
3.3 Field Infiltration Tests 36
3.3.1 Constant-Head Single-Ring Infiltration Test (F-C) 37
3.3.2 Falling-Head Single-Ring Infiltration Test 41
3.4 Soil Sampling 43
3.5 Laboratory Tests 45
3.5.1 Dry Density and Residual Volumetric Water Content 46
3.5.2 Total Organic Carbon (TOC) Measurement 47
3.5.3 Granulometric Analysis 48
3.5.4 Effluent and Soil Solution Preparation 49
3.5.5 KBr Tracer Calibration 49
3.5.6 Fluorescein and Rhodamine Calibrations 50
3.5.7 Agglomeration Tests 52
3.5.8 Preparing Soil Cores for Colum Tests 54
3.5.9 Soil Column Saturation Phase 54
3.5.10 Column Tracer Experiments 56

3.5.11 Imazamox Transport Experiments 57
3.6 HYDRUS-1D Modelling 59
3.6.1 Determination of Soil Parameters 60
3.6.2 Theoretical Background of Solute Transport Modelling 62
3.6.3 Boundary Conditions 63
3.7 Summary of Experimental Workflow and Site-Specific Activities. 65
4 Results and Discussion 70
4.1 Field Infiltration Experiments 70
4.1.1 Constant-Head Infiltration Tests 70
4.1.2 Falling Head Infiltration Tests 72
4.2 Soil Characterization 74
4.2.1 Granulometric Analysis 74
4.2.2 Dry Density and Initial Water Content 76
4.2.3 Total Organic Carbon 77
4.2.4 Estimation of Soil Hydraulic Parameters via Pedotransfer Functions 77
4.3 Tracer Selection and Validation 78
4.3.1 KBr Calibration 78
4.3.2 Fluorescein and Rhodamine Compatibility 79
4.3.3 Agglomeration Tests 81
4.4 Laboratory Column Tests 82
4.4.1 Column Saturation and Tracer Tests 86
4.4.2 K_D Evaluation for Rhodamine 94
4.4.3 Imazamox Transport Tests: Im-M3S and Im-M3D 96
5 Ag-MAR Modelling 101
5.1 Type A: 1D Vadose Zone Modelling 103
5.2 Type B: Analytical Mound Modelling 107
6 Conclusions 111
7 Bibliography 113

List of Figures

Figure 1.1: Global surface temperature change relative to 1850–1900. 12
Figure 1.2: Annual average monthly blue water scarcity (Period: 1996-2005)..... 13
Figure 1.3: Global sectoral water withdrawals 13
Figure 1.4: Historical mean annual air temperature in Torino (1900–2022) with linear trendline..... 15
Figure 1.5: Regional land use classification. 16
Figure 1.6: Trend of groundwater table in monitoring wells of the Piedmont Plain in the period from 2002 to 2017.. 17
Figure 1.7: Ground water boundary across Po river hydrographic district. 18
Figure 1.8: Infiltration-based MAR methods. 19
Figure 1.9: Direct injection-based MAR methods 20
Figure 2.1: Location of Mortara and Beinette study sites in Northern Italy.. 24
Figure 2.2: Regional hydrogeological setting of Northwest Italy. 25
Figure 2.3: Topsoil textural classes (Depth 0- 1 m) around the Mortara study site..... 26
Figure 2.4: Spatial distribution of rice cultivation and the primary irrigation canal network surrounding the Mortara study site within Pavia Province. 27
Figure 2.5: Shallow aquifer piezometric contours and ground water flow direction. 28
Figure 2.6: Soil classification map of Beinette.. 29
Figure 2.7: Depth to groundwater (soggiacenza, m b.g.s.) of the superficial aquifer (GWB-S7) at monitoring station 00401610001 in in Beinette (2001-2025). 30
Figure 3.1: Laboratory device used to verify Darcy's law. 31
Figure 3.2 Variation of hydraulic conductivity of different soil types with pore water pressure head..... 32
Figure 3.3: Field infiltration and soil sampling locations at the Mortara study site. 36
Figure 3.4: Field infiltration test locations at the Beinette study site. 37
Figure 3.5: Single-ring, constant-head infiltration setup 38
Figure 3.6 : Cumulative infiltration (I) plotted against the time (t) during the single-ring, constant-head infiltration test at Location 2 at the Mortara site. 39
Figure 3.7: Field infiltration setup diagram with key parameters. 39

Figure 3.8: Cumulative infiltration (I) plotted against the square root of time (t) during the single-ring, constant-head infiltration test at Location 2 at the Mortara site. 41
Figure 3.9: Single-ring, falling-head infiltration setup before filling. 42
Figure 3.10: Left-hand side of Equation 20 plotted against time for the shallow falling-head infiltration test at Mortara Location 3. 43
Figure 3.11: Soil sampling equipment and core extraction 44
Figure 3.12: A Column core sample after removing a soil layer for evaluating θr and ρd. 46
Figure 3.13: Shimadzu TOC analysis setup comprising the SSM-5000A Solid Sample Combustion Unit. 47
Figure 3.14 Mechanical sieve shaker used for granulometric analysis. 48
Figure 3.15: Calibration curve of KBr. 50
Figure 3.16: Spectrophotometer setup 51
Figure 3.17: Absorbance spectra of two multi-tracer solutions containing 0.3966 $g.L^{-1}$ KBr with mixed Fluorescein and Rhodamine. 51
Figure 3.18: Effluent from Mortara 1 column after KBr injection 52
Figure 3.19: Soil Core sample prepared for infiltration and tracer testing. 54
Figure 3.20: Mariotte bottle setup maintaining a constant ponded water layer. 55
Figure 3.21: The Setup for two tracer tests in parallel. 56
Figure 3.22: Intensity registered over time during the chromatogram run 58
Figure 3.23: HPLC chromatogram at 247 nm 58
Figure 3.24: Timeline of experimental phases for each column test. 68
Figure 3.25: Flow chart of the study 69
Figure 4.1: Cumulative infiltration (I) plotted against the square root of time ($\sqrt{t}$) for the constant-head infiltration tests: (a) IN-C-M2 and (b) IN-C-B1 71
Figure 4.2: Cumulative infiltration (I) plotted against time (t) for the constant-head infiltration tests: (a) IN-C-M2 and (b) IN-C-B1 71
Figure 4.3: Linearization variable Y (left-hand side of Equation 13) plotted against time for the falling-head infiltration tests. 73
Figure 4.4: USDA soil texture triangle. 75
Figure 4.5: Calibration curve of KBr 79

Figure 4.6: Normalized absorbances of fluorescein at a concentration of 0.0025 g/L in different solutions. 79
Figure 4.7: Normalized absorbances of rhodamine at a concentration of 0.00667 g/L in different solutions 80
Figure 4.8: Calibration curve of Rhodamine in KBr background solution measured at a wavelength of λ = 565.5 nm 80
Figure 4.9: Variation in normalized count rate over time for different solutions. 81
Figure 4.10: Complete breakthrough curves and effluent discharge dynamics during column experiment for U-M3S core. 84
Figure 4.11: Complete breakthrough curves and effluent discharge dynamics during column experiment for U-M3D core. 85
Figure 4.12: Relative concentration of KBr (C/C_0) and outflow rate during the preliminary tracer test KBr-M1A. 88
Figure 4.13: Relative concentration of KBr (C/C0) and outflow rate during the preliminary tracer test KBr-M2A. 89
Figure 4.14: Observed and simulated KBr concentration breakthrough curves for preliminary column test KBr-M2A. 90
Figure 4.15: Breakthrough curves of relative concentration (C/C_0) and effluent flow rate over time for tracer tests conducted on the U-M3S core. 91
Figure 4.16: Breakthrough curves of relative concentration (C/C_0) and effluent flow rate over time for tracer tests conducted on the U-M3D core. 91
Figure 4.17: Measured and simulated KBr breakthrough curves obtained from inverse modelling for the KBr-M3S tracer test. 93
Figure 4.18: Measured and simulated KBr breakthrough curves obtained from inverse modelling for the KBr-M3D tracer test. 93
Figure 4.19: Natural preferential macropore identified in soil core U-M1B. 94
Figure 4.20: Simulated Rhodamine breakthrough curve using inverse modelling alongside measured data for the Rh-M3S. 95
Figure 4.21: Simulated Imazamox breakthrough curve using inverse modelling alongside measured data for Rh-M3D 95
Figure 4.22: Breakthrough curve of imazamox and effluent flow rate over time for Im-M3S. 97

Figure 4.23: Breakthrough curve of imazamox and effluent flow rate over time for Im-M3D. 97
Figure 4.24: Simulated Imazamox breakthrough curve using inverse modelling alongside measured data of Im-M3S test. 98
Figure 4.25: Simulated Imazamox breakthrough curve using inverse modelling alongside measured data for Im-3MD. 99
Figure 5.1: Schematic of transient groundwater mound formation during localized infiltration recharge 101
Figure 5.2: Water pressure head variation at the bottom of the simulated soil profile (AM-8L, AM-16L, AM-8F, and AM-16F: 5 m depth; AB-8F and AB-16F: 15 m depth) under deep drainage lower boundary conditions..... 105
Figure 5.3:Simulated groundwater mounds (Δh) under a 1-day pulse recharge event.. 109

List of Tables

Table 3.1:Details of soil samples 45
Table 3.2: Summary of experimental activities, test locations, and sample identifiers. 65
Table 3.3: Summery of field infiltration tests with experimental conditions 67
Table 3.4: Cumulative timeline for experimental activities in soil column tests. Time starts at the beginning of saturation phase and extends until the tracer start. 67
Table 4.1: Cumulative infiltration before establishing a constant ponded water head during constant-head infiltration tests. 70
Table 4.2: Summary of constant-head single ring infiltration tests. 72
Table 4.3: Summary of falling-head single-ring infiltration test results. 74
Table 4.4: Percentage of particle fractions and USDA soil category 75
Table 4.5: Dry bulk density and initial Volumetric Water Content (VWC) 76
Table 4.6: Total Organic Carbon (TOC) of soil samples 77
Table 4.7: Estimated van Genuchten soil hydraulic parameters obtained from pedotransfer functions. 78
Table 4.8: Electrical Conductivity of Effluent 78
Table 4.9: Experimental timeline, hydraulic boundary conditions, and solution parameters across all operational phases for column U-M3S 82
Table 4.10: Experimental timeline, hydraulic boundary conditions, and solution parameters across all operational phases for column U-M3D. 83
Table 4.11: Hydraulic conductivity at the saturation phase 86
Table 4.12: Summery of saturated hydraulic conductivity measured in the field and laboratory. 87
Table 4.13: Calibrated saturated water content (θS) and longitudinal dispersivity (α) obtained from HYDRUS-1D inverse simulation for column U-M2A. 90
Table 4.14: Water head, flow rate, and calculated K_S for tracer tests KBr-M3S and KBr-M3D. 92
Table 4.15: Saturated volumetric water content (VWC) and Dispersivity of undisturbed soil samples from Mortara Location 3 93
Table 4.16: Key input parameters for rhodamine breakthrough curve inverse modelling. 95

Table 4.17: Estimated K_D and K_{oc} values for Rhodamine 96
Table 4.18: Flow rates during flushing phase of imazamox transport tests (Im-M3S and Im-M3D) and input parameters into inverse modelling of Imazamox BTC 98
Table 4.19: Distribution Coefficient (K_D) and organic carbon-normalized adsorption coefficient (K_{oc}) 100
Table 5.1: Summary of all simulations 102
Table 5.2: Summary of physical and hydraulic properties of soil profiles..... 103
Table 5.3: Summary of soil profile of Mortara for modelling type A..... 104
Table 5.4: Summary of soil profile of Beinette for modelling type A 104
Table 5.5: Summary of infiltration soil profile of Mortara for modelling type B. 107
Table 5.6: Summary of infiltration soil profile of Beinette for modelling type B. 107
Table 5.7: Simulated steady-state infiltration fluxes (q). 107
Table 5.8:Input hydrogeological and geometrical parameters for the Hantush analytical mound model. 109

1 Introduction

1.1 Global Water Scarcity and Ground Water Table Decline

Water scarcity is a growing concern highly influenced by climate change, which is due to anthropogenic activities including greenhouse gas emissions by fossil fuel combustion, deforestation and alterations of land use pattern. The global surface temperature was 1.1 ℃ higher in the 2011-2020 period compared to the 1850-1900 period, as illustrated in Figure 1.1 (IPCC, 2023). This trend, accelerates the water cycle, shifts snow to rain, and shifts snowmelt timing earlier, and amplifies flood/drought extremes (Cook et al., 2020; Oki & Kanae, 2006). Additionally, water scarcity is driven by rapid population growth, expanding industrial demand, and unsustainable water resource exploitation (Kummu et al., 2016; Vörösmarty et al., 2010).

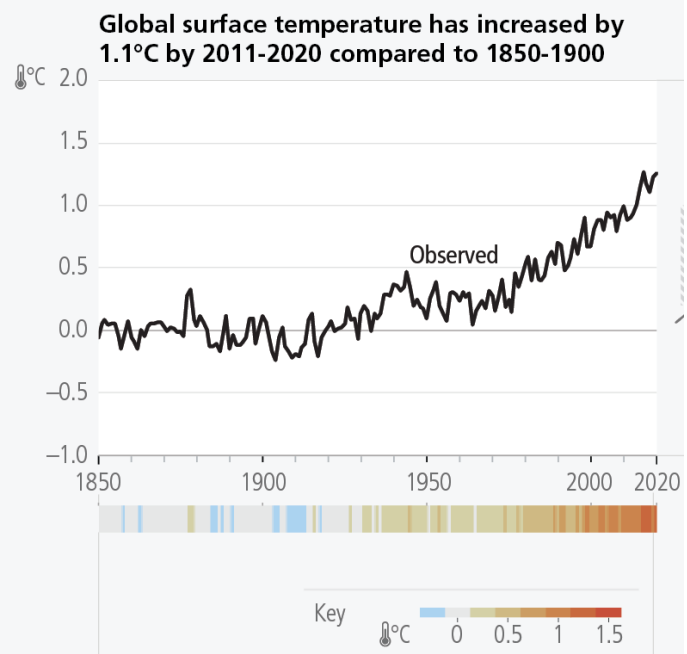


Figure 1.1: Global surface temperature change relative to 1850–1900 (adapted from IPCC, 2023).

The water scarce population of the world increased nearly 16-fold from 1900 (0.24 billion) to 2000 (3.8 billion) (Kummu et al., 2016), and this is a considerable increase compared to global population growth. The global freshwater flux is theoretically sufficient so satisfy the demand, however spatial and temporal variability cause temporary water scarcity (Kummu et al., 2016). Figure 1.2 (Mekonnen & Hoekstra, 2016) illustrates the spatial distribution of annual average monthly water scarcity index (SW) - where SW is the

ration of water consumption to sustainable blue water availability. Furthermore, four billion peoples in the world (two-thirds of the global population) face severe water scarcity (SW>2) for at least one month per year (Mekonnen & Hoekstra, 2016).

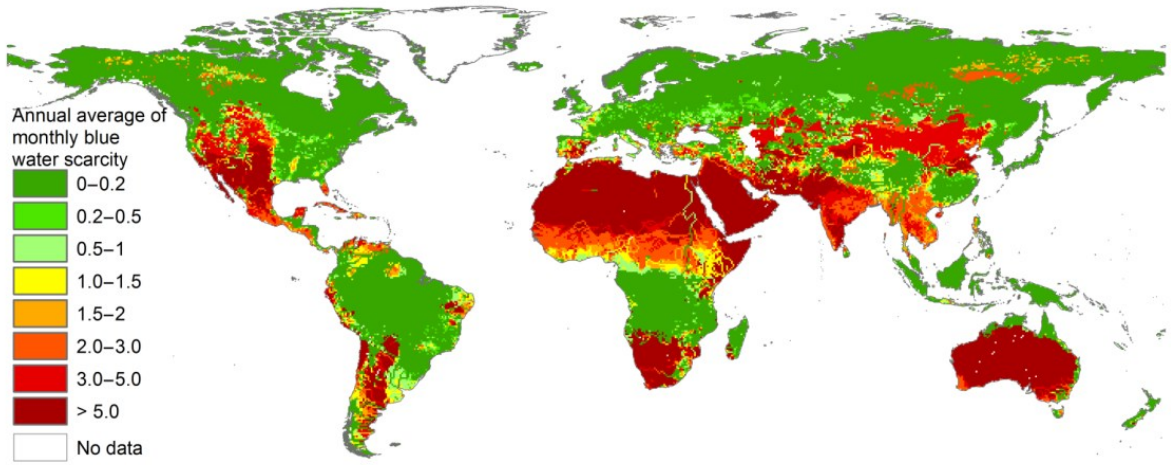


Figure 1.2: Annual average monthly blue water scarcity (Period: 1996-2005) (adapted from Mekonnen & Hoekstra, 2016).

The main contributor to water resource overexploitation and the most vulnerable sector is agriculture, accounting for more than 70% of global freshwater withdrawals (FAO, 2020). Nevertheless, the demand increases continuously (Figure 1.3) and competes with other sectors to feed the growing global population (FAO, 2020).

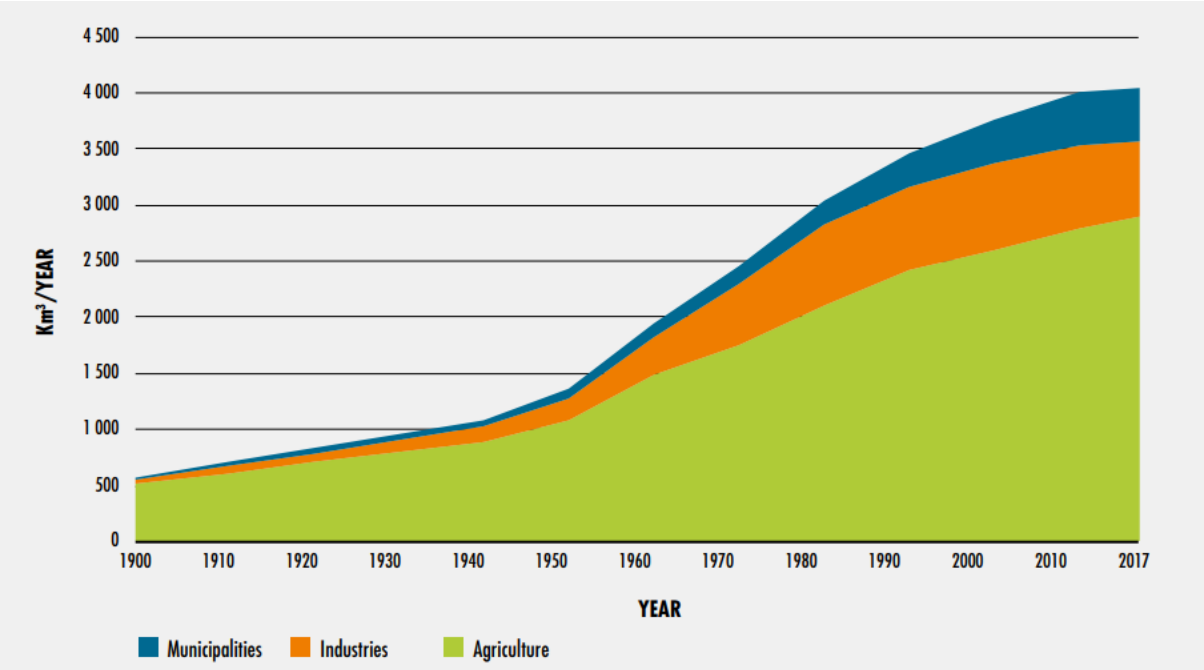


Figure 1.3: Global sectoral water withdrawals (adapted from FAO, 2020)

In this framework, groundwater resources are used to buffer temporary water scarcity. The global groundwater withdrawals in 2018 were estimated to be approximately 978 km^3 per year for all sectors (AQUASTAT, n.d.; Eurostat, n.d.; UNESCO, 2022). Agriculture remains the largest user, representing 70% of total ground water withdrawals, while 38% of irrigated lands are supplied by groundwater (Margat & van der Gun, 2013; Siebert et al., 2013; UNESCO, 2022).

Consequently, groundwater levels declined rapidly (>0.5 m yr^{-1}) in the 21st century across many regions in the world, alongside accelerating decline trends over the last four decades in 30% of the world's regional aquifers. Furthermore, both rapid and accelerating declines are particularly evident in aquifers underlying cultivated drylands (Jasechko et al., 2024). In contrast, a considerable number of aquifer systems showed decelerating trends alongside a few that recovered in the late 20th century and the early 21st century (Jasechko et al., 2024).

1.2 Impacts of Climate Change on Groundwater in North-Western Italy

The area of Turin (North-West Italy) is facing severe impacts from climate change. For instance, the area showed an increasing trend in air temperature, as shown in Figure 1.4. However, there is no trend in the variation of rainfall according to the Mann-Kendall trend tests applied across 30 pluviometric stations ($p > 0.05$ across all gauges) throughout the Piedmont plain for the period 2002–2017, although temporal variability is substantial (Lasagna et al., 2019). Moreover, the relationship between precipitation and the groundwater table (GWT) is generally weak. Instead, several other factors play a role, namely presence of losing watercourses in vicinity, ground water withdrawal, and agricultural land-use patterns (Egidio et al., 2025; Lasagna et al., 2019).

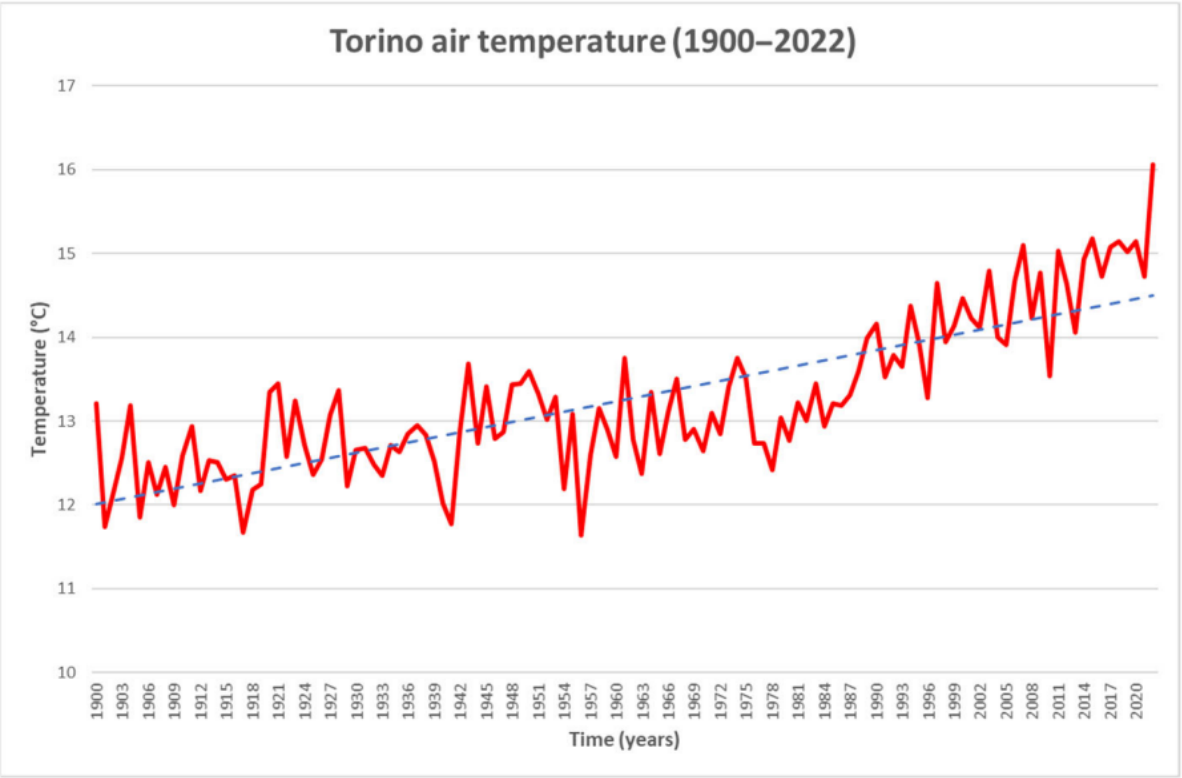


Figure 1.4: Historical mean annual air temperature in Torino (1900–2022) with linear trendline. (Egidio et al., 2025)

As a matter of fact, the Piedmont plain in NW Italy is largely dominated by agricultural land, as shown in Figure 1.5 (Egidio et al., 2025). Along with climate pressures, a major concern is that the groundwater level cycle is significantly shifted in agricultural sectors dominated by corn and submerged rice paddies, where the annual peak occurs during the summer irrigation season rather than during the natural spring snowmelt and precipitation period (Egidio et al., 2025; Lasagna et al., 2019). Consequently, the combined effects of climate change and land-use patterns represent a critical challenge for groundwater resource management in this region.

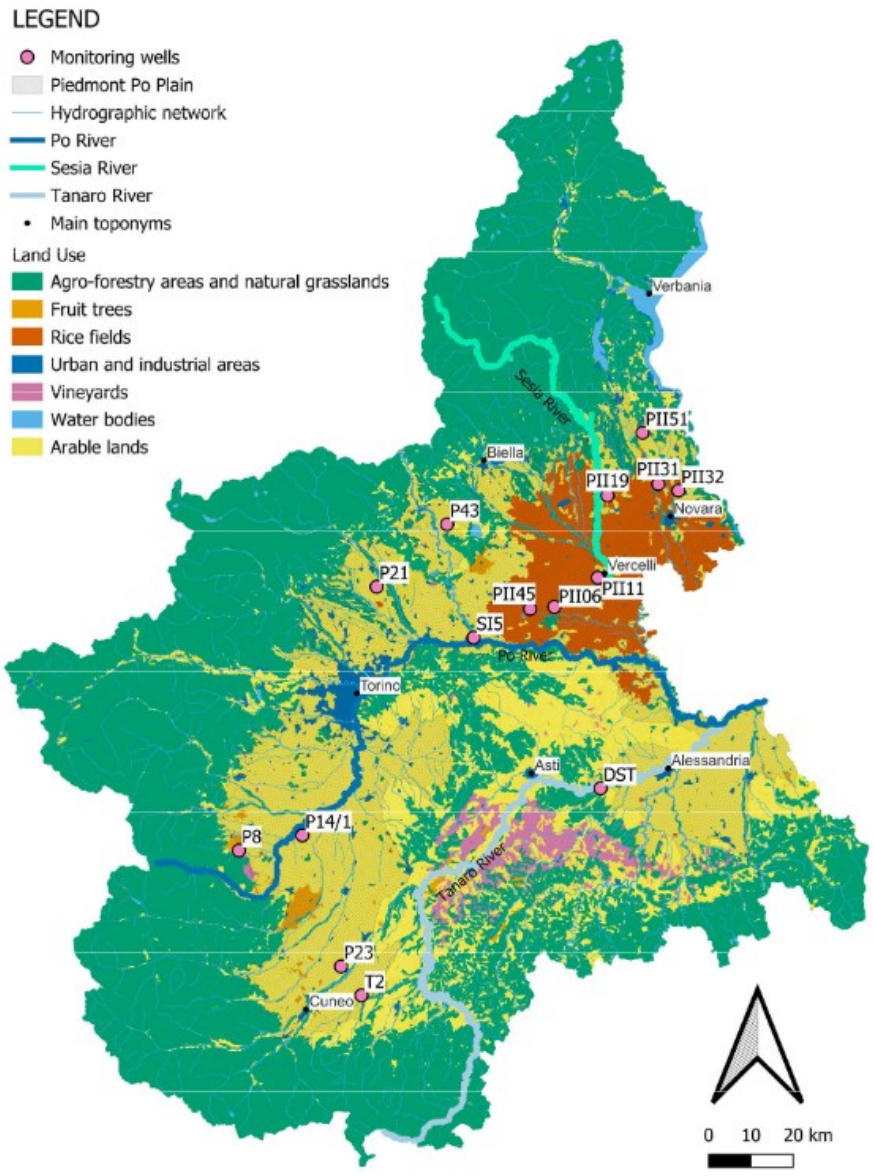


Figure 1.5: Regional land use classification. (Egidio et al., 2025)

Moreover, the study by Lasagna et al., (2019), based on data from the period 2002–2017, showed that 22% of the analysed monitoring wells (8 out of 37 shallow monitoring wells) in the Piedmont region had a downward trend, while 24% (9 wells out of 37) showed an upward trend. The other wells did not show any trend, as shown in Figure 1.6 .

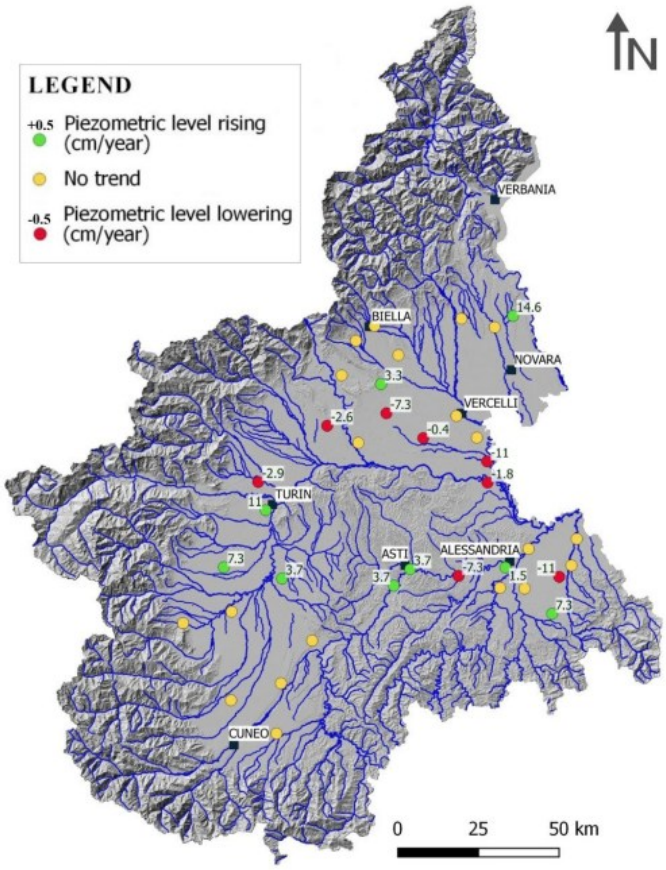


Figure 1.6: Trend of groundwater table in monitoring wells of the Piedmont Plain in the period from 2002 to 2017. (Lasagna et al., 2019).

However, the study by Egidio et al., (2025), conducted over the period 2010 to 2022- a shorter period but with more recent data including the severe drought year of 2022- showed a widespread decline in the groundwater table in NW Italy across 15 wells, with an average lowering of 4.32 cm/year.

This declining trend is clear evidence of the vulnerability of the shallow groundwater system, which is bounded by an underlying aquitard at the bottom and open to the atmosphere at the top as an unconfined aquifer. Figure 1.7 (Autorità di Bacino Distrettuale del Fiume Po, 2021) shows the shallow groundwater body delineation across the Po River hydrographic district. A large portion of this area-including Cuneo, Vercelli, and Novara -is covered by sandy-silty central plain alluvium (CA), which provides both favourable primary permeability for surface infiltration and substantial pore storage capacity, making these porous sediments highly suitable for artificial recharge systems and seasonal groundwater storage. Crucially, both Egidio et al., (2025) and Lasagna et al., (2019) demonstrated that the replenishment of groundwater by rainfall is not significant

across most of the study area, and the influence of surface water sources like rivers remains highly localized. Moreover, recharge is largely anthropogenic, driven primarily by agricultural irrigation. Considering these factors, to counteract the impacts of climate change, relying solely on natural replenishment and mitigating climate forcing are not enough; instead, the aquifers should be recharged not only through unintentional agricultural flooding, but also through Managed Aquifer Recharge (MAR) methods.

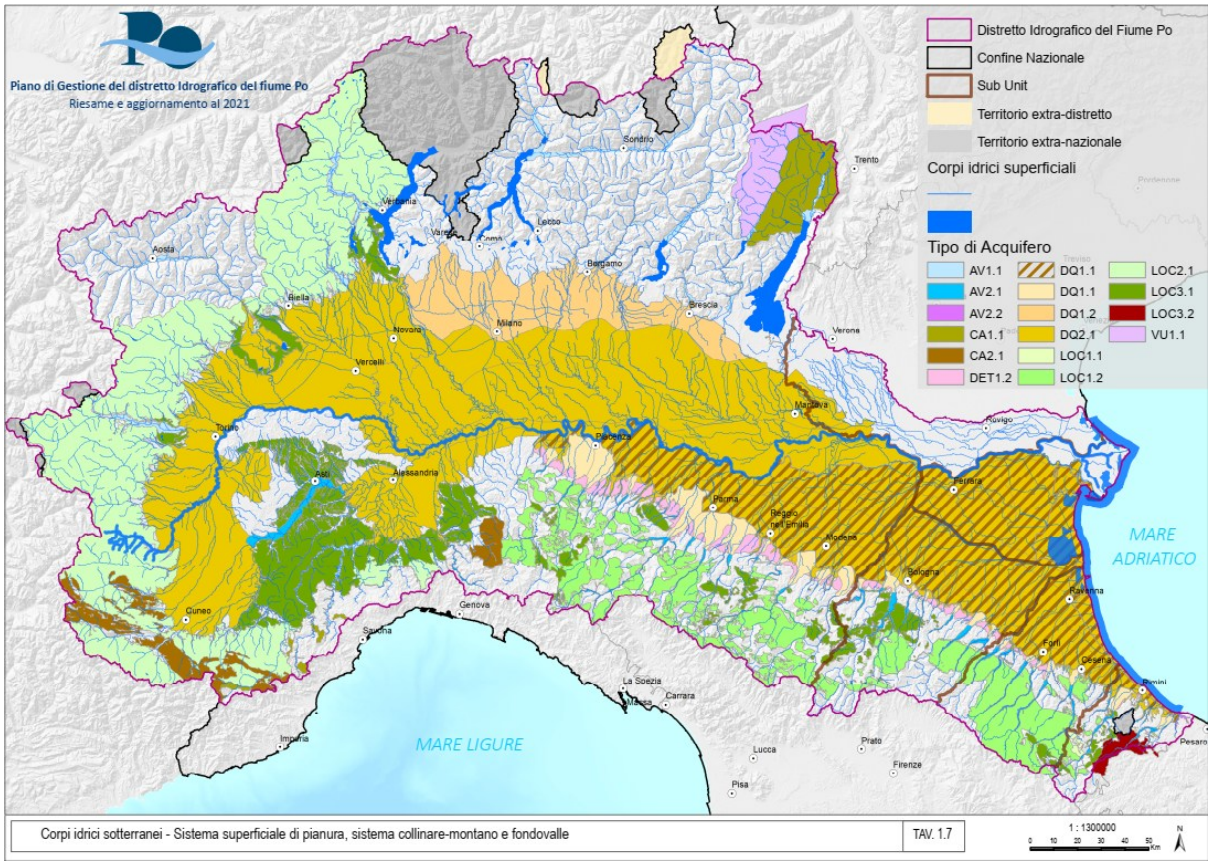


Figure 1.7: Ground water boundary across Po river hydrographic district (Autorità di Bacino Distrettuale del Fiume Po, 2021). Aquifer codes designate hydrogeological typologies: ***AV****: Coarse alluvial fan gravels and sands (high permeability),* ***CA****: Sandy-silty central plain alluvium (medium-low permeability),* ***DQ****: Fine distal and deltaic sediments,* ***LOC****: Local aquifers and low-permeability hill formations,* ***DET****: Morainic and slope detrital deposits,* ***VU****: Fractured and karstified carbonate bedrock.*

1.3 Managed Aquifer Recharge (MAR) and Agricultural MAR (Ag-MAR)

Aquifers are replenished naturally through the infiltration of rainwater, seepage from natural streams, and anthropogenically induced recharge. Anthropogenic recharge can be grouped into three categories: unintentional, unmanaged and managed recharge (Dillon et al., 2009). Managed aquifer recharge (MAR) belongs to the third category, defined as “the purposeful recharge of water to aquifers for subsequent recovery or

environmental benefit" (Dillon et al., 2009). MAR restores overexploited aquifers by balancing water demand and supply, while serving as a mechanism to store surplus surface water when resources are abundant (Sufyan et al., 2024).

From an engineering perspective, MAR is mainly divided into two broad categories depending on whether recharge relies on passive percolation by gravity-driven infiltration or forced injection directly into the target formation via pressurized boreholes (Alam et al., 2021; Dillon et al., 2009). Infiltration-based methods, illustrated in Figure 1.8, include infiltration ponds and basins, soil aquifer treatment (SAT), bank filtration, and percolation ponds.

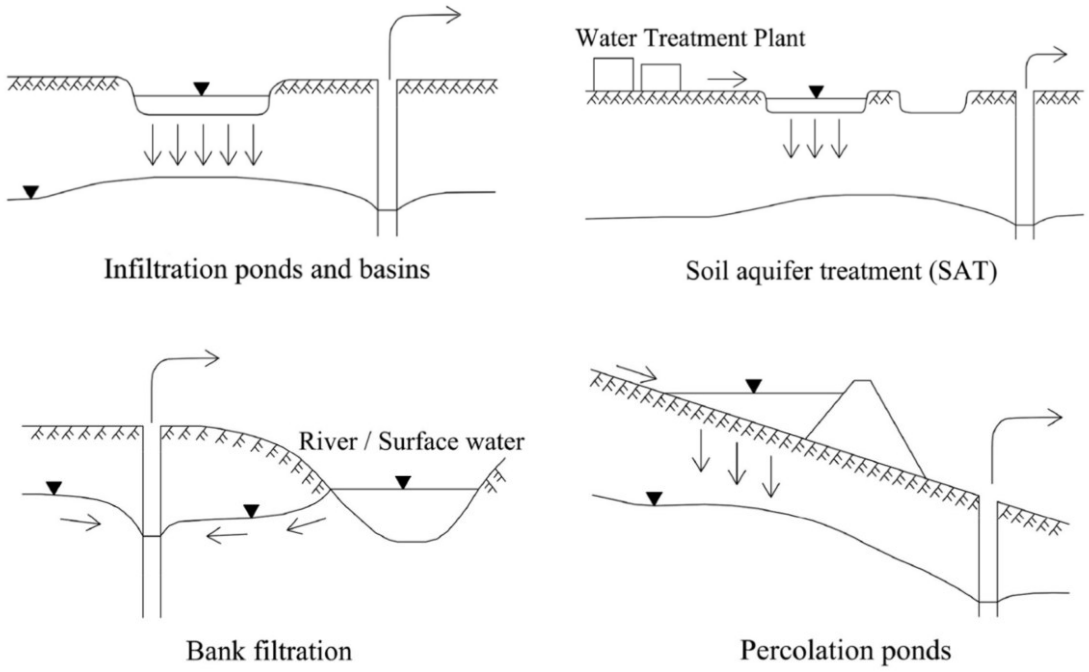


Figure 1.8: Infiltration-based MAR methods. Modified from Dillon et al., (2009) and Zhang et al., (2020)

Infiltration-based methods are suitable for flat and low-slope terrain (slopes < 3%). These passive methods require minimal energy, resulting in low operational costs (Alam et al., 2021). Conversely, direct injection methods via boreholes include Aquifer Storage and Recovery (ASR), Aquifer Storage, Transfer, and Recovery (ASTR), dry wells, and vadose zone shafts, as illustrated in Figure 1.9 (Alam et al., 2021; Dillon et al., 2009; Zhang et al., 2020).

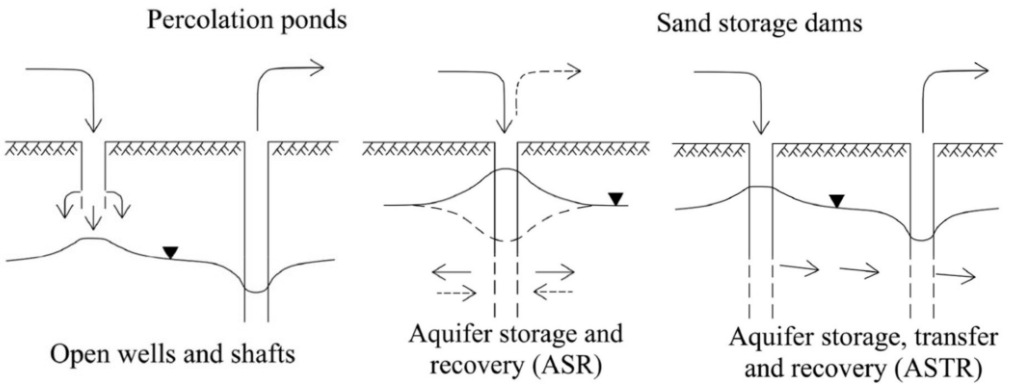


Figure 1.9: Direct injection-based MAR methods Modified from Dillon et al., (2009) and Zhang et al., (2020)

Direct injection methods demand a much smaller land footprint and operate independently of vadose zone permeability (Alam et al., 2021). However, because they completely bypass the unsaturated zone, these systems exhibit negligible capacity for the natural attenuation of dissolved organic carbon (DOC), suspended solids, and pathogens, requiring high-quality source water or intensive pre-treatment to prevent well-screen clogging and aquifer contamination (Alam et al., 2021; Zhang et al., 2020).

Compared to conventional surface water reservoirs, MAR provides significant advantages (Alam et al., 2021; Zhang et al., 2020). Constructing artificial surface reservoirs requires high capital investment, leaves infrastructure vulnerable to dam failure or overtopping risks, and incurs heavy evaporative water losses-especially under Mediterranean climatic regimes (Alam et al., 2021; Zhang et al., 2020). However, traditional infiltration MAR requires dedicated, single-purpose land allocations, which is economically prohibitive in intensively farmed alluvial plains (Alam et al., 2021; Levintal, Kniffin, et al., 2023). Moreover, farmland with flooding irrigation crops significantly recharges groundwater (Colombo et al., 2024; Dillon et al., 2009). Considering these factors, farmlands can be allocated for MAR during the off-season when water is abundant in this period (Levintal, Huang, et al., 2023; Levintal, Kniffin, et al., 2023). This kind of MAR is called agricultural managed aquifer recharge (Ag-MAR) (Levintal, Kniffin, et al., 2023). Specifically, northwestern Italy irrigates farmland using river water, which means water is abundant in the non-growing season (Colombo et al., 2024). This makes a suitable setup for implementing Ag-MAR, except when irrigation canals are closed for maintenance during these seasons.

The MAURICE pilot project in western Lombardy, implemented off-season flooding across 32.3 ha of agricultural land, and showed that 80% of the diverted water was retained in the shallow aquifer by late winter, raising the groundwater table by up to 26 cm (Colombo et al., 2024). Due to the low regional groundwater velocity, 58% of this water was still retained at the start of summer, sustaining an average groundwater rise of 2.2 cm over a 190 km^2 area (Colombo et al., 2024). This stored volume was equivalent to 12 small surface reservoirs of 25,000 m^3 each (Colombo et al., 2024).

Ag-MAR offers substantial advantages: capital expenditure is low because existing conveyance networks, ditches, and furrows are utilized without requiring land acquisition (Alam et al., 2021; Colombo et al., 2024; Dahlke et al., 2018). Furthermore, extensive agricultural land cover across northwestern Italy provides large spatial capacity for regional scaling, while the highly permeable sand and gravel deposits characteristic of the Po plain alluvium facilitate rapid infiltration into the unconfined aquifer (Autorità di Bacino Distrettuale del Fiume Po, 2021; Colombo et al., 2024).

However, it holds some downward impacts as well (Alam et al., 2021; Levintal, Kniffin, et al., 2023). Prolonged standing water can compact the topsoil layer and reduce dissolved oxygen in the pores, altering biological cycles in the soil (Alam et al., 2021; Levintal, Kniffin, et al., 2023). Moreover, it can form an impermeable soil layer, degrading soil infiltration capacity (Alam et al., 2021). Furthermore, agricultural soils contain agrochemicals and nitrate (Levintal, Huang, et al., 2023). High infiltration fluxes can leach them, reducing soil fertility and increasing the environmental risk of groundwater contamination (Levintal, Huang, et al., 2023; Rodríguez-Escales et al., 2018).

To evaluate Ag-MAR feasibility, quantitative characterization of key subsurface flow and storage parameters is essential: saturated hydraulic conductivity (K_S), which dictates the maximum vertical transmission rate through the vadose zone, and porosity (equals to saturated volumetric water content θ_S), which determines drainable pore storage capacity per unit volume of soil (Alam et al., 2021; Zhang et al., 2020).

The characterization methodology for Ag-MAR combines in situ field infiltration testing (including single-ring and double-ring infiltrometers and borehole Lefranc tests), laboratory column transport experiments using tracers to evaluate porosity, and inverse

numerical modelling to quantify unsaturated hydraulic parameters alongside remote sensing methods (Alam et al., 2021; Tosco, 2024a; Zhang et al., 2020).

In this context, this study evaluates Ag-MAR feasibility during winter flooding through in-situ field tests on a paddy field already practicing winter flooding in Mortara, near a dedicated pilot site established within the SeTe-ALCOTRA project in Beinette and through laboratory column experiments conducted on undisturbed soil cores collected from these sites.

1.4 Thesis Structure and Research Objectives

The primary focus of this study is to evaluate the hydrodynamic feasibility and environmental implications of Agricultural Managed Aquifer Recharge (Ag-MAR) during winter flooding in the alluvial plain of northwestern Italy by quantifying key vadose zone hydrodynamic parameters, infiltration capacity, and reactive solute transport parameters via field and laboratory experiments. The study is based on two agricultural settings: an active rice field practicing Ag-MAR recharge for 10 years in Mortara (Lomellina plain, PV, Lombardy) and an experimental pilot recharge site in Beinette (Cuneo plain, CN, Piedmont). To achieve these objectives, a multi-scale experimental framework combining field-scale testing and laboratory analyses was implemented.

First, in situ single-ring experiments were conducted under falling-head and constant-head conditions to characterize field-saturated hydraulic conductivity and to compare both methods to identify their reliability on the permeable sandy soils of the study area.

Subsequently, soil samples were collected from both sites in disturbed and undisturbed conditions and utilized for physicochemical characterization by measuring dry bulk density, initial volumetric water content, particle size distribution via mechanical sieving, and Total Organic Carbon (TOC) using the solid sample combustion method.

In addition, tracers commonly used in groundwater studies to track hydrodynamic behaviour were evaluated to analyse their validity for this study and to inform future investigations. The tracers evaluated were Potassium Bromide (KBr), Fluorescein, and Rhodamine. Their mutual interactions and interactions with the soil matrix were assessed by evaluating light absorbance variations and soil fine particle fraction

agglomeration using spectrophotometer measurements and the Dynamic Light Scattering (DLS) method.

Furthermore, soil column experiments were performed on undisturbed soil samples collected from Mortara to evaluate saturated hydraulic conductivity (K_S) and obtain breakthrough curves. Two simultaneous column tests were performed on cores collected from the same location, representing a continuous soil profile up to 38.5 cm. Two tracers were utilized: conservative KBr and non-conservative Rhodamine. Subsequently, a leaching and mobility test was performed for Imazamox, an herbicide widely used in paddy fields.

Finally, the column breakthrough curves were simulated by inverse numerical modelling using the HYDRUS-1D code to evaluate saturated volumetric water content (θ_S), dispersivity (α), and the soil distribution coefficient (K_d) for each reactive compound in the soil matrix. Moreover, the organic carbon-normalized partition coefficient (K_{OC}) of Imazamox was evaluated to compare with literature values.

Building upon these experimental parameters, numerical simulations were performed to evaluate the groundwater level response in terms of elevation, mounding, and dissipation. Secondly, they aimed to identify the sensitivity of the modelling outputs to input parameters obtained from different experimental methods.

To systematically present these investigations, this report is structured into several subsequent chapters. Chapter 2 describes the study areas of the two sites, detailing their regional and local hydrogeological settings. Chapter 3 presents the materials and methods used in this study, explaining the underlying theoretical background alongside the field and laboratory procedures. Chapter 4 reveals the experimental results alongside a detailed discussion of each activity. Chapter 5 presents the numerical and analytical modelling of Ag-MAR, evaluating downward percolation, aquifer mounding dynamics, and parameter sensitivity. Finally, Chapter 6 presents the conclusions, synthesizing the primary findings regarding Ag-MAR feasibility in northwestern Italy based on the evaluated hydrodynamic parameters, while addressing the operational reliability of field infiltration methods, tracer behaviour in the soil matrix, and the environmental risk of herbicide leaching.

2 Study Area

This research is based on two agricultural sites within the Po River basin in northwestern Italy: Mortara (Province of Pavia, Lombardy) and Beinette (Province of Cuneo, Piedmont) (Figure 2.1). Both study sites are located within the Po River basin-at the upstream and middle reaches (Figure 2.1), with a well-distributed irrigation canal system.

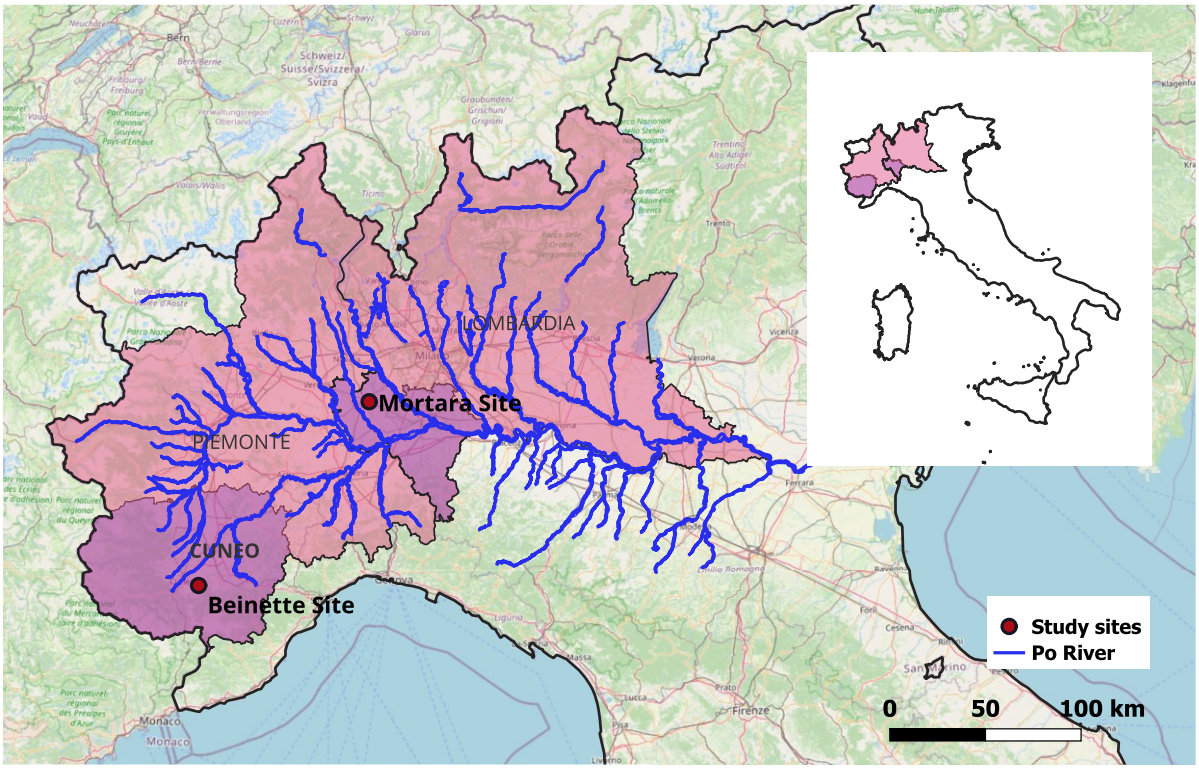


Figure 2.1: Location of Mortara and Beinette study sites in Northern Italy. Boundaries sourced from ISTAT, (2023); river networks adapted from AdbPo, (2020); basemap © OpenStreetMap contributors.

On one hand Mortara is located in the Lomellina area, dedicated to rice production. Indeed, Italy is the largest rice producer in Europe, with 235,000 ha of cultivated land in 2012; 90% of this total is concentrated in the northwestern regions of Piedmont and Lombardy, where paddy rice cultivation is widespread (Scarabel et al., 2012).

In this area, there is a mixed sandy-silty alluvial complex with medium to medium-high porosity and permeability, offering favourable conditions for passive infiltration methods for managed aquifer recharge (Figure 2.2; Beretta et al., (2021)). On the other hand, Beinette is located with a surrounding area of mix of coarse alluvial and fluvioglacial complex with high to very high permeability and porosity creating ideal for Ag-MAR (Figure 2.2; Beretta et al., (2021)).

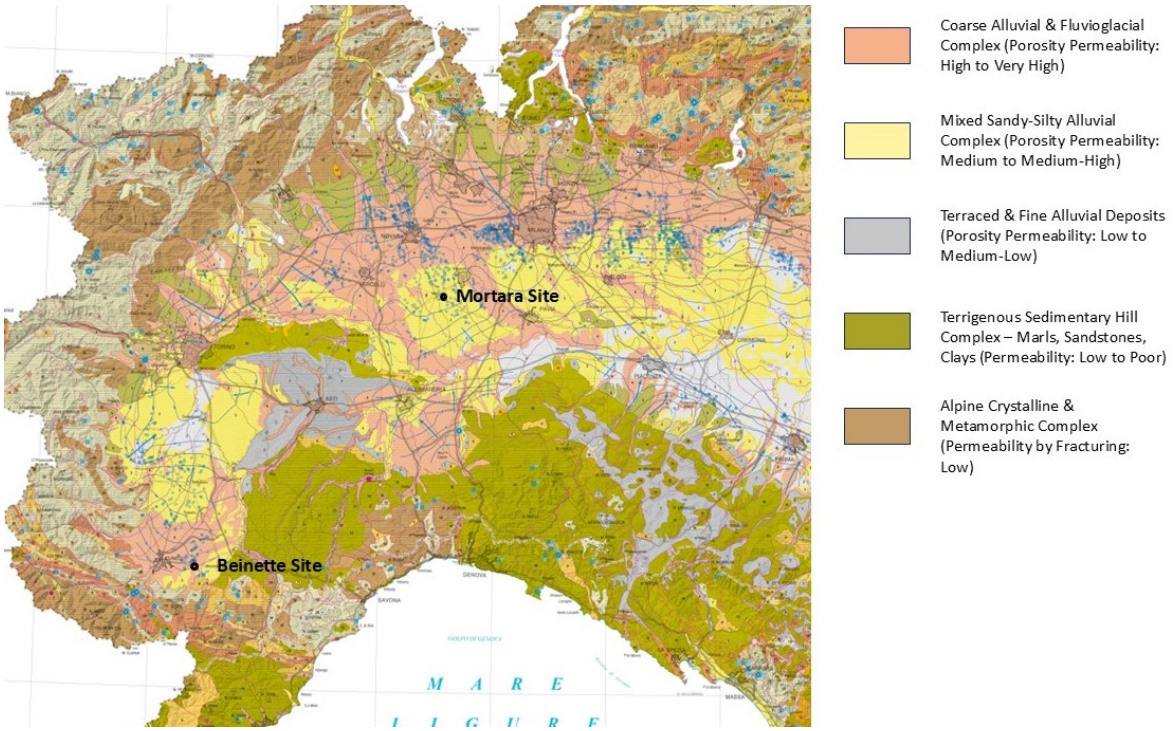


Figure 2.2: Regional hydrogeological setting of Northwest Italy. (Adapted from Beretta et al. (2021))

2.1 Mortara Site

A closer look at the Mortara site reveals that it is located in a sandy soil area (Figure 2.3). This is particularly advantageous, as sandy soils exhibit high porosity and permeability. Moreover, the adjacent areas consist of sandy loam and loamy sand soils, indicating that this site could theoretically be expanded for Ag-MAR from a hydrological point of view, especially since the entire surrounding area is predominantly covered by agricultural lands served by irrigation canals.

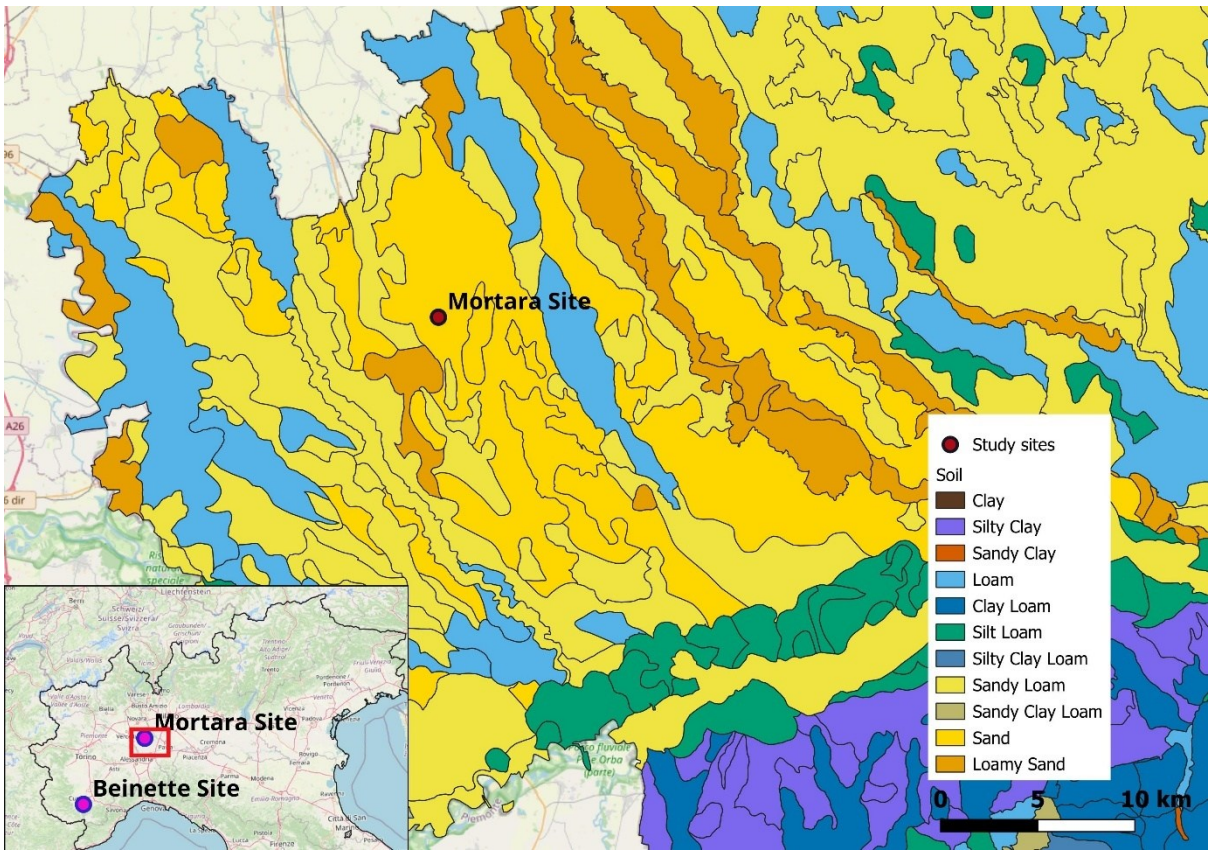


Figure 2.3: Topsoil textural classes (Depth 0- 1 m) around the Mortara study site. Data adapted from ERSAF & Regione Lombardia (2010); basemap © OpenStreetMap contributors.

The Mortara site is surrounded by extensive rice paddy fields (Figure 2.4), with cultivation taking place from April to October. Farmers begin spring land preparation by plowing and harrowing, followed by sowing between mid-April and May. Continuous ponded flooding occurs from May to August by diverting river water through the dense irrigation canal network, unintentionally replenishing the shallow unconfined aquifer. However, a hydrological study conducted in Candia Lomellina, adjacent to Mortara, demonstrated that the groundwater table returns to baseline levels within approximately two months following harvest and the cessation of summer irrigation (Negri et al., 2020).

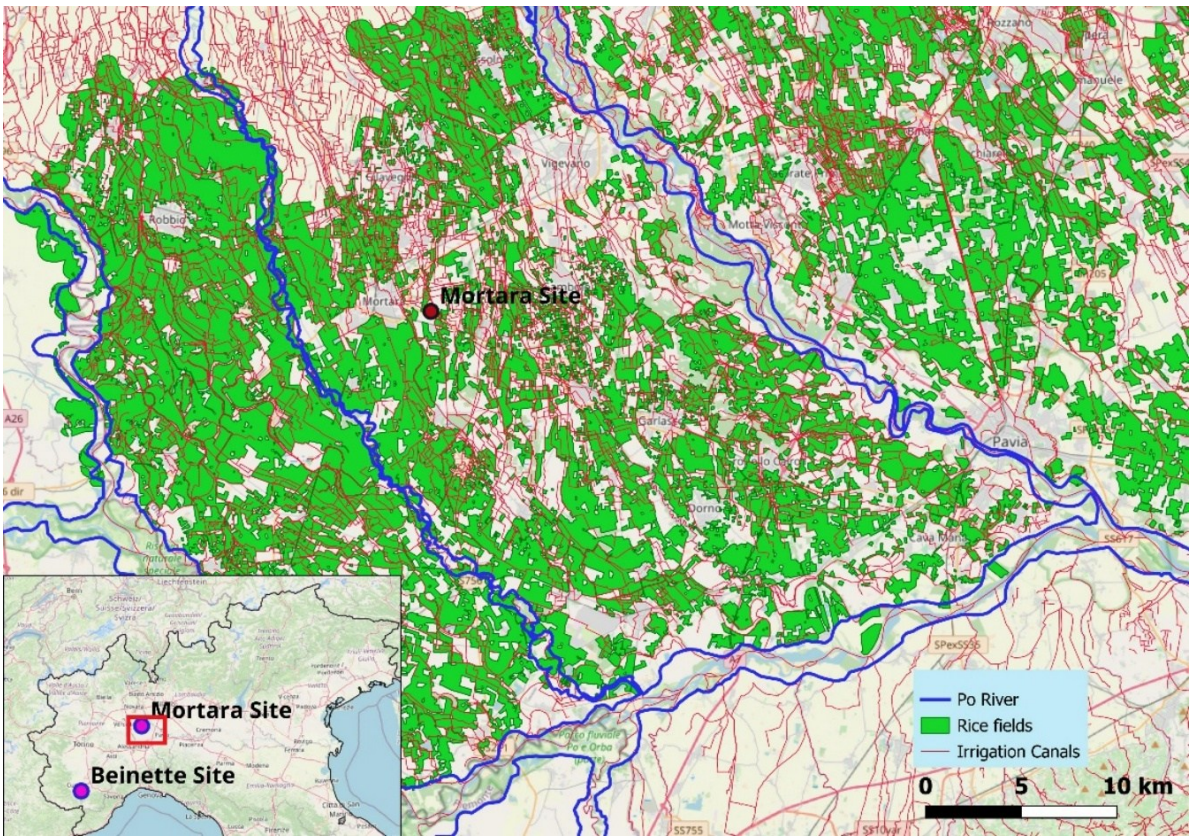


Figure 2.4: Spatial distribution of rice cultivation and the primary irrigation canal network surrounding the Mortara study site within Pavia Province. Adjacent areas outside the provincial boundary are omitted. Data retrieved from ERSAF & Regione Lombardia(2021) and Regione Lombardia (2022).

The piezometric contours of shallow aquifer system around the site run perpendicular to the tributary branches, resulting in groundwater flow that runs parallel to these upstream channels flowing North-to-South before discharging into the main Po River channel flowing West-to-East. This configuration maximizes groundwater retention, which may buffer local water supplies against temporal water scarcity (Figure 2.5).

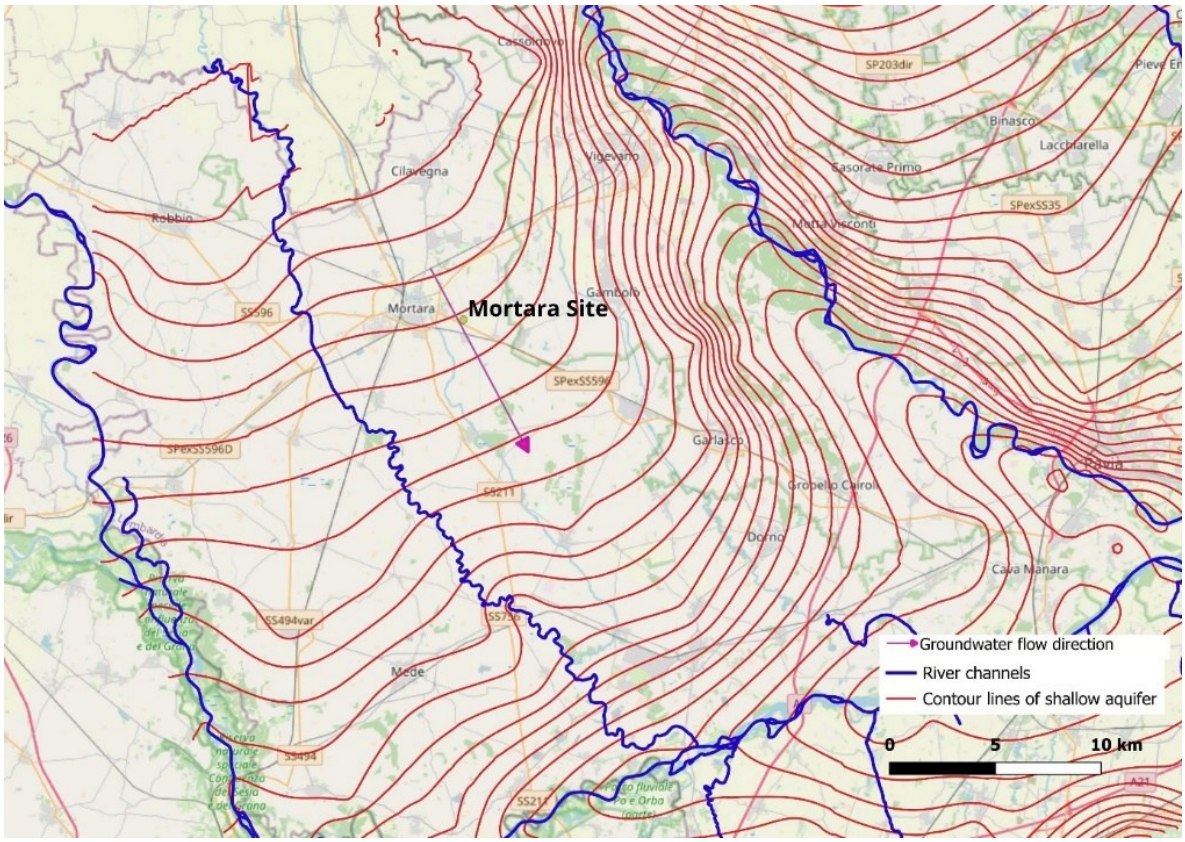


Figure 2.5: Shallow aquifer piezometric contours and ground water flow direction. Piezometric data adapted from Regione Lombardia & ARPA Lombardia (2016); river networks adapted from AIPo & Regione Lombardia (2022); basemap © OpenStreetMap contributors.

2.2 Beinette Site

The Beinette site, situated in the inland alluvial plain of Cuneo on the Right Stura Bank in southwestern Piedmont, is adjacent to a traditional spring-fed ditch system (*fontanili*), specifically the *Fontanile dei Paschi*. Under the SeTe-ALCOTRA project, a pilot study evaluating Managed Aquifer Recharge (MAR) through infiltration trenches is actively being investigated (Taramasso et al., 2025). In-situ field infiltration tests, laboratory grain size distribution analyses and total organic carbon analysis of the vadose zone were performed to characterize the top soil of site for comparison with the Mortara site.

As shown in Figure 2.6 the site is located in an area with loamy topsoil surrounded by loamy sand and sandy loam belts. The spatial distribution of these narrow, elongated soil belts corresponds to paleochannels (or fluvial ridges / alluvial channel deposits), formed by ancient river paths and depositional corridors of the local river network. However, Taramasso et al. (2025) reported that the subsoil beneath the agricultural layer consists of coarse gravel with slightly silty sand and is highly permeable.

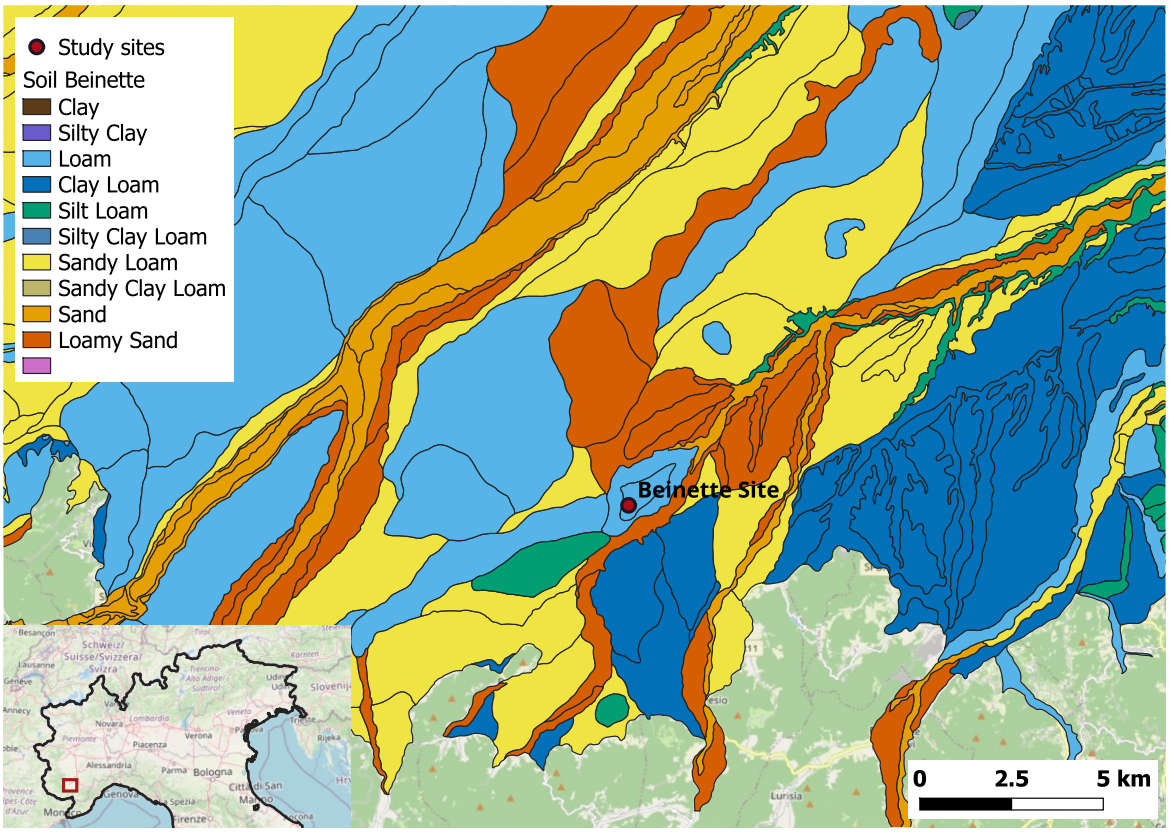


Figure 2.6: Soil classification map of Beinette. Data adapted from Regione Piemonte & IPLA (2017); basemap © OpenStreetMap contributors.

Groundwater table depth (from the ground surface) records from the regional ARPA Piemonte station 00401610001 (Groundwater Body GWB-S7 / Right Stura Bank) for the period from 2001 to 2025 are presented in Figure 2.7. A persistent upward trend in depth to the water table is evident, accompanied by high seasonal fluctuations. Thereby, the regional groundwater depletion trend is clear, characterized by higher seasonal and interannual uncertainties.

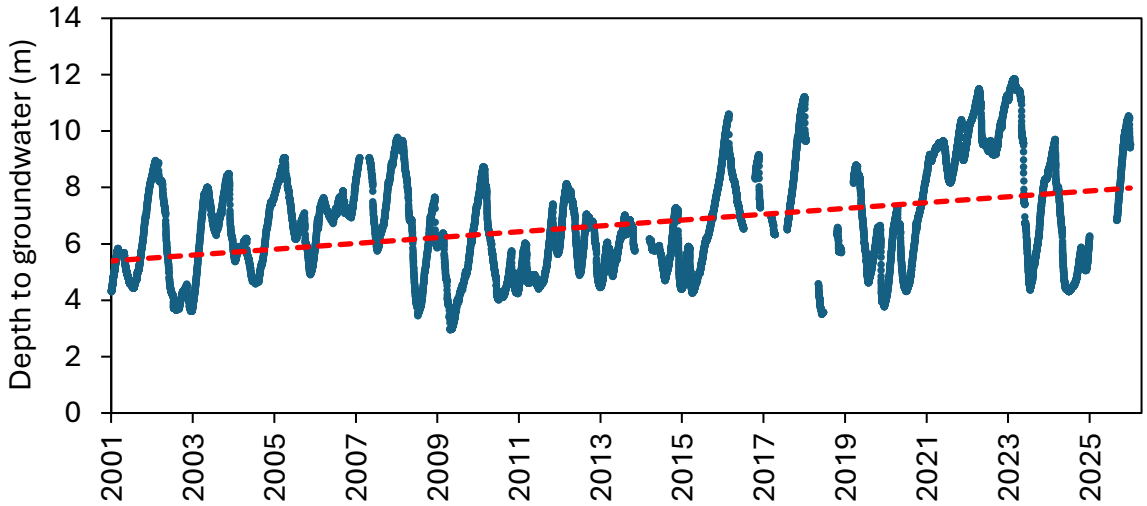


Figure 2.7: Depth to groundwater (soggiacenza, m b.g.s.) of the superficial aquifer (GWB-S7) at monitoring station 00401610001 in in Beinette (2001-2025). The dashed red line represents the linear trend. Data: (ARPA Piemonte, 2025).

The territory surrounding the Beinette site is covered with water-intensive agricultural-lands (Battegazzore & Morisi, 2012). Several rivers, including the Stura di Demonte, Gesso, Colla, and Pesio, interact with the hydrological system by recharging the shallow aquifer of the area through riverbed infiltration losses (Taramasso et al., 2025). Moreover, a dense irrigation canal system exists in the area (Taramasso et al., 2025). With these facts, this study area is suitable for Ag-MAR during the off-season, when agricultural water demand is minimal (Taramasso et al., 2025).

3 Materials and Methods

This chapter details the experimental methodologies with the background theories and materials used in the study. The study progressed from field-based measurements to laboratory-scale experiments designed to meet the research objectives. The fundamental theories are explained first, followed by specific theoretical frameworks introduced alongside their respective procedures.

Following the theoretical background, the herbicide imazamox used in this study is introduced. Then, field infiltration measurements are presented, followed by soil parameterization experiments and column transport experiments. Afterward, the numerical modelling used to interpret hydrodynamic and solute transport parameters is described. Finally, an overview of the entire experimental procedure is presented. Each experiment is assigned a unique identifier for better organization.

3.1 Water Flow and Solute Transport Dynamics

Darcy's law defines the linear relationship between the water discharge Q [L^3T^{-1}] passing through a porous medium of cross-section A [L^2] and the hydraulic gradient i [-], which is the ratio of the water head drop Δh [L] over length L. (Figure 3.1; Sethi & Di Molfetta, 2019).

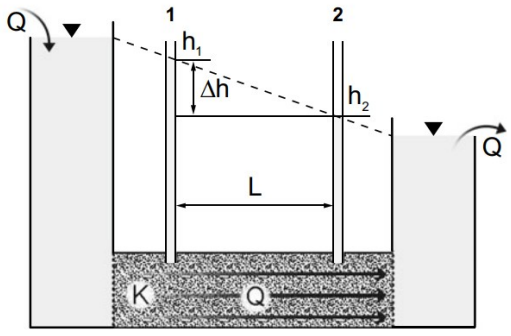


Figure 3.1: Laboratory device used to verify Darcy's law.(Adopted from Sethi & Di Molfetta, 2019)

$$Q = KA\frac{\Delta h}{L} \qquad (1)$$

The discharge across a unit cross-sectional area (Q/A) is called specific discharge, or Darcy velocity q [LT^{-1}]. For one-dimensional vertical flow vertical flow, taking z as the

vertical coordinate directed positive upward, the relationship between q and hydraulic the head gradient ∂H/∂z [-] is formulated in Equation (2) derived from the Darcy's law.

$$q_s = -K_s\left(\frac{\partial H}{\partial z}\right) \qquad (2)$$

where, K_s is the saturated hydraulic conductivity. q_s is the Darcy velocity under saturated conditions. If the soil matrix is not saturated, K is lower than K_s, and is given by Equation (3) (Dane et al., 2002):

$$q = -K(\theta)\left(\frac{\partial H}{\partial z}\right) = -K(h)\left(\frac{\partial H}{\partial z}\right) \qquad (3)$$

where K(θ) [LT^{-1}] and K(h) represent hydraulic conductivity at volumetric water content θ [-] and at pore water pressure head h [L], respectively. K(θ) and K(h) increase with volumetric water content and pore water pressure head (Figure 3.2). Ultimately, the maximum value of both is achieved at saturation-saturated hydraulic conductivity Ks)- which is a soil-specific constant.

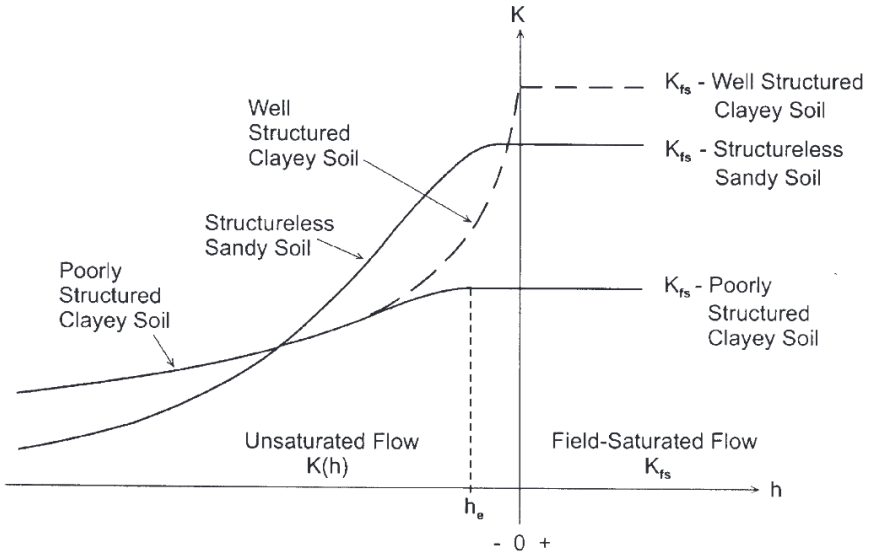


Figure 3.2 Variation of hydraulic conductivity of different soil types with pore water pressure head. (Dane et al., 2002)

In many field applications, fully saturated conditions- where void spaces are completely filled with water- may not be reached due to entrapped air in void spaces. Therefore, field-saturated hydraulic conductivity (K_{fs}), which reflects a quasi-saturated, steady-state condition, is evaluated in the field instead of K_s. While standard field tests measure K_{fs},

prolonged winter flooding may fully saturate the soil over time. However, unless explicitly mentioned otherwise, the difference between K_s and K_{fs} is assumed to be negligible under the scope of this study.

Transient water flow in the soil cannot be described by Darcy's law alone, and hence it cannot represent all flow conditions observed in the laboratory soil column tests. Richards' equation is formulated to represent these transient conditions as well. It is formulated as Equation (4) after simplifying for 1D vertical flow by assuming no sources or sinks in the soil samples and converting the pressure term Ψ [L] into volumetric water content θ (Tosco, 2024c).

$$\frac{\partial \theta}{\partial t} = \frac{\partial}{\partial z}\left(D_W(\theta)\frac{\partial \theta}{\partial z} + K_z(\theta)\right) \qquad (4)$$

where θ [-] is the volumetric water content, z [L] is the vertical coordinate, $K_z(\theta)$ [LT^{-1}] is the unsaturated hydraulic conductivity, $D_W(\theta)$ [L^2T^{-1}] is the soil water diffusivity, defined by Equation (5):

$$D_W = K(\theta)\frac{\partial \Psi}{\partial \theta} \qquad (5)$$

Reactive solute transport through soil matrix under steady-state saturated conditions is governed by the one-dimensional Advection-Dispersion Equation (ADE), (Equation 6; Van Genuchten & Wierenga, 1976).

$$\frac{\rho}{\theta}\frac{\partial S}{\partial t} + \frac{\partial C}{\partial t} = D_S\frac{\partial^2 C}{\partial z^2} - v_0\frac{\partial C}{\partial z} \qquad (6)$$

where C [ML^{-3}] is the solute concentration in the liquid phase, S [$M\ M^{-1}$] is the sorbed concentration on the soil solid phase, ρ [ML^{-3}] is the soil dry bulk density, θ [-] is the saturated volumetric water content, v_0 [LT^{-1}] is the average pore-water velocity, z [L] is the spatial coordinate along the flow direction, and t [T] is time.

Hydrodynamic dispersion coefficient, D_S [L^2T^{-1}], represents the spreading of solute front during advection movement. Hydrodynamic dispersion occurs due to two inseparable mechanisms: molecular diffusion driven by concentration gradients, and mechanical dispersion caused by velocity variations within the porous matrix (Bear, 1988). The D is defined in Equation (7).

$$D_S = \alpha v + \tau D_0 \qquad (7)$$

where D_0 [L^2T^{-1}] is the molecular diffusion coefficient of the solute, τ [-] is the soil tortuosity factor, and v [LT^{-1}] is the pore water velocity. α [L] is the longitudinal dispersivity (α), a fundamental physical parameter that reflects the heterogeneity, pore size distribution and, tortuous pathways of soil matrix (Bear, 1988).

Solving these nonlinear equations with multiple iterations is difficult to solve without computer based numerical models. Therefore, HYDRUS-1D was utilized. The hydrodynamic model adopted for hydraulic parameterization was the van Genuchten–Mualem model (Equation (8); Tosco, (2025); Van Genuchten, (1980)) while the equilibrium solute transport model was used for modelling the tracers and herbicide breakthrough curves to find chemical and physical parameters of solute transport.

$$K(S_e) = K_{sat} S_e^{1/2} \left[1 - \left(1 - S_e^{\frac{1}{m}} \right)^m \right]^2 \qquad (8)$$

where $K(S_e)$ $[LT^{-1}]$ is the unsaturated hydraulic conductivity, K_{sat} $[LT^{-1}]$ is the saturated hydraulic conductivity, S_e [-] is the effective saturation, and m [-] is a dimensionless empirical shape parameter related to n [-] by m = 1 - 1/n (Van Genuchten, 1980). The effective saturation S_e is defined as:

$$S_e = \frac{\theta - \theta_r}{\theta_S - \theta_r} \qquad (9)$$

where θ [-] is the volumetric water content, θ_r [-] is the residual water content, and θ_s [-] is the saturated water content. The determination of these soil-specific parameters is explained in subsequent Section 3.6.1.

Furthermore, measuring the concentration of the compound eluted over time from a soil matrix within a known column geometry allows the quantification of the retardation coefficient R [-] of non-conservative compounds, defined as the ratio of the effective water velocity v_e [LT^{-1}] ($v_e = q/\theta$) to the effective solute velocity v_s [LT^{-1}], as formulated in Equation (10) under linear isotherm conditions (Tosco, 2024b).

$$R = \frac{v_e}{v_s} = 1 + \frac{\rho_b}{\theta} K_d \qquad (10)$$

where ρ_b is the dry bulk density of the soil, C is the solute concentration in water, and K_d [L^3M^{-1}] is the soil distribution coefficient, defined in Equation 11. After the evaluation of K_d, the organic carbon-normalized adsorption coefficient K_{oc} [L^3M^{-1}] was calculated using

Equation 12 (Karickhoff et al., 1979), enabling a direct comparison with established literature values.

$$S = K_d \,.\, C \tag{11}$$

$$K_{oc} = \frac{K_d}{f_{oc}} \tag{12}$$

where S [-] and C [ML^{-3}] are solute concentration in soil and liquid phase, respectively with S defined as mass of solute adsorbed per unit mass of dry soil. f_{oc} [-] is fraction mass of organic carbon in the soil.

3.2 Imazamox

Imazamox is a widely used herbicide applied in Clearfield® rice cultivation, which accounts for approximately 20% of the total rice-growing area in northwestern Italy (Scarabel et al., 2012). It is typically applied twice per growing season (Scarabel et al., 2012). Therefore, this compound is a critical agrochemical that is worth investigating in a feasibility study of Agricultural Managed Aquifer Recharge (Ag-MAR).

Imazamox exhibits a weak sorption affinity (K_{oc}= 2-130 mL/g for the parent compound; 5-88 mL/ g for its diacid metabolite), making it highly mobile in soil matrices (Buerge et al., 2019). Furthermore, its aerobic degradation half-life is strongly pH dependent, ranging from 1.8-5.1 days in neutral soils to over 120 days in acidic conditions (Buerge et al., 2019). Under intense infiltration in winter flooding, the hydraulic retention time in unsaturated vadose zone is short. This low sorption capacity, combined with short brief contact time poses a significant risk of un-degraded imazamox leaching into shallow aquifer.

3.3 Field Infiltration Tests

Rapid evaluation of hydraulic conductivity in the field was achieved by in-situ infiltration tests. The reliability of the results depends on the suitability of the infiltration method for the site-specific soil conditions. Therefore, initially, two infiltration test methods were performed to compare their performance in the study area, allowing subsequence studies to adopt the most suitable one.

A total of eight field infiltration tests were conducted. Constant-head infiltration tests were performed at Location 2 in Mortara (Figure 3.3) and at Location 1 in Beinette (Figure 3.4). In addition, two falling-head infiltration tests were conducted at Location 1 and 2 in Beinette. At Locations 3 and 4 in Mortara, two single-ring falling-head infiltration tests were performed per location; one at the ground surface and second inside an excavated pit to evaluate the continuous soil profile.



Figure 3.3: Field infiltration and soil sampling locations at the Mortara study site. Irrigation canals adapted from Regione Lombardia (2022); satellite basemap: Imagery © Google



Figure 3.4: Field infiltration test locations at the Beinette study site. (satellite basemap: Imagery © Google)

3.3.1 Constant-Head Single-Ring Infiltration Test (F-C)

The experimental setup consists of a ring with a diameter of 30.0 cm connected to a Mariotte reservoir by two conduits. The ring was driven into the ground at a flat surface. The primary conduit is for downward water flux, while the secondary one is for air intake into the reservoir (Figure 3.5). The constant water head in the ring is governed by the elevation of the secondary conduit's lower orifice. The timer was initiated when water level touched this level, verified by visual inspection through the transparent upper plate of the ring. During the infiltration, reservoir drawdown was recorded over time to evaluate the infiltration flux into the soil. The volumetric water content (θ) of the soil was measured by using a Time-Domain Reflectometer (TDR) probe before and after the test.



Figure 3.5: Single-ring, constant-head infiltration setup with the ring and Mariotte reservoir couple via 2 conduits.

Data were analysed assuming both steady-state and transient flow conditions. By comparing the experimental data against the theoretical models, the actual infiltration regime was identified and selected for the final evaluation.

3.3.1.1 Constant-Head Single-Ring infiltration test - steady state flow

The infiltration rate is a constant under steady state conditions resulting a linear regression with time (Figure 3.6; Dane et al., 2002). The slope of the cumulative infiltration curve over time yields the steady infiltration rate or Darcy velocity q [LT^{-1}], which is adopted for subsequent calculations in Equation (13).

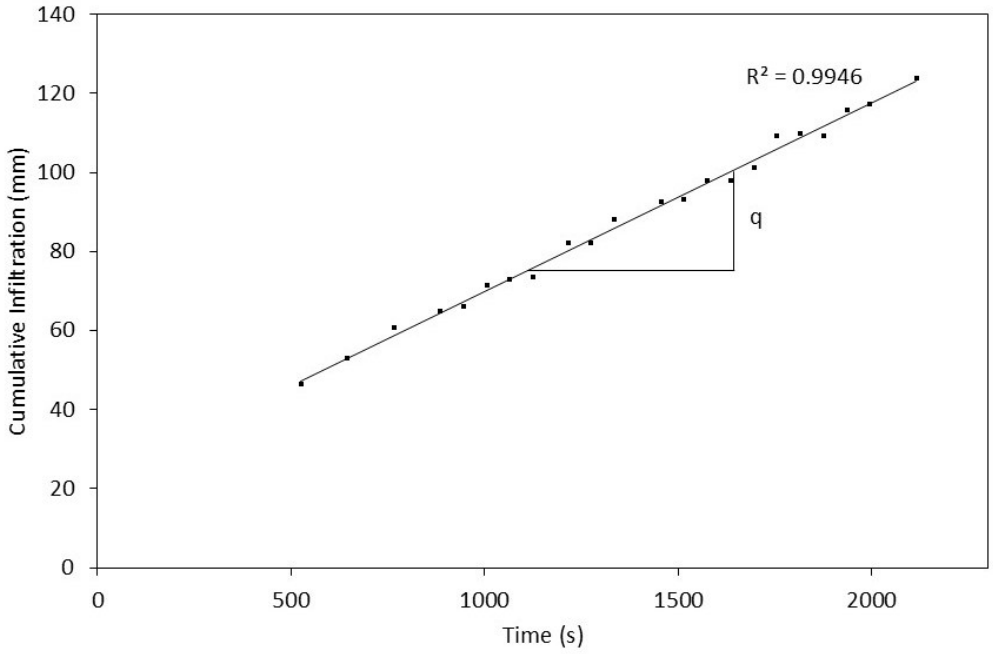


Figure 3.6 : Cumulative infiltration (I) plotted against the time (t) during the single-ring, constant-head infiltration test at Location 2 at the Mortara site. The slope of the linear regression line (mm/s) represents the infiltration rate or Darcy velocity (q)

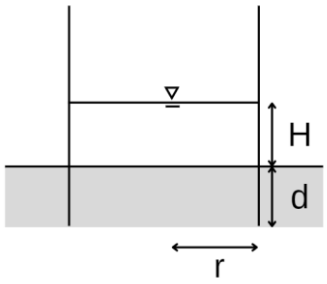


Figure 3.7: Field infiltration setup diagram with key parameters. H: Hydraulic head, d: insertion depth, r: ring radius.

$$Q_s = \frac{r}{G}\left(K_{fs}H + \varphi_m\right) + \pi r^2 K_{fs} \qquad (13)$$

$$G = 0.316\frac{d}{r} + 0.814 \qquad (14)$$

where Q_s [L^3T^{-1}] is the steady discharge, is expressed as $Q_s = q.A$, where A [L^2] is the cross-sectional area of the ring. Unlike laboratory infiltration tests, water flows laterally upon exiting the ring due to capillary effect. G [-] is used to compensate for this effect and the boundary conditions (Reynolds & Elrick, 1990). Parameters d [L] and r [L] are ring insertion

depth and ring radius, respectively. φ_m $[L^2T^{-1}]$ is the matric flux potential, defined as (Reynolds & Elrick, 1990):

$$\varphi_m = \frac{K_{fs}}{\alpha^*} \qquad (15)$$

where α^* is the inverse of microscopic capillary length and was not measured; instead, substituted by a representative value for the specific soil category was adapted from Reynolds & Elrick (1990).

Substituting Equation 14 and 15 into the Equation 13 and isolating K_{fs}, Equations 16 is obtained to determine the field saturated hydraulic conductivity K_{fs} .

$$K_{fs} = \frac{Q_s}{\frac{r}{G}\left(H+\frac{1}{\alpha^*}\right)+\pi r^2} \qquad (16)$$

3.3.1.2 Constant-Head, Single-Ring infiltration test - Transient flow

The early-stage infiltration under transient condition mainly driven by the capillary effect occurs before the establishment of a constant infiltration rate. The procedure proposed by Odell et al., 1998 was used to evaluate infiltration behaviour during this transient phase. Within this framework, cumulative infiltration is expressed as a function of the square root of time as formulated in Equation 17:

$$I = S_H \sqrt{t} \qquad (17)$$

where the parameter I [L] is the cumulative infiltration, S_H [$LT^{-1/2}$] is the soil sorptivity for a given ponded head H [L], and t [T] is time.

The slope of the curve of cumulative infiltration against the square root of the time (Figure 3.8) is equal to the sorptivity for the experimental ponded water head. Subsequently the equation 18 and 19 were applied to evaluate K_{fs}.

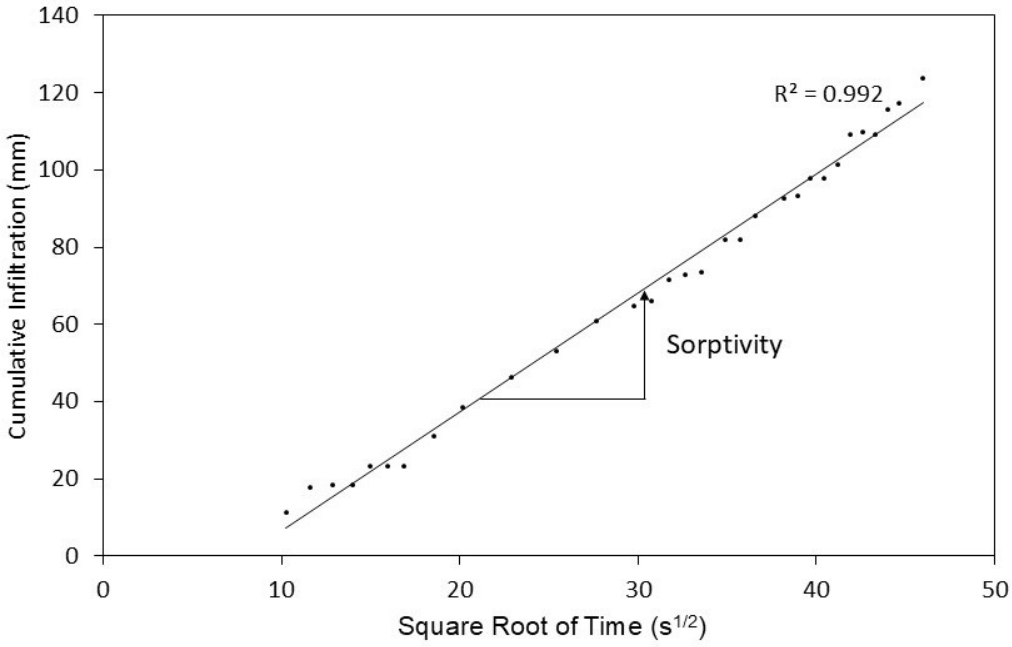


Figure 3.8: Cumulative infiltration (I) plotted against the square root of time ($\sqrt{t}$) during the single-ring, constant-head infiltration test at Location 2 at the Mortara site. The slope of the linear regression line (mm/s$^{1/2}$) represents the soil sorptivity.

$$S_H = \sqrt{2\Delta\theta K_{fs} H + S_0^2} \tag{18}$$

$$S_0 = \left(\frac{(\Delta\theta)\varphi_m}{b}\right)^{\frac{1}{2}} \tag{19}$$

Where the parameter $\Delta\theta$ [-] is the difference between final and initial volumetric water content, $S_0[\mathrm{LT}^{-1/2}]$ is the sorptivity under zero ponding head, and b [-] is an empirical constant taken as 0.55 for all soil. Substituting Equations 15 and 19 into Equation 18 allows K_{fs} to be expressed as:

$$K_{fs} = \frac{S_H^2}{\Delta\theta\left(2H + \frac{1}{0.55\alpha^*}\right)} \tag{20}$$

3.3.2 Falling-Head Single-Ring Infiltration Test

The setup of this test consists of a water level sensor (Levelogger), a barometric sensor (barologger) and a ring (Figure 3.9). The ring was driven into the ground at a flat surface. The levelogger and barologger was programmed to record water level and atmospheric pressure in regular intervals. Consequently, water was filled and allowed to infiltrate. The

experimental duration was set to approximately 2.5 hours, except in cases where high soil permeability led to complete water depletion earlier.



Figure 3.9: Single-ring, falling-head infiltration setup before filling.

The interpretation method proposed by (Nimmo et al., 2009) is based on Equation 21:

$$L_G \, ln\left(\frac{L_G+\lambda+H_0}{L_G+\lambda+H}\right) = K_{fs}t \tag{21}$$

$$L_G = C_1 d + C_2 r \tag{22}$$

where the parameter L_G [L] is ring-installation scaling length, λ is the capillary length scale, H is the ponded depth at time t [L], H_0 is the initial ponded depth, and C_1, C_2 are empirically determined constants.

λ was adopted from White & Sully, (1987) as recommended in the procedures of (Nimmo et al., 2009). The dimensionless constants C_1 and C_2 were adopted from (Reynolds & Elrick, 1990).

The left side of the equation 21, Y [L], was calculated for each reading and plotted against time (Figure 3.10); the slope of the fitted linear trendline corresponds to the field-saturated hydraulic conductivity (K_{fs}).

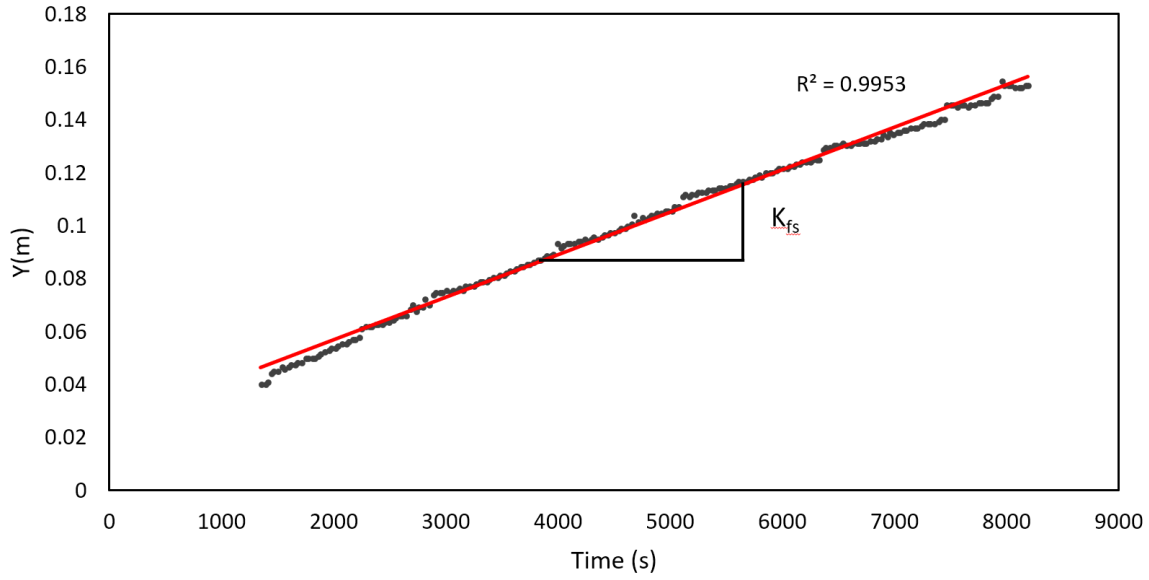


Figure 3.10: Left-hand side of Equation 20 plotted against time for the shallow falling-head infiltration test at Mortara Location 3. The slope corresponds to the field saturated hydraulic conductivity K_{fs}.

3.4 Soil Sampling

Soil samples were collected using two different methods for two different purposes. Loose soil core samples were taken for granulometric analysis and to measure total organic carbon. Sampling was conducted using an Edelman auger (Figure 3.11), which was manually rotated into the soil profile to extract trapped bulk soil material.

Undisturbed soil cores were taken in transparent plastic liners (Figure 3.11) for subsequent infiltration and solute transport column experiments. The plastic liner was placed in the undisturbed soil sampler and secured with the end cap. After attaching the handle, it was driven into the soil profile using a combination of vertical hammering and continuous unidirectional rotation.

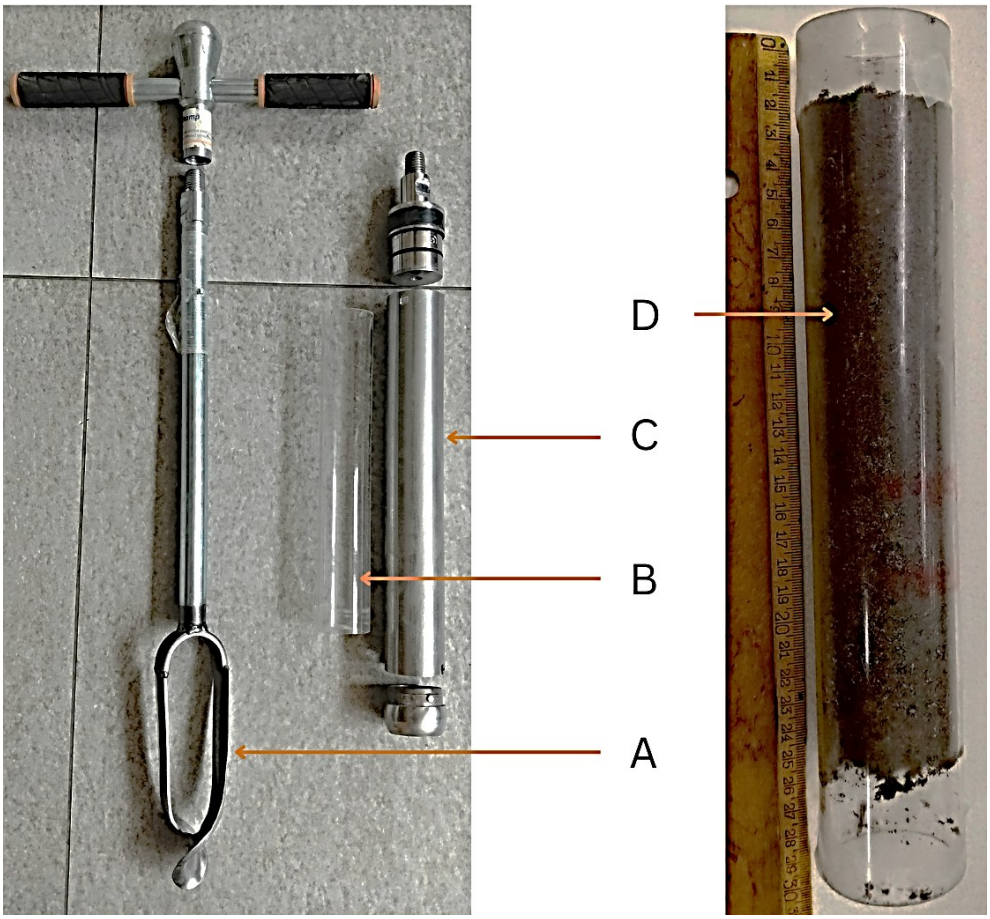


Figure 3.11: Soil sampling equipment and core extraction: (A) Edelman auger, (B) Empty transparent plastic liner for undisturbed soil core sample, (C) Undisturbed soil core sampler, (D) Undisturbed soil sample.

Undisturbed soil cores were collected from fields at the same locations where field infiltration tests were conducted. In total, nine undisturbed soil cores were taken; one sample was from Beinette other 8 samples were from Mortara site. Two shallow samples were collected at each sampling location 1 and 2. One shallow sample and one deep sample were collected at each location 3 and 4 (Figure 3.3). Deep samples were taken beneath the shallow sample holes to represent continues vertical soil profile. In total, seven loose samples were taken corresponding to the soil core locations. The sampling depth of each soil core sample is presented in Table 3.1.

Table 3.1:Details of soil samples

Sample Code	Sampled Date (DD/MM/YYYY)	Sample Location/ Site	Condition	Sampling Depth (cm)
U-B	31/03/2026	Beinette	Undisturbed	0-20
U-M1A	11/03/2026	Mortara 1	Undisturbed	0-18
U-M1B	11/03/2026	Mortara 1	Undisturbed	0-18
U-M2A	11/03/2026	Mortara 2	Undisturbed	0-21
U-M2B	11/03/2026	Mortara 2	Undisturbed	0-21
U-M3S	19/05/2026	Mortara 3	Undisturbed	0-20
U-M3D	19/05/2026	Mortara 3	Undisturbed	20-38
U-M4S	19/05/2026	Mortara 4	Undisturbed	0-23.5
U-M4D	19/05/2026	Mortara 4	Undisturbed	23.5-45.5
D-B1	31/03/2026	Beinette 1	Disturbed	0-20
D-M1	11/03/2026	Mortara 1	Disturbed	0-18
D-M2	11/03/2026	Mortara 2	Disturbed	0-21
D-M3S	19/05/2026	Mortara 3	Disturbed	0-20
D-M3D	19/05/2026	Mortara 3	Disturbed	20-38
D-M4S	19/05/2026	Mortara 4	Disturbed	0-23.5
D-M4D	19/05/2026	Mortara 4	Disturbed	23.5-45.5

Soil samples were sealed immediately after sampled to preserve water content in the field condition. Upon return to the lab, they were kept in refrigerator to preserve field conditions until they were used.

3.5 Laboratory Tests

The laboratory experiments were conducted in three stages: preliminary column test, soil characterization and primary column test. Preliminary column tests were performed to identify potential operational challenges and refine the experimental procedure, establishing a well-defined expected workflow for the main experimental stage.

Two soil columns collected from Locations 1 and 2 at the Mortara site were tested during preliminary stage. Only the saturation and the tracer test phases, explained in subsequence Sections 3.5.9 and 3.5.10, were included for the preliminary column tests. Only KBr was used as a tracer at concentrations of 100 mmol/L for the Location 1 column test, and 27.8 mmol/L for the Location 2 column test.

The second stage was soil characterization and tracer evaluation to validate their compatibility. Subsequently, the main stage comprised soil column tests conducted simultaneously using two parallel columns. The procedures and materials for these two stages are explained in this section.

3.5.1 Dry Density and Residual Volumetric Water Content

Dry density ρ_d [ML^{-3}] and initial volumetric water content θ_i [-] of each column core sample were measured before they were used for the infiltration test. A known length of soil core was removed at the bottom of the cylinder (Figure 3.12). The removed sample was weighed, dried in the oven and then weighed again. ρ_d and θ_r were evaluated using Equation 23 and 24.

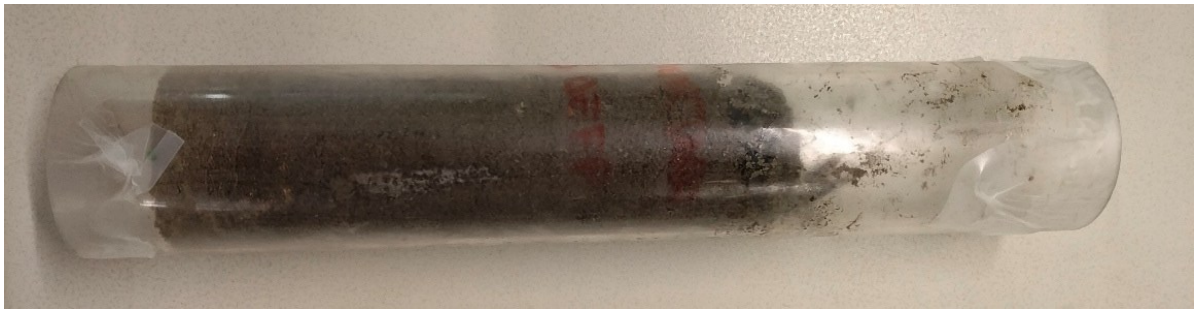


Figure 3.12: A Column core sample after removing a soil layer for evaluating θ_r and ρ_d.

$$\rho_d = \frac{m_2}{V} \qquad (23)$$

$$\theta_i = \frac{\left(\frac{m_1 - m_2}{d_w}\right)}{V} \qquad (24)$$

where the parameter m_1 [M] is the weight before drying, m_2 is the weight after drying, d_w [ML^{-3}] is the density of water, V [L^3] is the removed soil volum.

3.5.2 Total Organic Carbon (TOC) Measurement

Total Organic Carbon (TOC) was determined in two stages by measuring Total Carbon (TC) and Inorganic Carbon (IC). Prior to analysis, the soil samples were dried at 60 ℃ for 24 hours to remove moisture and obtain measurements in dry basis while preserving volatile organic matter.

A Shimadzu TOC-L Analyzer equipped with SSM-5000A Solid Sample Combustion Unit (Figure 3.13) was used, following the procedure proposed by (Tanaka, 2023). A Previously established calibration curve was utilized after validation with a pure glucose standard.

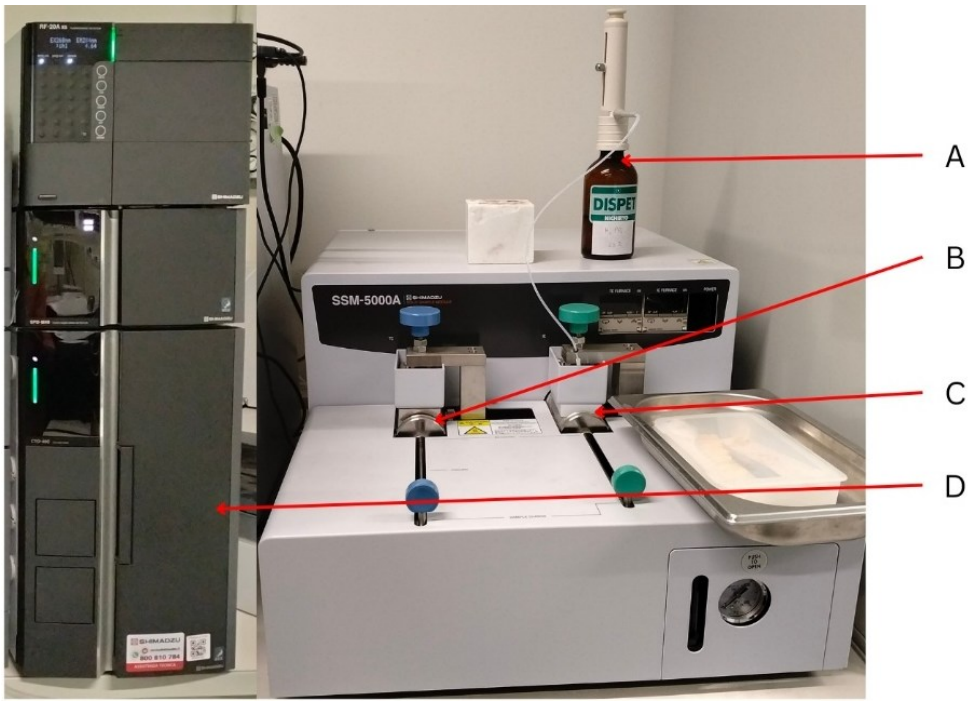


Figure 3.13: Shimadzu TOC analysis setup comprising the SSM-5000A Solid Sample Combustion Unit (right) and the TOC-L Main Unit (left tower, D); (A) Phosphoric Acid (H_3PO_4) Dispenser, (B) TC Combustion Port, (C) IC Reaction Port.

Soil samples were weighed and placed into combustion boats that were preconditioned by combustion unit, then combusted at 900 ℃ in a high-purity oxygen atmosphere to measure TC. TOC-L Analyser detected CO_2 and generated a graph of CO_2 concentration over time. The area under the curve represented the TC, and the actual TC value was calculated using the calibration curve while accounting for the initial sample weight.

To determine IC, samples were treated with H_3PO_4 to convert carbonates into CO_2, then immediately inserted into combustion unit and heated to 200℃ to rapidly release the trapped CO_2. Following the same procedure as the TC measurement, IC was quantified based on released CO_2.

TOC was calculated by subtracting IC from TC, as expressed in Equation 25.

$$TOC = TC - IC \quad (25)$$

3.5.3 Granulometric Analysis

Loose soil samples collected at each location were used for granulometric analysis after drying in the oven at 105 ^{0}C for 15 hours. Then they were sieved using sieves of different mesh sizes standardized by the ASTM. Sieve sizes of 2.00, 1.40, 1.18, 0.600, 0.425, 0.300, 0.150, 0.075, 0.053, 0.045 millimetre and a pan were used. Consequently, the soil particles retained on each sieve were weighed to evaluate the percentage passing of soil particles to construct particle size distribution curves and classify the soil with USDA Triangle (Van Lear, 2024) based on three particle size categories. These size boundaries were identified according to Soil Science Division Staff, (2017) as sand (0.05-2. 0mm), silt (0.002-0.05 mm), and clay (<0.002mm).



Figure 3.14 Mechanical sieve shaker used for granulometric analysis.

3.5.4 Effluent and Soil Solution Preparation

Effluent is the solution eluted from the soil column after passing through the soil matrix. Soluble compounds and ions present in the soil are released into this solution; therefore, effluent exhibits different chemical properties than influent water. Additionally, the subsequent agglomeration analysis was performed using a synthetic effluent, meaning water did not actually flow through the soil column. Instead, soil and water were mixed at a 1:3 weight ratio. Then, the mixture was allowed to stand for 5 minutes to facilitate separation, and the supernatant was collected. Afterward, centrafiguration was performed to further separate suspended particles.

3.5.5 KBr Tracer Calibration

Bromide (Br^-) and most soil particles are negatively charged making soil particles repel Br^- ions. This phenomenon makes in minimal adsorption of Br ion onto soil particles. Therefore, it behaves as a conservative tracer meaning that it travels through pores at nearly the same rate as water.

One of the simplest and fastest methods to determine the concentration of KBr is to measure electrical conductivity (EC). However, as water flows through the soil matrix, native soil ions are released into the solution introducing background noise to the EC measurements. Therefore, initially, only deionized water was allowed to flow through the soil matrix and the background electrical conductivity (EC_{sat}) was measured. Subsequently, KBr solutions of known concentrations ranging up to 100 $mmol.L^{-1}$ were prepared using this soil-contacted water (Effluent), after which the EC of each solution (EC_{ef}) was measured. The net electrical conductivity induced by KBr ($\Delta EC = EC_{ef} - EC_{sat}$) was plotted against the KBr concentration to establish the calibration curve (Figure 3.15).

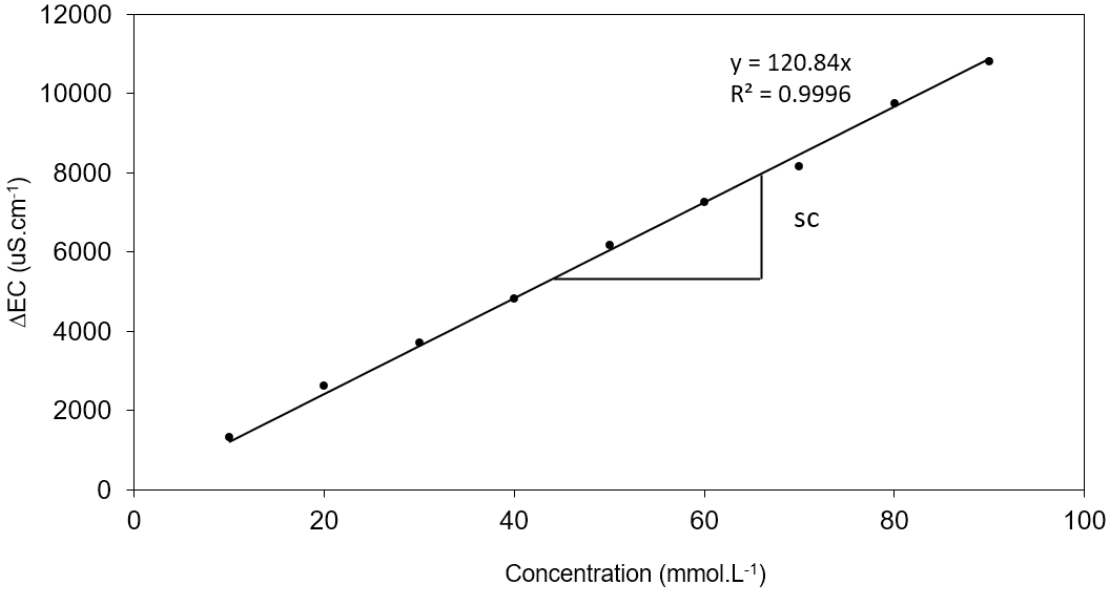


Figure 3.15: Calibration curve of KBr.

Consequently, the concentration of KBr in a sample is calculated by the equation 26.

$$Concentration = \frac{EC_{ef} - EC_{sat}}{sc} \qquad (26)$$

where EC_{ef} is the electrical conductivity of the sample, EC_{sat} is the soil-specific background electrical conductivity, and sc is the slope of the calibration curve.

3.5.6 Fluorescein and Rhodamine Calibrations

Fluorescein and Rhodamine are fluorescent dyes widely used as tracers in the field of hydrology to track water movement. However, their individual characteristics, their interactions with the soil matrix and their mutual interaction with each other were evaluated based on their absorption spectra prior to preparing calibration curves.

A spectrophotometer (Figure 3.16) was used to evaluate absorption spectra and concentrations of each dye in solutions. The instrument's lamp emits light and directs it through a cuvette containing dye solution. The solution absorbs light at specific wavelength where the absorbance is proportional to the concentration of the dye according to the Beer-Lambert law (Equation 27).

$$A = \varepsilon \times c \times l \qquad (27)$$

where the parameter A is the absorbance [-], ε is the molar absorptivity [L^2N^{-1}], c is the concentration [NL^{-3}] and l is the path length [L].

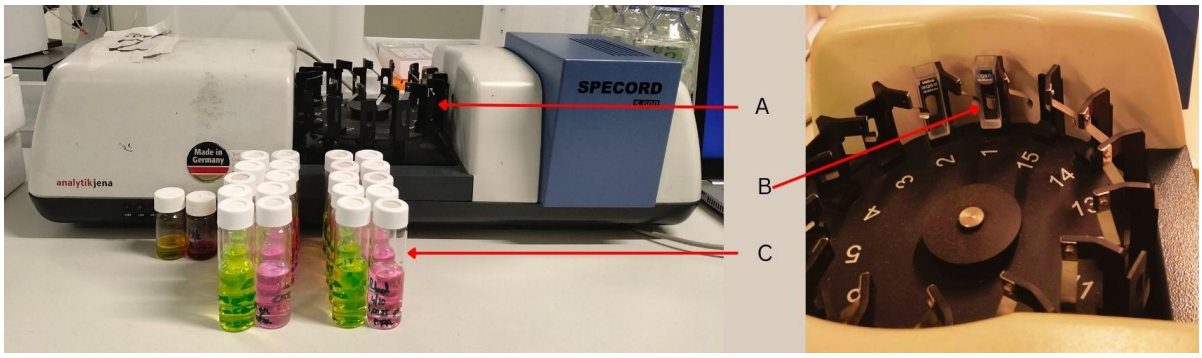


Figure 3.16: Spectrophotometer setup; (A) rotary cuvette carousel, (B) sample loaded in a standard cuvette, and (C) prepared sample solutions prior to measurement.

The wavelength of peak absorbance (λ_{max}) is characteristic of the specific compound dissolved in the solution. If multiple absorbing compounds are present, multiple absorption peaks appear. (Figure 3.17).

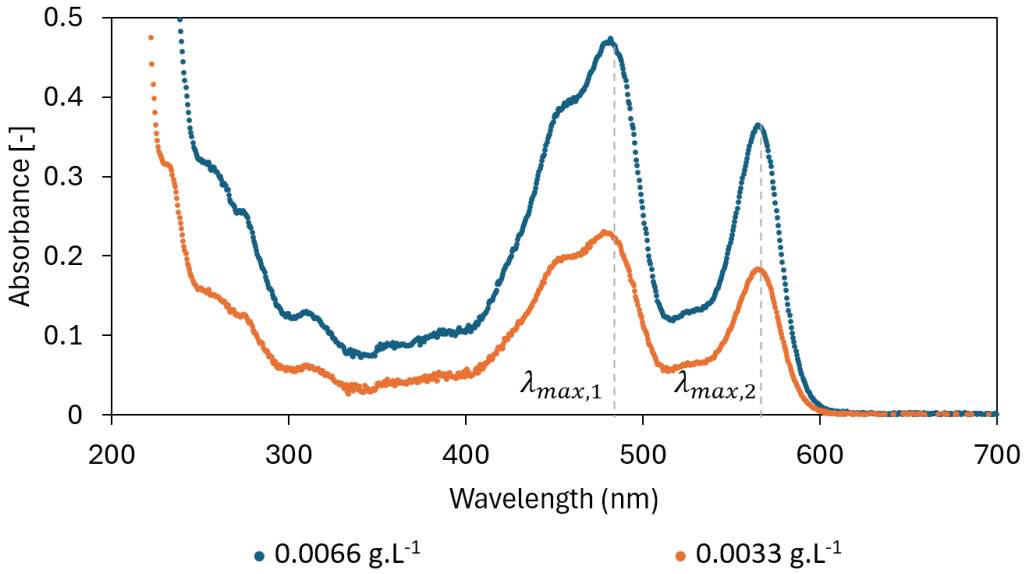


Figure 3.17: Absorbance spectra of two multi-tracer solutions containing 0.3966 g.L^{-1} KBr with mixed Fluorescein and Rhodamine. Both dyes were present at equal concentrations in each respective mixture (0.0066 g.L^{-1} and 0.0033 g.L^{-1}). Dashed lines indicate the characteristic absorption peaks of Fluorescein ($\lambda_{max,1}$) and Rhodamine ($\lambda_{max,2}$)

In the first stage, each dye was prepared separately at different concentrations diluted in deionized water. The tested concentration ranges for Rhodamine (0-0.018 g.L^{-1}) and Fluoresceine (0.016 g.L^{-1}) were chosen to fall within the linear absorbance measurement range. Their absorbances at their specific wavelengths were measured and plotted

against the concentration to construct their calibration curves. In the second stage, the tracer solutions were diluted in soil-contacted deionized water (effluent), and their initial procedure was repeated to identify their interactions with effluent. In the third stage, the procedure was repeated by mixing them together in the same concentrations of Fluorescein and Rhodamine diluted in deionized water and, subsequently in effluent to evaluate their mutual interactions as well as their interactions with the soil matrix. Then, all the previous stages were repeated by additionally adding KBr to evaluate its impact on Fluorescein and Rhodamine.

3.5.7 Agglomeration Tests

Agglomeration tests was performed to evaluate the potential flocculation of the soil fine fraction in pore water upon contact with the tracers, as formation of aggregates can lead to partial clogging of the soil matrix, altering permeability and flow paths. Fine particulate aggregates were visually observed in the 11.90 $g.L^{-1}$ KBr solution after contact with soil matrix (Figure 3.18). Consequently, Dynamic Light Scattering (DLS) analysis was conducted to evaluate the degree of particle agglomeration as a function of KBr concentration and time, thereby determining an optimal concentration for subsequent tracer tests to prevent pore blockage while enabling the detection of subtle changes in relative concentration.



Figure 3.18: Effluent from Mortara 1 column after KBr injection

A dynamic light scattering (DLS) instrument operates by illuminating the sample with a monochromatic light beam and measuring the scattered light intensity over time (Stetefeld et al., 2016). The Brownian motion-constant random movement due to thermal collisions with solvent molecules-of particles causes Doppler broadening and fluctuations in the scattered light intensity over time, allowing precise measurements (Stetefeld et al., 2016).

The analysis focused on three main parameters.

1. Z-Average – The Z-average represents the average hydrodynamic diameter of the particles. An increase in Z-average indicates agglomeration. (Jia et al., 2023)
2. Polydispersity index (PDI) – PDI indicates width and heterogeneity of particle size distribution. Low PDI means narrow and more uniform distribution, whereas an increase in PDI suggests variation in particle size distribution due to agglomeration. (Jia et al., 2023)
3. Average Count Rate – The average count rate (measured in kcps) represents the overall intensity of scattered light from suspended particles. A decrease in count rate over time indicates gravitational settling (sedimentation) of larger aggregates out of the measurement zone.

Five samples were prepeared by varying the added components. All the samples were prepared in the synthetic effluent, which was obtained following the procedures explained in Section 3.5.4:

1. Soil extract (deionized water equilibrated with the soil matrix)
2. Soil extract with 0.595 $g.L^{-1}$ KBr
3. Soil extract with rhodamine 0.01 $g.L^{-1}$
4. Soil extract with rhodamine 0.01 $g.L^{-1}$ and 0.595 $g.L^{-1}$ KBr
5. Soil extract with 1.190 $g.L^{-1}$ KBr

DLS analysis was conducted for four consecutive days. Every day, the samples were shaken before transferring them to the cuvette to replicate the same conditions each day. Replicate measurements were obtained at each time point for each sample. Z-average, PDI and average count rate were calculated as the average of those replicates.

3.5.8 Preparing Soil Cores for Colum Tests

Column tests were conducted in two stages: preliminary and primary. The preliminary study was performed to identify unforeseen operational challenges and experimental duration to better prepare for the primary column tests. The soil column test had three phases in this study: saturation, tracer tests and imazamox transport experiments.

The undisturbed soil cores collected in the field and used for measuring dry bulk density and initial water content were utilized for this procedure. A mesh filter was placed at the base of the column to prevent fine particles from migrating and blocking the drainage outlet (Figure 3.19). The end cap equipped with a drainage orifice was subsequently installed and a flexible plastic tube was connected to direct effluent drops to the sample collection containers.

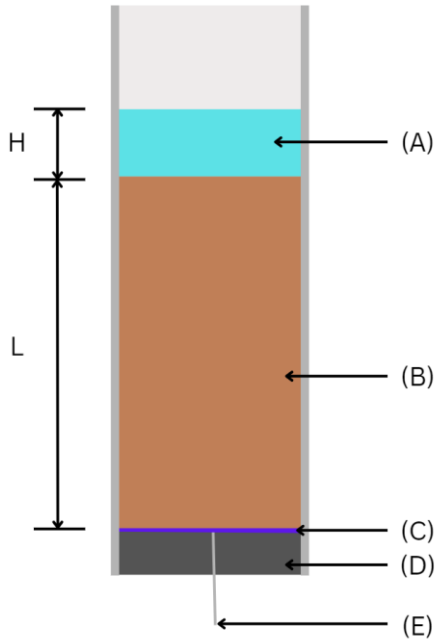


Figure 3.19: Soil Core sample prepared for infiltration and tracer testing. ***(A)*** *Ponding water layer;* ***(B)*** *Soil matrix;* ***(C)*** *Filter;* ***(D)*** *End cap;* ***(E)*** *outflow pipe.*

3.5.9 Soil Column Saturation Phase

The saturation phase was conducted by continuous deionized water injection under a constant water head. The primary objective was to completely fill all available soil voids except for those containing trapped air, thereby ensuring that solute transport occurred in subsequence tracer test under uniform, steady-state flow conditions.

The water head at the top of sample was sustained with a ponding water layer, to simulate field flooding at constant ponded head, by a Mariotte bottle which had two conduits (Figure 3.20). One conduit was connected to the ponding water layer. The second pipe was left open to the air. The ponding water level was adjusted according to the level of the lower end opening of the second conduit. The outflow rate was measured by a digital scale connected to a laptop which recorded readings every minute. Deionized water was allowed to flow until a constant water flow rate was established, thereby completing the saturation phase.

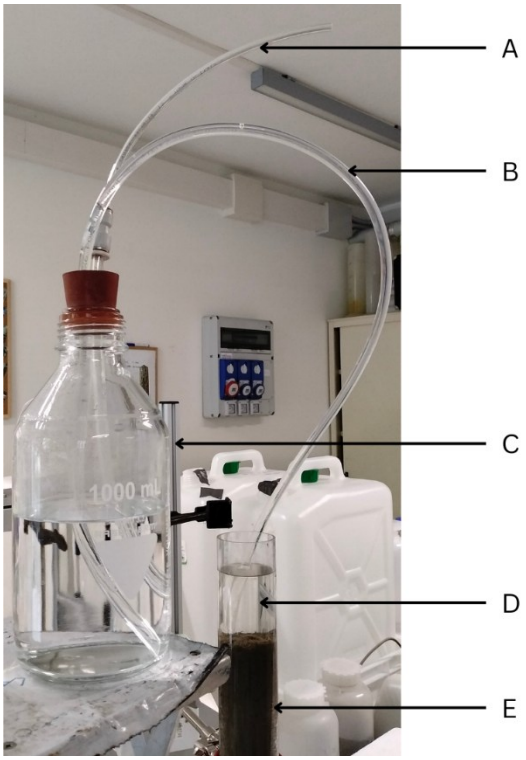


Figure 3.20: Mariotte bottle setup maintaining a constant ponded water layer. (A) Atmospheric conduit. (B) Inflow conduit connected to ponding water layer with Mariotte bottle. (C) Reservoir. (D) Ponding water layer. (E) Soil column

3.5.10 Column Tracer Experiments

The aim of the tracer test was to evaluate saturated volumetric water content (θ_s) [-] and dispersivity α [L]. Tracers diluted in deionized water at a known concentration were injected under a constant water head using the Mariotte bottle (Figure 3.21). To minimize measurement errors caused by background Electrical Conductivity fluctuations in the effluent, a sufficiently high KBr concentration was desirable. However, because the preliminary experiments showed column blockage following KBr injection, the concentration was kept at a lower, acceptable level of 10 mmol/L in the primary test. Rhodamine was also included alongside KBr at a concentration of 0.016 g/L, corresponding to the upper level of the spectrophotometer's linear measurement range, ensuring accurate quantification even at lower relative concentrations.

The solution containing both tracers was filled into the Mariotte bottle. Consequently, following the same procedure as saturation, the tracer solution was injected into the soil matrix while maintaining a constant ponding layer thickness to replicate identical hydrodynamic boundary conditions.

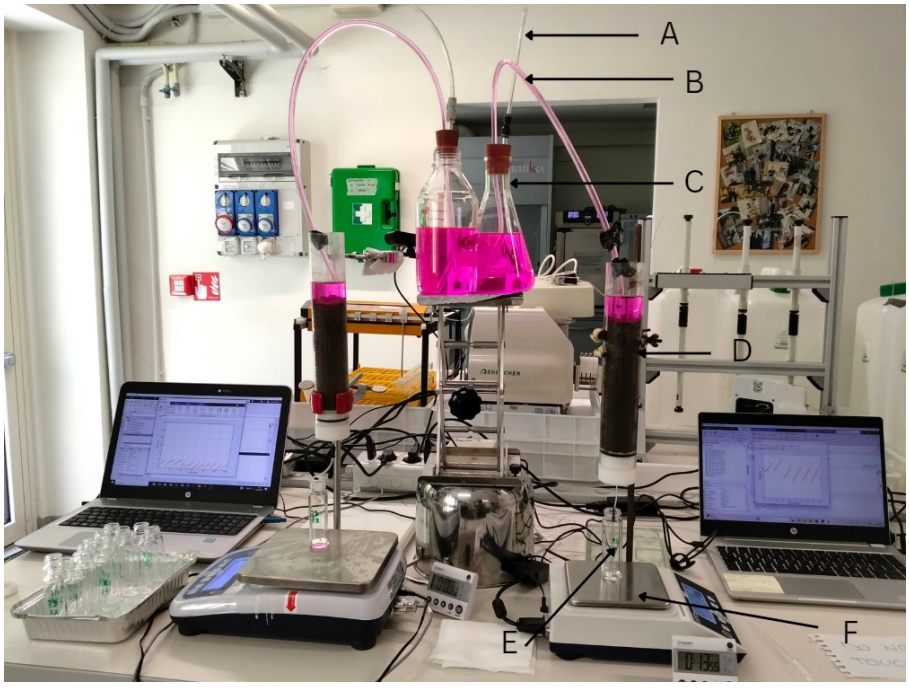


Figure 3.21: The Setup for two tracer tests in parallel. ***(A)*** *Atmospheric conduit;* ***(B)*** *Inflow conduit connected to ponding water layer with Mariotte bottle;* ***(C)*** *Mariotte bottle;* ***(D)*** *Core soil sample;* ***(E)*** *Sample collecting vial;* ***(F)*** *Digital scale connected to a laptop.*

Effluent samples -the solution eluted through the soil matrix in the column- were collected from the start of tracer injection, and the concentration of each tracer in the was measured concurrently. The effluent was continuously collected in vials, and weighed to record outflow rate over time. Time interval for individual samples was determined according to the rate of change in relative concentration. If the relative concentration changed rapidly, the sampling duration was reduced to obtain a smooth breakthrough curve. Effluent samples were automatically collected overnight at fixed time intervals using a fraction collector equipped with a peristaltic pump.

The injection of tracers was continued until the breakthrough curve established a plateau at the relative concentration near unity ($C/C_0=1$ where C is the effluent tracer concentration and C_0 is the input injection concentration). The Mariotte bottle solution was then switched to deionized water to flush the tracers remained in the soil matrix. The breakthrough curve was constructed by plotting the relative concentration against time. Tracer flushing was continued until the relative concentration reached near zero and remained stable over time. Following completion of the breakthrough curve, the ponded water layer at the top was removed, and the column was allowed to drain to prepare it for the subsequent imazamox mobility test.

3.5.11 Imazamox Transport Experiments

The objective of this column test was to determine the soil distribution coefficient (K_d) and the organic carbon-normalized adsorption coefficient (K_{oc}). To simulate realistic field conditions, the herbicide was applied onto drained soil and allowed to reside for a few hours then columns were flushed with deionized water under a constant water head at the top. A mass of 40 mg of Imazamox was applied to each column test to ensure reliable detection in effluent.

Once flushing began, the effluent was collected and weighed. Soil cores were flushed until the imazamox concentration in the effluent reached zero. The effluent was subsequently filtered through a 0.45 µm PTFE filter and transferred into vials for High-Performance Liquid Chromatography (HPLC) analysis.

HPLC separates compounds using a stationary solid phase and a mobile liquid phase. The sample solution is pumped at high pressure through the solid phase packed in a column. Due to differential interactions between the stationary and mobile phases, individual compounds elute at distinct retention times, allowing accurate detection and quantification via light absorbance without interference.

To measure imazamox concentration, a calibration curve was constructed using measurements of known concentrations across the range of 0-200 $mg.L^{-1}$. Detection and quantification of imazamox were carried out using a HPLC system utilizing a C18 analytical column. On this column, the retention time of imazamox was 6.2 min (Figure 3.16). The Photodiode Array detector detected imazamox at 247 nm wavelength. The area under the peak in the chromatogram of absorbance against retention time (Figure 3.23) was proportional to the concentration.

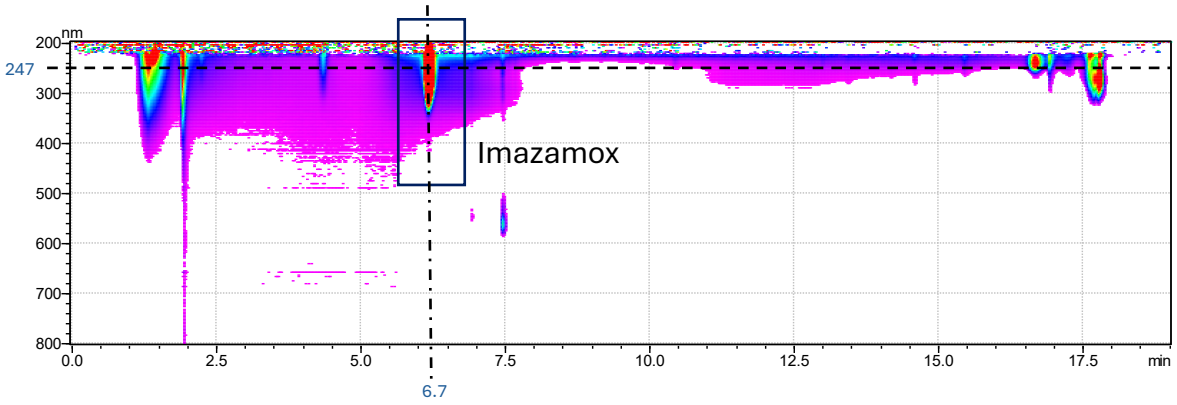


Figure 3.22: Intensity registered over time during the chromatogram run

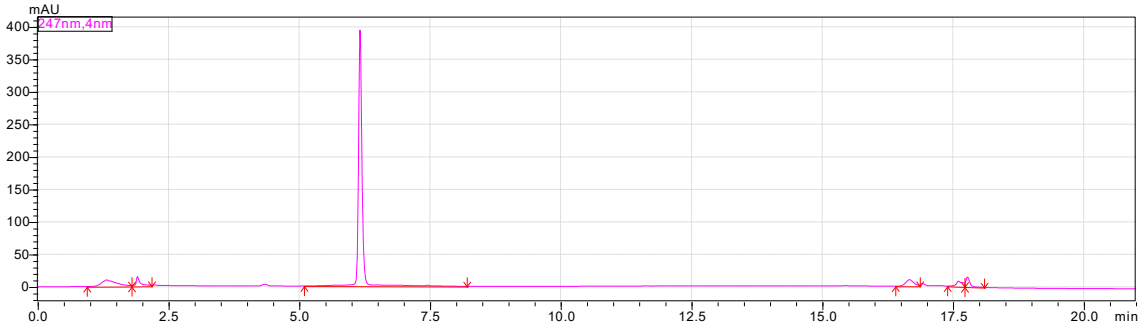


Figure 3.23: HPLC chromatogram at 247 nm

At the end of imazamox mobility test, the soil columns were allowed to drain for 24 hours to facilitate residual water content analysis following the procedure described in Section 3.5.1. The total imazamox eluted in each column effluent was calculated using the measurements of concentration and discharge volume; consequently, a mass balance analysis was carried out. To validate the mass balance calculation against experimental data, the soil cores were sectioned layer by layer at 1 cm increments, with its volume and wet mass recorded concurrently to reconstruct the vertical concentration profile. Retained imazamox was extracted from the soil samples using a 20 mmol.L^{-1} $CaCl_2$ solution. Initially, 35 ml of solution was added to each sample. This mixture was centrifuged and the supernatant was filtered, transferred to HPLC sampler vials and analysed for concentration. This extraction procedure was repeated twice more, namely, 22.5 ml and 15 ml were added in the second and third extractions, respectively

3.6 HYDRUS-1D Modelling

The numerical modelling using HYDRUS-1D was executed in three phases: Inverse modelling to estimate dispersivity α and saturated volumetric water content θ_s, forward modelling to plan imazamox transport experiments, and inverse modelling to determine soil distribution coefficient (K_D).

Saturated volumetric water content θ_s and dispersivity λ were evaluated from the tracer breakthrough curve by inverse modelling. Because the flow rate varied during column test, the initial flow rate was considered. Subsequently, the forward modelling of the Imazamox breakthrough curve was performed using the evaluated α and θ_S at previous modelling phase, and updated hydraulic conductivity corresponding to the final flowrates of the tracer test. This simulation was used to design the Imazamox transport experiment: determining the applied mass, the flushing start time after Imazamox application, flushing duration, sampling intervals, and the overall duration of the experiment. Following the physical column test, breakthrough curve was constructed from the measured effluent concentrations. Finally inverse numerical modelling was used to evaluate Kd [L^3M^{-1}], allowing the calculation of K_{oc} [L^3M^{-1}] of imazamox for comparison with literature values.

3.6.1 Determination of Soil Parameters

The van Genuchten model (Equation 8) is used to define hydraulic conductivity where water content (θ) is lower than saturated water content (θ) to represent the complete unsaturated flow phenomena in the model.

$$K(S_e) = K_{sat} S_e^{1/2} \left[1 - \left(1 - S_e^{\frac{1}{m}}\right)^m\right]^2 \qquad (8)$$

where $K(S_e)$ $[LT^{-1}]$ is the unsaturated hydraulic conductivity, K_{sat} $[LT^{-1}]$ is the saturated hydraulic conductivity, S_e [-] is the effective saturation, and m [-] is a dimensionless empirical shape parameter related to n [-] by m = 1 - 1/n (Van Genuchten, 1980). The effective saturation S_e is defined as:

$$S_e = \frac{\theta - \theta_r}{\theta_S - \theta_r} \qquad (28)$$

where θ [-] is the volumetric water content, θ_r [-] is the residual water content, and θ_s [-] is the saturated water content.

Thereby, with known dry bulk density of the soil matrix, total organic matter and particle size distribution, pedotransfer functions (Equation 29-34) were adapted to predict these parameters except θ_r. (Tosco, 2025; Wösten et al., 1999).

$$\theta_s = 0.7919 + 0.001691 \cdot C - 0.29619 \cdot D - 0.000001491 \cdot S^2 + 0.0000821 \cdot OM^2 + (0.02427 / C) + (0.01113 / S) + 0.01472 \cdot \ln(S) - 0.0000733 \cdot OM \cdot C - 0.000619 \cdot D \cdot C - 0.001183 \cdot D \cdot OM - 0.0001664 \cdot topsoil \cdot S \qquad \textbf{(29)}$$

$$\alpha = \exp[-14.96 + 0.03135 \cdot C + 0.0351 \cdot S + 0.646 \cdot OM + 15.29 \cdot D - 0.192 \cdot topsoil - 4.671 \cdot D^2 - 0.000781 \cdot C^2 - 0.00687 \cdot OM^2 + (0.0449 / OM) + 0.0663 \cdot \ln(S) + 0.1482 \cdot \ln(OM) - 0.04546 \cdot D \cdot S - 0.4852 \cdot D \cdot OM + 0.00673 \cdot topsoil \cdot C] \qquad \textbf{(30)}$$

$$n = 1 + \exp[-25.23 - 0.02195 \cdot C + 0.0074 \cdot S - 0.1940 \cdot OM + 45.5 \cdot D - 7.24 \cdot D^2 + 0.0003658 \cdot C^2 + 0.002885 \cdot OM^2 - (12.81 / D) - (0.1524 / S) - (0.01958 / OM) - 0.2876 \cdot \ln(S) - 0.0709 \cdot \ln(OM) - 44.6 \cdot \ln(D) - 0.02264 \cdot D \cdot C + 0.0896 \cdot D \cdot OM + 0.00718 \cdot topsoil \cdot C] \qquad \textbf{(31)}$$

$$Ks = \exp(7.755 + 0.0352 \cdot S + 0.93 \cdot topsoil - 0.967 \cdot D^2 - 0.000484 \cdot C^2 - 0.000322 \cdot S^2 + (0.001 / S) - (0.0748 / OM) - 0.643 \cdot \ln(S) - 0.01398 \cdot D \cdot C - 0.1673 \cdot D \cdot OM + 0.02986 \cdot topsoil \cdot C - 0.03305 \cdot topsoil \cdot S) \qquad \textbf{(32)}$$

$$l^* = 0.0202 + 0.0006193 \cdot C^2 - 0.001136 \cdot OM^2 - 0.2316 \cdot \ln(OM) - 0.03544 \cdot D \cdot C + 0.00283 \cdot D \cdot S + 0.0488 \cdot D \cdot OM \qquad \textbf{(33)}$$

$$l = 10 \cdot (\exp(l^*) - 1) / (\exp(l^*) + 1) \qquad \textbf{(34)}$$

where C is the clay percentage (< 2 µm), S is the silt percentage (2–50 µm), OM is the organic matter percentage (or TOC), D is the dry bulk density [g/cm^3], and topsoil is an indicator variable equal to 1 for topsoil and 0 for subsoils. The fine fraction was not analysed further to determine the clay percentage in this study; therefore, all particle sizes below 50 μm were classified as silt, and all terms including clay were omitted from pedotransfer equations.

However, due to the high uncertainty of K_s (coefficient of determination (R^2) of ln(K_S) = 0.19) and l (coefficient of determination (R^2) of ln(l*) = 0.12) reported by Wösten et al., 1999, the experimentally derived parameters were prioritized over the empirical estimates from these functions.

Moreover, the tortuosity parameter l in the conductivity function proposed by Mualem, (1976) was set to 0.5, as this value has been shown to be statistically optimal for most soil matrices. Additionally, the residual water content θ_r was defined based on initial water content found before the saturation phase.

The hydraulic conductivity K_s was calculated manually using Equation (35) which was derived from Equation (3):

$$q_s = K_s\left(\frac{H+L}{L}\right) \qquad (35)$$

where q_s, and K_s are the parameters defined for Equation 2, H [L] is the water head at the top of the column, L [L] is the length of the column and $\frac{H+L}{L}$ is the hydraulic gradient along the column.

As a result, only the α and n were derived by the pedotransfer functions. While K_S was determined by experimental measurements.

3.6.2 Theoretical Background of Solute Transport Modelling

This section explains the modelling framework sequentially for conservative tracer transport, non-conservative tracer transport, and the imazamox leaching simulation.

When the conservative tracer was injected into the soil matrix, the column was saturated; therefore, the volumetric water content across the column and over time is constant and equal to the saturated volumetric water content (θ_s). In addition, the flowrate was assumed to be steady. The effective velocity v [LT^{-1}] of fluid particles and conservative tracers-tracers which move with water at the same velocity- is defined as:

$$v = \frac{q}{\theta_s} \qquad (36)$$

where q is the Darcy velocity ($q = Q_S/A$, where Q_S is the volumetric discharge and A is the cross-sectional area of the column).

Considering Equations 6 and 7 :

$$\frac{\rho}{\theta}\frac{\partial S}{\partial t} + \frac{\partial C}{\partial t} = D_S\frac{\partial^2 C}{\partial z^2} - v\frac{\partial C}{\partial z} \qquad (6)$$

$$D_S = \alpha v + \tau D_0 \qquad (7)$$

The molecular diffusion term (τD_0) was considered negligible compared to mechanical dispersion in this study; hence the hydrodynamic dispersion coefficient was defined as $D_S = \alpha_L v$. Because conservative tracers are not adsorbed onto soil particle, $\frac{\partial S}{\partial t}$ was set to zero. Given the dispersivity α and saturated volumetric water content θ_s, the solute concentration C(t,z) can be mathematically determined, where t and z are time and the vertical coordinate, respectively. Initially, by assuming values for α and θ_S, $C(t,Z_B)$ was simulated, where z_B is the coordinate at the column bottom and t is withing the experimental period.

The simulated concentration error was evaluated by comparing simulated results with measured values, where the solute concentration at the bottom. This step was repeated across all observation times to evaluate the corresponding simulated concentrations. Then, based on the residual matrix, θ_S and α were iteratively adjusted in HYDRUS-1D until the residuals converged. Furthermore, at critical points, the residuals were weighted to better align the simulation with the respective measurements.

The evaluation method for non-conservative tracers is the same, exception for the inclusion of adsorption, as these compounds are adsorbed onto soil particles. The adsorbed solute concentration in the solid phase (S) is quantified assuming a linear isotherm (Equation 10). Therefore, $\frac{\partial S}{\partial t}$ in Equations (6) is expressed in terms of the soil distribution coefficient (K_d). Given the K_d, the retardation coefficient (R) and the solute velocity (v_S) can be quantified using Equation (10):

$$R = \frac{v_e}{v_s} = 1 + \frac{\rho_b}{\theta} K_d \qquad (10)$$

where θ is volumetric water content (equal to the saturated volumetric water content, $\theta = \theta_S$, for these saturated tests) and ρ_b is the dry soil bulk density.

The values of θ_S and α determined from the conservative tracer modelling are adopted for this subsequence evaluation; thereby v_e is also known. The only unknown is K_d, which is estimated using the same inverse procedure described for conservative tracers.

Modelling imazamox solute transport corresponds to unsaturated conditions. Since the hydraulic conductivity is defined by the van Genuchten model, Richards' equation is applied in an iterative calculation, updating the water content from initial conditions (initial water content all over the column = θ_r) over spatial coordinates and time. Applying the same transport principles discussed for non-conservative solute transport, the concentration variation at the bottom of the column can be simulated over time. Thereby, by calculating the residuals between measured and simulated effluent concentrations, an inverse model is run to evaluate the soil distribution coefficient (K_d).

3.6.3 Boundary Conditions

The water flow upper boundary condition for the tracer inverse model was set as a Variable Pressure Head (Equation 37), so that when the injection solution was changed from the tracer solution to deionized water, the hydraulic head and the concentration of the tracer could be set explicitly.

$$h(0,t) = h_0(t) \qquad (37)$$

where h(0,t) [L] is the water head at the top at time t, and $h_0(t)$ is the predefined water head at time t.

The lower boundary condition was always set to free drainage (Equation 38). The water flow upper boundary condition used for the imazamox breakthrough curve modelling was an Atmospheric Boundary Condition with a Surface Layer (Equation 39) to accurately represent applying imazamox on dry soil and then deionized water after a few hours by maintaining a ponded water layer on the surface.

$$\frac{\partial h}{\partial z} = 0 \tag{38}$$

$$\begin{cases} q(0,t) = p(t)\,, & if \quad d_s < d_{s,max} \\ h(0,t) = h_{s,max}, & if \quad d_s \geq d_{s,max} \end{cases} \tag{39}$$

where z [L] is the vertical coordinate, h is the pressure head, q(0,t) [LT^{-1}] is the Darcy flow at the top at time t, p(t) [LT^{-1}] is precipitation at time t, h(0,t) [L] is the water head at the top, d_s [L] is the ponded water layer at the top, $d_{s,max}$ [L] is the predefined maximum ponded water layer and $h_{s,max}$ [L] is the water head at $d_{s,max}$.

The Equilibrium Model was always used for the solute transport modelling with the same boundary conditions for all the simulations; which were the Concentration Flux Boundary Condition (Equation 40), and Zero Concentration Gradient (Equation 41) for the upper and lower boundary conditions, respectively. The linear isotherm was utilized to represent adsorption of non-conservative tracer onto the soil.

$$C(t, z = 0) = C_0 \tag{40}$$

$$\frac{\partial C}{\partial z} = 0 \tag{41}$$

3.7 Summary of Experimental Workflow and Site-Specific Activities.

All tests done in this study are summarized in Table 3.2 along with their location and unique identifier.

Table 3.2: Summary of experimental activities, test locations, and sample identifiers.

Activity & Reference Section	Location	Sample evaluated	Identifier
Constant-Head Single-Ring infiltration test (Section 3.3.1)	Mortara 2 Beinette 1	In situ In situ	IN-C-M2 IN-C-B1
Falling-Head Single-Ring infiltration test (Section 3.3.2)	Mortara 3^S Mortara 3^D Mortara 4^S Mortara 4^D Beinette 1 Beinette 2	In situ In situ In situ In situ In situ In situ	IN-F-M3S IN-F-M3D IN-F-M4S IN-F-M4D IN-F-B1 IN-F-B2
Dry bulk density and Initial Volumetric Water content (Section 3.5.1)	Laboratory	All undisturbed core samples	DD, θ_i-All
Total organic carbon (Section 3.5.2)	Laboratory	All disturbed soil samples	TOC-All
Granulometric analysis (Section 3.5.3)	Laboratory	All disturbed soil samples	PS-All
KBr tracer calibration (Section 3.5.4)	Laboratory	N/A	Cal-KB
Fluorescein tracer evaluation (Section 3.5.5)	Laboratory	N/A	Cal-Fl
Rhodamine tracer evaluation (Section 3.5.5)	Laboratory	N/A	Cal-Rh
Agglomeration analysis (Section 3.5.6)	Laboratory	U-M2A	AG-DLS
Soil column saturation	Laboratory	U-M1A U-M2A U-M3S U-M3D	Sat-M1A Sat-M2A Sat-M3S ST-M3D

KBr tracer test (Section 3.5.9)	Laboratory	U-M1A U-M2A U-M3S U-M3D	KBr-M1A KBr-M2A KBr-M3S KBr-M3D
Rhodamine tracer test (Section 3.5.9)	Laboratory	U-M3S U-M3D	Rh-M3S Rh-M3D
Imazamox calibration (Section 3.5.10)	Laboratory	N/A	Cal-Im
Imazamox transport experiment (Section 3.5.10)	Laboratory	U-M3S U-M3D	Im-M3S Im-M3D
HYDRUS modelling for KBr tracer test (Section 3.5.12)	Laboratory	U-M3S U-M3S	HY-KBr-M3S HY-KBr-M3D
HYDRUS modelling for Rhodamine tracer test (Section 3.5.12)	Laboratory	U-M3S U-M3S	HY-Rh-M3S HY-Rh-M3D
HYDRUS modelling for Imazamox leaching test (Section 3.5.12)	Laboratory	U-M3S U-M3S	HY-Im-M3S HY-Im-M3D

Note: *Superscripts **S** and **D** denote shallow (at ground) and deep (at 20 cm depth) testing depths, respectively.*

The test specific conditions of infiltration tests including water head condition, duration, ring diameter and water head are presented in Table 3.3.

Table 3.3: Summery of field infiltration tests with experimental conditions

Test Identifier	Water head condition	Ring Diameter (cm)	Const. water head or Initial water head (cm)	Duration (min)
IN-C-M2	Constant	30	4.7	36
IN-C-B1	Constant	30	9.0	22.2
IN-F-M3S	Falling	25	32.0	138.0
IN-F-M3D	Falling	25	29.5	136.5
IN-F-M4S	Falling	25	33.1	65.5
IN-F-M3D	Falling	25	29.7	136.5
IN-F-B1	Falling	25	14.1	12.9
IN-F-B1	Falling	25	42.9	135

In total, four column tests were performed in this study. Two of them were used for preliminary studies using U-M1A and U-M2A cores, while the remaining two column tests were performed in parallel for primary study using two cores of U-M3S and U-M3D, collected from the same location (Location 3 at Mortara) at two different depths, representing a continuous soil profile (0-38 cm). The timeline, starting from saturation of each column, and experimental steps are illustrated in Figure 3.24. In addition, Table 3.4 summarizes the cumulative timing of each activity.

Table 3.4: Cumulative timeline for experimental activities in soil column tests. Time starts at the beginning of saturation phase and extends until the tracer start.

Sample evaluated	Time (Hours)					
	Tracer Start	Tracer Flush	Drainage Start	Imazamox App.	Imazamox Flush	Completion
U-M1A	15.40	38.68	46.65	N/A	N/A	N/A
U-M2A	16.18	140.18	379.68	N/A	N/A	N/A
U-M3S	1.75	59.77	202.32	220.32	237.05	390.22
U-M3D	1.47	26.55	55.63	73.63	92.47	144.42

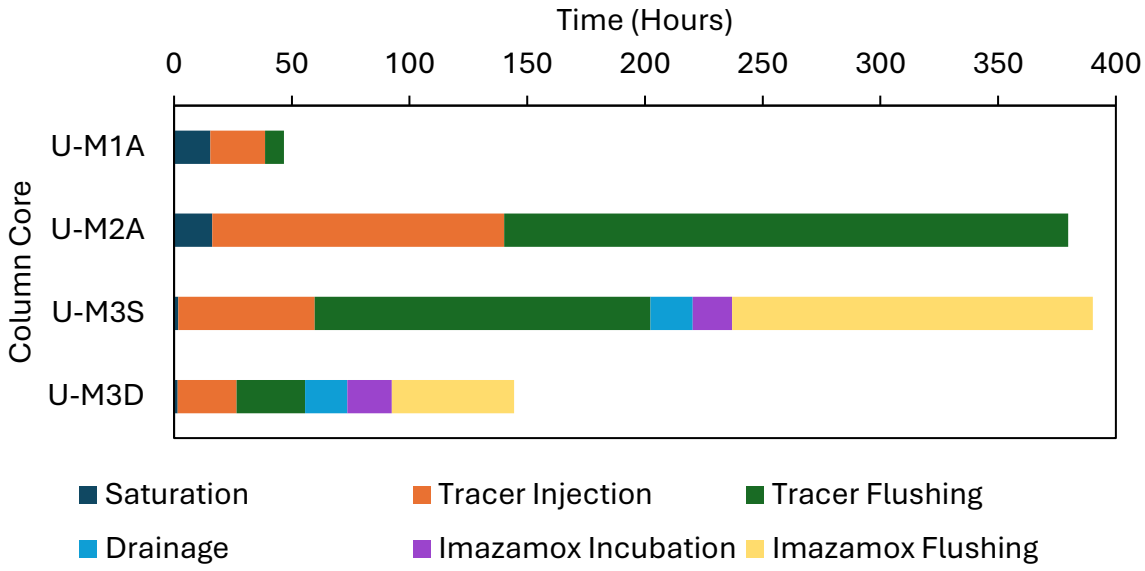


Figure 3.24: Timeline of experimental phases for each column test.

The preliminary column tests conducted on U-M1A and U-M2A cores consisted only of saturation and tracer test phases, where only the KBr tracer was applied. In contrast, the primary column tests using the U-M3S and U-M3D cores additionally included Rhodamine in the tracer test and a subsequent imazamox leaching test. The amount of applied imazamox application was determined through HYDRUS-1D forward simulations, aiming for precisely detectable concentrations while maintaining a reasonable flushing duration. The entire experimental procedure of this study, including both field and laboratory experiments, their connections, and their integration into the Ag-MAR modelling framework is illustrated in Figure 3.25.

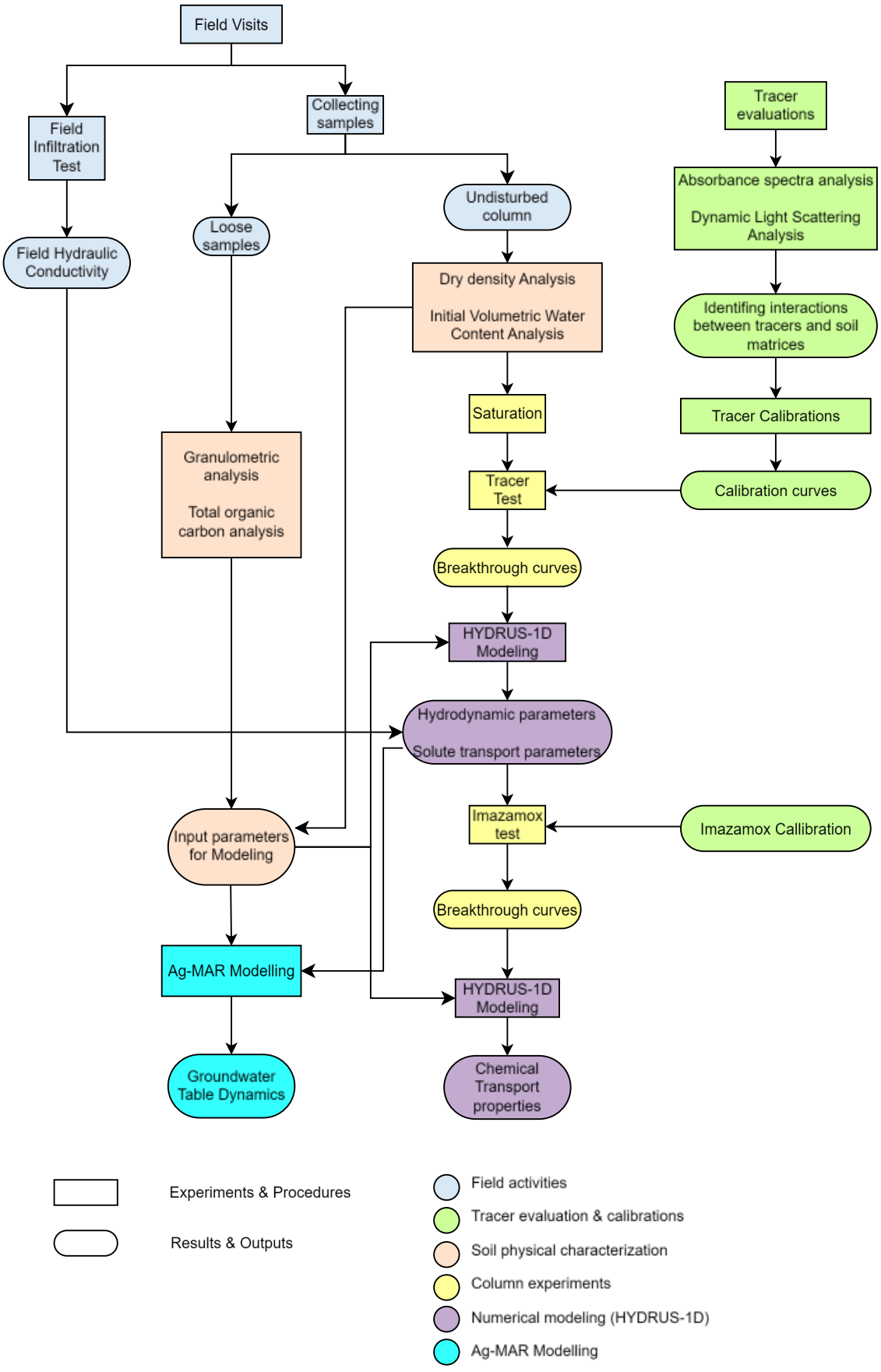


Figure 3.25: Flow chart of the study

4 Results and Discussion

4.1 Field Infiltration Experiments

4.1.1 Constant-Head Infiltration Tests

The constant-head infiltration setup equipped with a Mariotte reservoir presented handling and transport difficulties due to its heavy weigh, especially at agricultural field conditions where lacked access and manual carrying was necessary over uneven terrain. Additionally, using a larger diameter ring (30 cm) compared to that of the reservoir (Diameter- 24 cm) is not suitable for highly permeable soil as water cannot be refilled while maintaining a constant ponded head, and the total volume of water in the reservoir was insufficient for an adequate measurement period. Furthermore, the ponded water layer maintaining the constant head had to be established before recording measurements; meanwhile, water already infiltrated into the soil during filling. Consequently, cumulative infiltration prior to establishing the constant ponded layer was considerably high (Table 4.1), preventing accurate data acquisition during the transient phase due to this initial infiltration under a variable water head, especially in such permeable soils.

Table 4.1: Cumulative infiltration before establishing a constant ponded water head during constant-head infiltration tests.

Test	Initial infiltration (mm)
IN-C-M2	17.2
IN-C-B1	37.5

Constant-head infiltration tests (IN-C-M2 and IN-C-B1) were evaluated considering both transient and steady-state infiltration conditions. The method proposed by Odell et al., (1998) was utilized to evaluate the results in the transient regime; therefore, cumulative infiltration was plotted against the square root of time (Figure 4.1). The IN-C-M2 test results show a linear trend as suggested by the model, whereas the IN-C-B1 test results did not, revealing that transient condition was missed, particularly given the 37.5 mm initial infiltration (Table 4.1). Because of that, IN-C-B1 was not evaluated under transient conditions, while IN-C-M2 was evaluated without taking the initial outlier into account.

These outliers might have occurred due to preferential flow paths typical of agricultural soils. Table 4.2 summarizes the results.

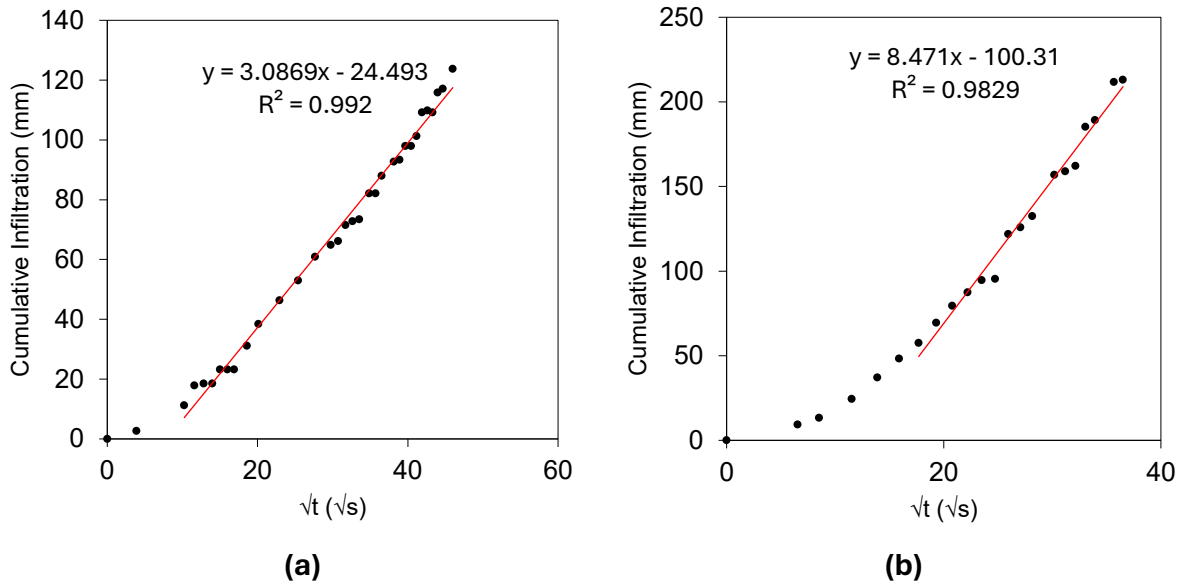


*Figure 4.1: Cumulative infiltration (I) plotted against the square root of time (√t) for the constant-head infiltration tests: (**a**) IN-C-M2 and (**b**) IN-C-B1*

To evaluate field saturated hydraulic conductivity (K_{fs}) considering the steady flow regime using the procedure described in Section 3.3.1.1, cumulative infiltration (I) was plotted against time (t), as showed in Figure 4.2. IN-C-M2 test entered the steady flow regime after 500 s, while IN-C-B1 exhibited steady flow from the beginning. The final results were summarized in Table 4.2.

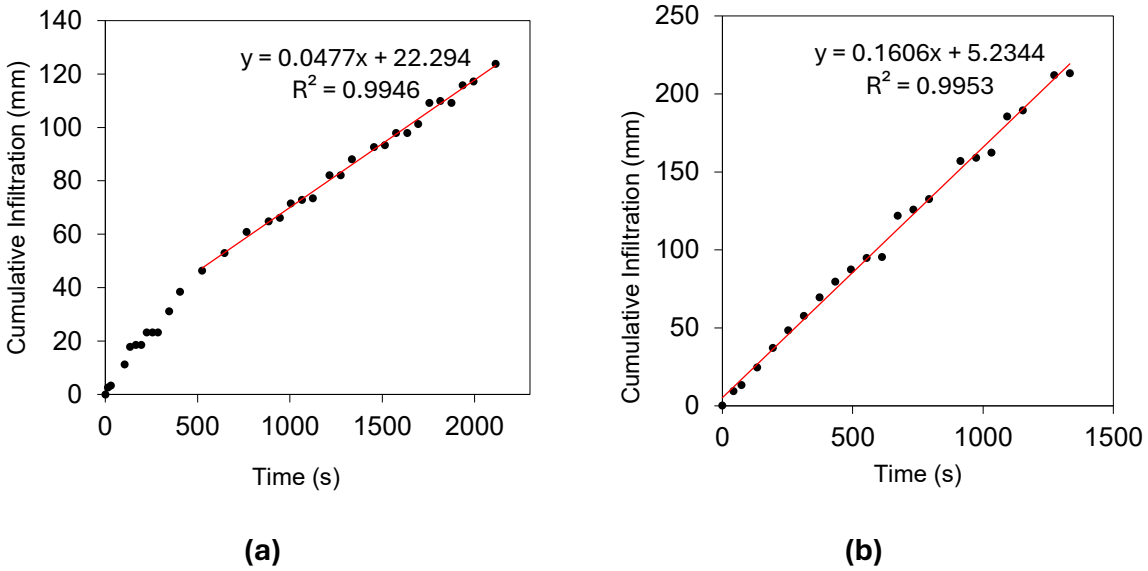


*Figure 4.2: Cumulative infiltration (I) plotted against time (t) for the constant-head infiltration tests: (**a**) IN-C-M2 and (**b**) IN-C-B1*

Table 4.2: Summary of constant-head single ring infiltration tests.

Test	Flow regime	K_{fs} ($\times 10^{-6}$ ms^{-1})
IN-C-M2	Transient	269.3
	Steady	31.5
IN-C-B1	Steady	72.0

The IN-C-M2 test results showed significantly different values depending on the evaluated flow regime: steady-state and transient. However, the result obtained under the steady-state regime was considered more reliable because substantial infiltration occurred prior to establishing a stable ponded water layer. For future studies, it is suggested to prioritize steady-state flow regime readings for highly permeable sandy soils. Nevertheless, the primary challenge in achieving a steady-state flow regime is the substantial water volume needed before reaching it. A related operational limitation is that the Mariotte reservoir of the constant-head setup cannot be refilled while simultaneously maintaining a constant ponded water head inside the ring. As an alternative, transient flow regime measurements could be adopted with one practical modification: reducing the ponding depth. This reduces both the time needed to establish the target water head and the cumulative infiltration that occurs beforehand. However, further experimental work should be carried out to validate these findings.

4.1.2 Falling Head Infiltration Tests

The single-ring, falling-head infiltration test was logistically simpler because the setup required only data loggers, a ring, and a measuring tape. However, pouring water into the ring disturbed the topsoil. However, due to automated data logging, multiple falling-head tests could be conducted simultaneously without direct supervision while the tests were running.

The falling head infiltration data evaluation methodology proposed by Nimmo et al., (2009) was utilised for falling head results. A few initial readings of a few tests are not aligned with the relationship of Equation 12 (Figure 4.4). The saturated hydraulic conductivity results of the falling head tests are summarised in Table 4.3.

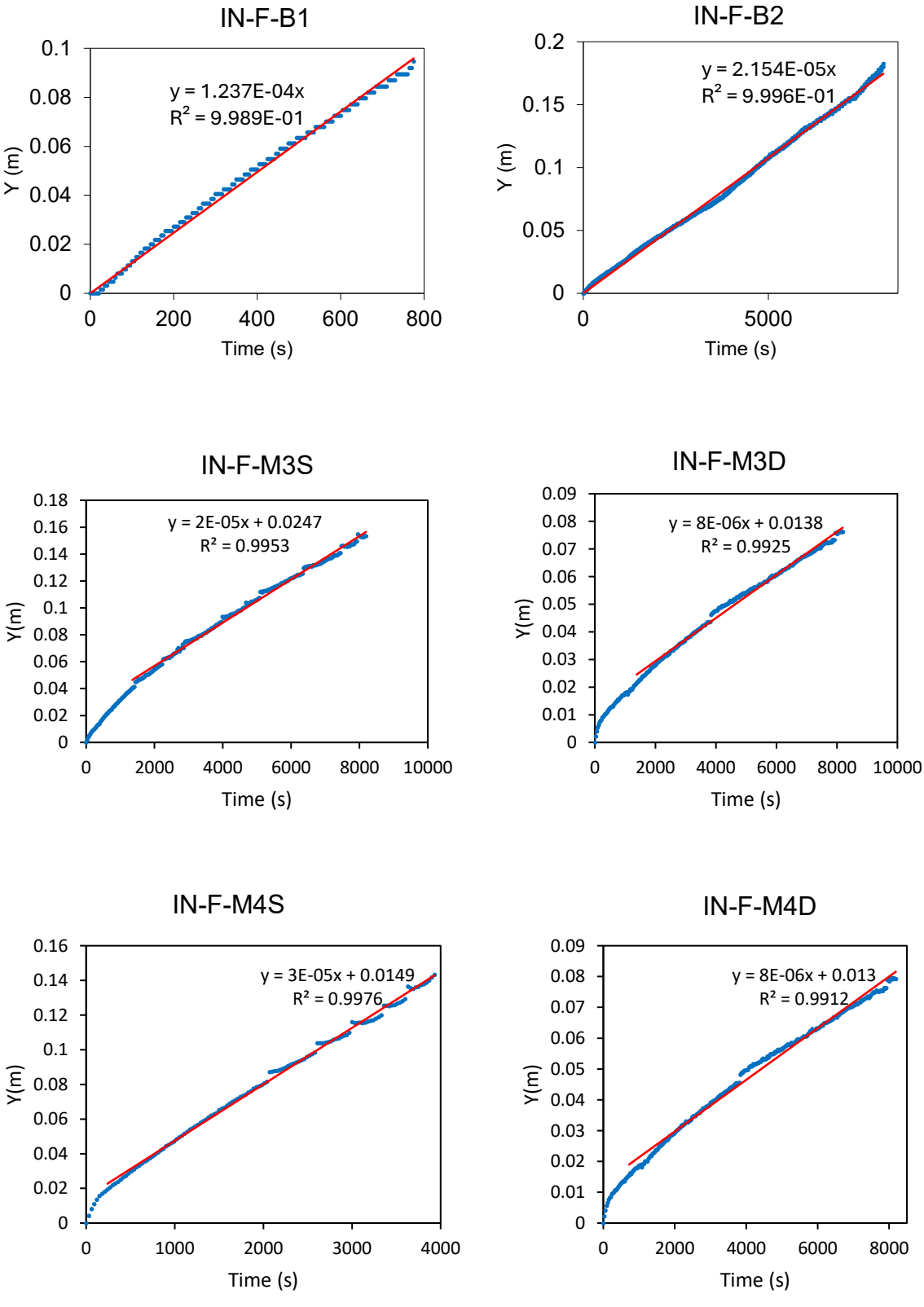


Figure 4.3: Linearization variable Y (left-hand side of Equation 13) plotted against time for the falling-head infiltration tests.

.

Table 4.3: Summary of falling-head single-ring infiltration test results.

Tests	K_{fs} ($\times 10^{-6}$ m/s)
IN-F-B1	124
IN-F-B2	21.5
IN-F-M3S	16.1
IN-F-M3D	7.8
IN-F-M4S	16.5
IN-F-M4D	8.4

Considering the Beinette Location 1 constant-head (Table 4.2; IN-C-B1; K_{fs}= 72 $\times 10^{-6}$ ms^{-1}) and falling-head (Table 4.3; IN-F-B1; K_{fs} = 124 $\times 10^{-6}$ ms^{-1}) results, the K_{fs} obtained by the falling-head test is 1.7 times of the constant-head infiltration test. Given the inherent spatial variability of agricultural soils, even between two tests conducted directly adjacent to each other, this level of agreement is satisfactory, implying that falling-head tests and constant-head single-ring infiltration tests under steady-state conditions are practically interchangeable and yield comparable results in highly permeable sandy soils.

4.2 Soil Characterization

4.2.1 Granulometric Analysis

All the soil samples contained more than 96% sand. Due to this high sand content, the soil is classified strictly as sand regardless of the individual percentages of silt and clay (Figure 4.4). The sand percentage of each soil sample is detailed in Table 4.4.

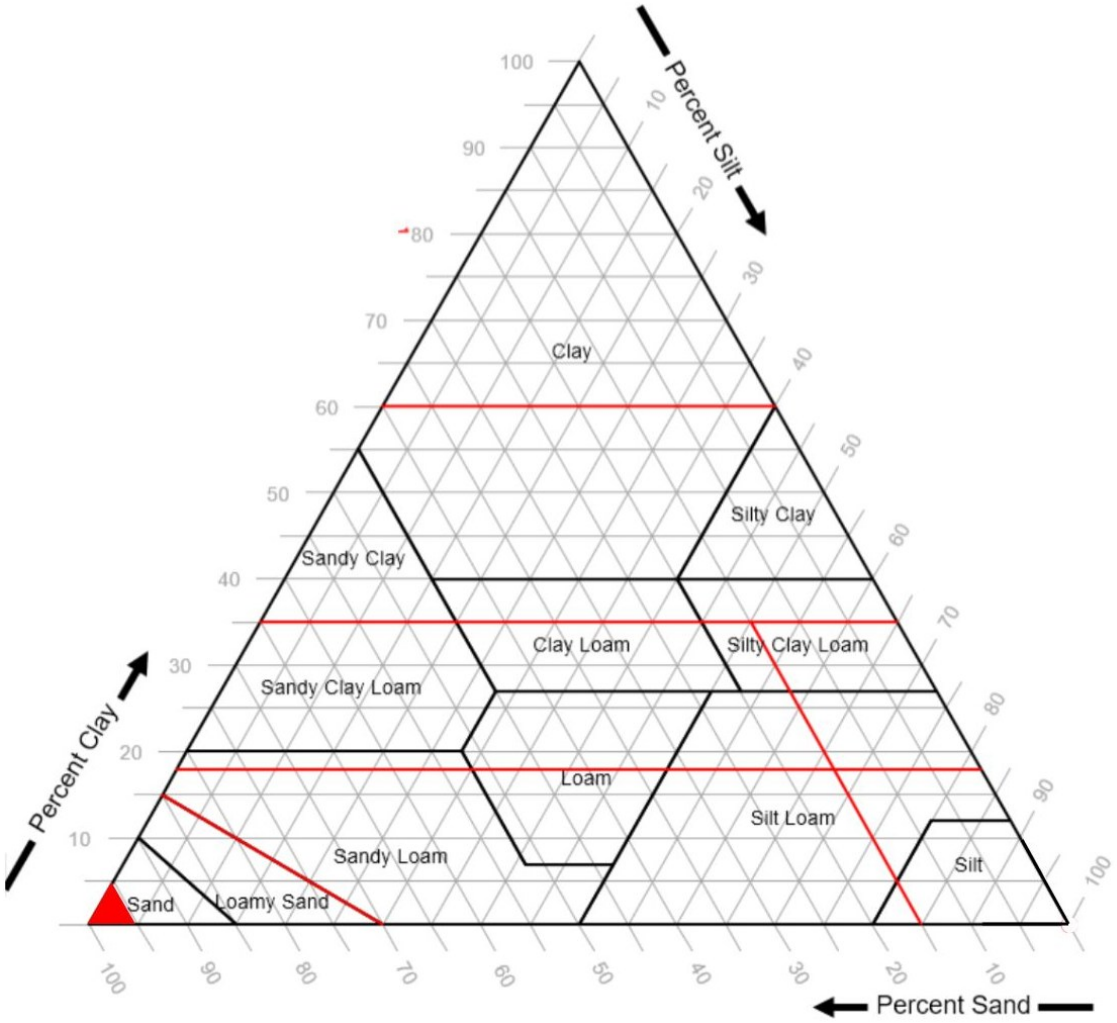


Figure 4.4: USDA soil texture triangle (Van Lear, 2024). The red highlighted area indicates the domain containing all analysed samples.

Table 4.4: Percentage of particle fractions and USDA soil category

		Mortara 1	Mortara 2	Mortara 3 Shallow	Mortara 3 Deep	Mortara 4 Shallow	Mortara 4 Deep	Beinette
%	Gravel	0.29	0.09	0.230428	0	0.50	0.14	0
	Sand	96.66	96.20	97.16	98.77	97.08	97.60	98.87
	Silt and clay	3.04	3.71	2.61	1.23	2.42	2.26	1.13
Soil Category		**Sand**	**Sand**	**Sand**	**Sand**	**Sand**	**Sand**	**Sand**

4.2.2 Dry Density and Initial Water Content

The undisturbed core soil samples were used for dry bulk density and Volumetric Water Content (VWC) analysis. Initial water content represents the water content when the soil was sampled. The measured values for all the seven soil samples were summarized in Table 4.5.

Table 4.5: Dry bulk density and initial Volumetric Water Content (VWC)

Soil sample	Dry bulk density (g/cm^3)	Initial VWC (%)
U-M1A, U-M1B	1.75[a]	0.35[a]
U-M2A	1.54	0.32
U-M3S	1.56	0.24
U-M3D	1.45	0.06
U-M4S	1.72	0.22
U-M4D	1.65	0.09

Note: [a]Values represent the average of samples U-M1A and U-M1B.

Samples U-M3S, U-M3D, U-M4S and U-M4D were collected on the same day; therefore, the comparison is limited to these samples. The variation in dry bulk density and VWC at the same depth (Shallow - U-M3S and U-M4S, Deep- U-M3D and U-M4D) was relatively small. However, both the dry bulk density and VWC of the shallow soil are higher at both locations 3 and 4 in Mortara.

4.2.3 Total Organic Carbon

Total Carbon (TC) and Inorganic Carbon (IC) were evaluated separately, from which Total Organic Carbon (TOC) was calculated. The results are summarized in Table 4.6.

Table 4.6: Total Organic Carbon (TOC) of soil samples

Sample	TC (%)	IC (%)	TOC (%)
D-M1	1.76	0.03	1.73
D-M2	1.78	0.04	1.74
D-M3S	1.67	0.04	1.63
D-M3D	0.86	0.04	0.82
D-M4S	1.12	0.04	1.08
D-M4D	0.76	0.04	0.72
D-B1	0.79	0.04	0.76

As expected in agricultural lands, TOC values of deep soil samples from Mortara locations 3 and 4 were lower than those observed in shallow soil samples.

4.2.4 Estimation of Soil Hydraulic Parameters via Pedotransfer Functions

The soil hydraulic parameters of the van Genuchten model-estimated using the pedotransfer functions described in Section 3.6.1-namely the saturated hydraulic conductivity Ks, saturated volumetric water content θs, empirical shape parameters n and α, and the pore-connectivity parameter l, were determined from the measured values of TOC, dry bulk density, particle size distribution, and the respective soil layer designation. The resulting values are summarized in Table 4.7.

Table 4.7: Estimated van Genuchten soil hydraulic parameters obtained from pedotransfer functions.

Location	Depth (cm)	K_S ($\times 10^{-6}$ ms^{-1})	θ_s (%)	l [-]	n [-]	α (cm^{-1})
Mortara 1	0-18	11.61	29.59	0.82	1.022124	0.143175519
Mortara 2	0-21	18.26	34.56	0.92	1.025178	0.130401095
Mortara 3	0-20	22.01	34.19	0.66	1.024756	0.142212187
Mortara 3	20-38	24.19	37.68	-0.21	1.026902	0.119857404
Mortara 4	0-23.5	15.22	29.04	0.43	1.022043	0.101326299
Mortara 4	23.5-45.5	9.18	30.65	0.07	1.023297	0.102116345
Beinette 1	0-20	33.53	31.92	-0.07	1.02314	0.118093373

4.3 Tracer Selection and Validation

4.3.1 KBr Calibration

The background Electrical Conductivity (EC) of effluent directly impacted the calibration curve as the concentration of KBr was measured based on EC, and the EC of the effluent was changed over time. Table 4.8 summarises the EC of effluent at the start of the tracer test. For this reason, the calibration curve (Figure 4.5) was prepared by diluting KBr in the effluent from U-M2A core and using Equation (26) to determine the net electrical conductivity (ΔEC) contributed by KBr alone, which was then plotted against the KBr concentration.

Table 4.8: Electrical Conductivity of Effluent

Column	EC ($\mu S/cm$)
Mortara 1	57
Mortara 2	151
Mortara 3 Shallow	70
Mortara 3 Deep	63

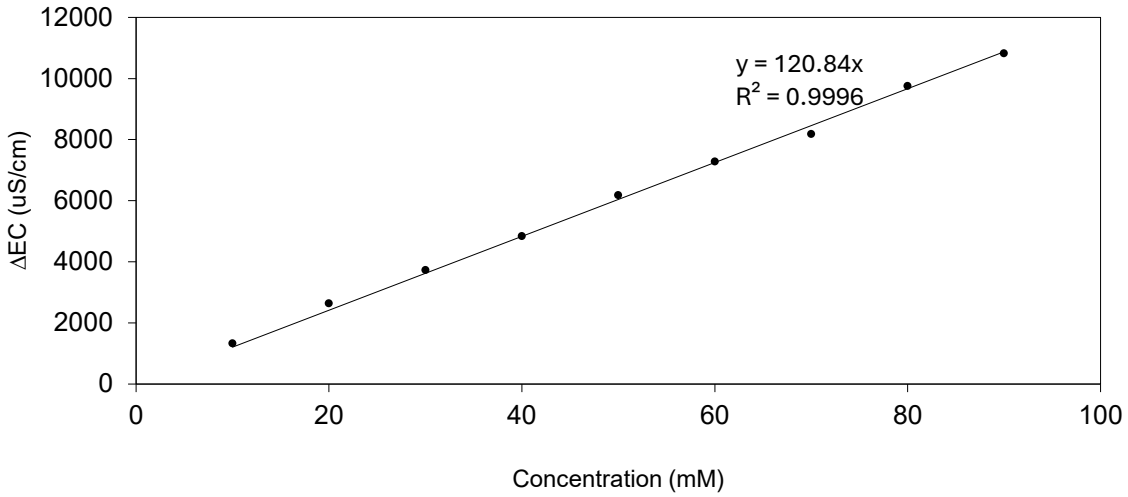


Figure 4.5: Calibration curve of KBr: net electrical conductivity ($\Delta EC = EC_{ef} - EC_{sat}$) plotted against concentration where EC_{ef} is the electrical conductivity of standard samples diluted in effluent and EC_{sat} is the soil-specific background electrical conductivity.

4.3.2 Fluorescein and Rhodamine Compatibility

Varying absorbance values around a wavelength of 488.5 nm were observed for the same fluorescein concentration in different background solutions. Furthermore, the peak absorbance wavelength (λ_{max}) also changed depending on the background solution, namely effluent, KBr, and Rhodamine. Consequently, normalized absorbance was illustrated as shown in Figure 4.6. The absorbance of rhodamine was also normalized as illustrated in Figure 4.7. The maximum absorbance wavelength (λ_{max} = 565.5 nm) and its corresponding value were consistent across different background solutions.

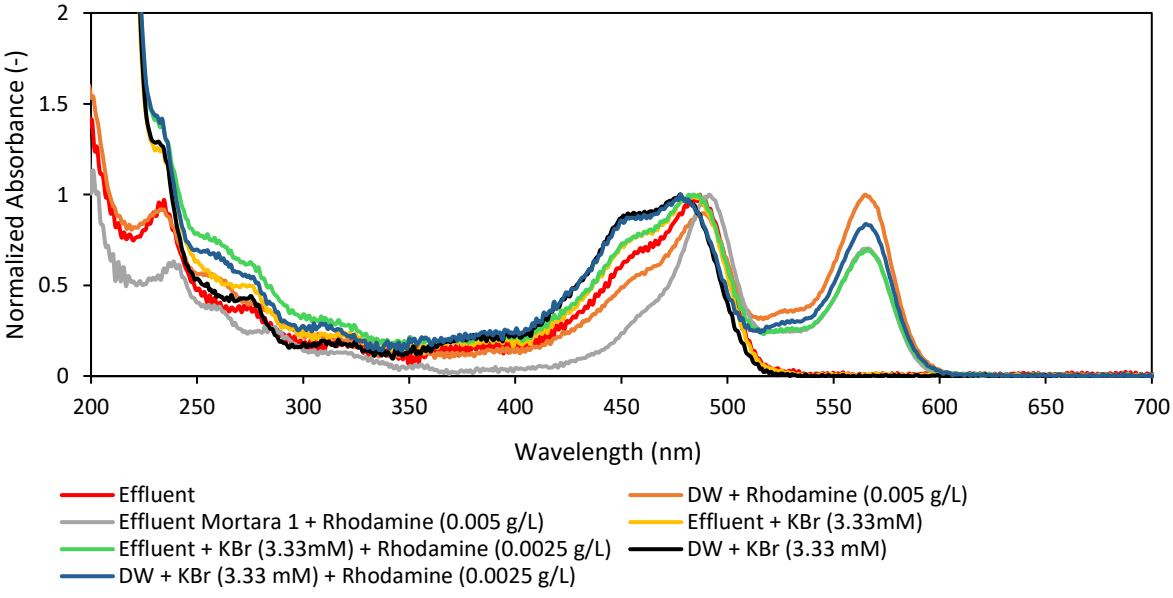


Figure 4.6: Normalized absorbances of fluorescein at a concentration of 0.0025 g/L in different solutions.

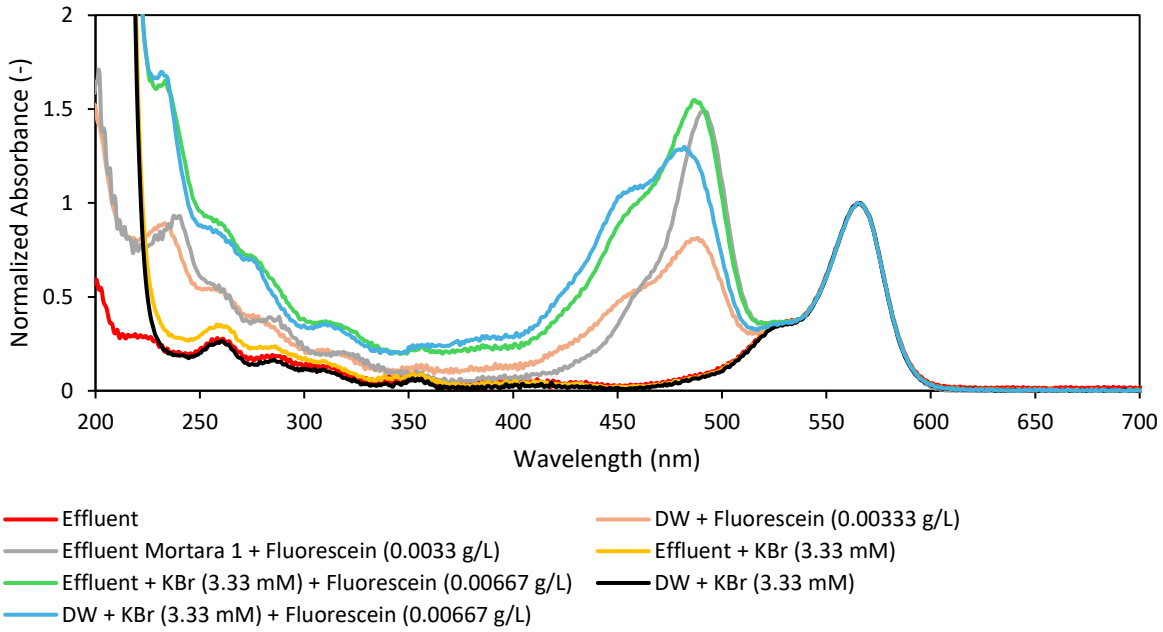


Figure 4.7: Normalized absorbances of rhodamine at a concentration of 0.00667 g/L in different solutions

Due to its spectral instability across different matrix solutions, fluoresceine could not be used as a tracer, as a reliable calibration curve could not be generated. Conversely, rhodamine absorbance at the peak at wavelength higher than 550 nm was found well reproducible across Deionized Water (DW), Effluent and KBr solutions. Consequently, rhodamine and KBr were chosen to be used as tracers simultaneously in the same tracer test. The calibration curve for rhodamine used illustrates in Figure 4.8.

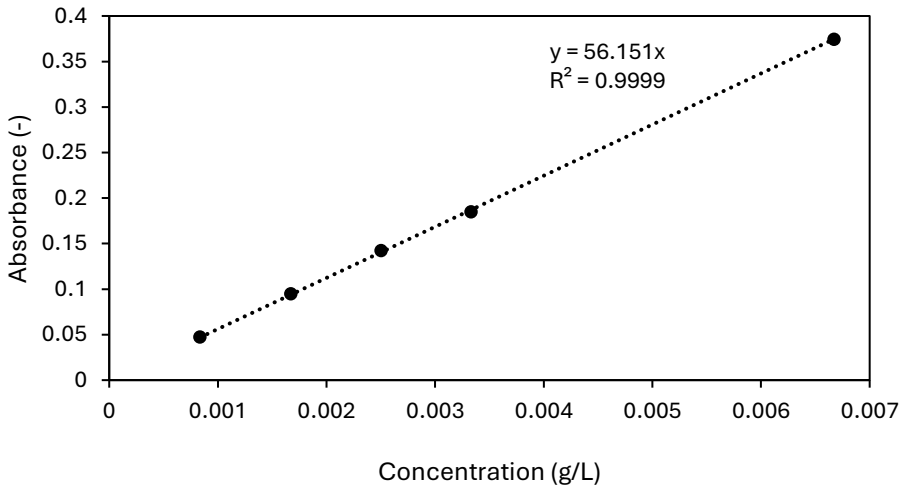


Figure 4.8: Calibration curve of Rhodamine in KBr background solution measured at a wavelength of λ = 565.5 nm

4.3.3 Agglomeration Tests

The three replicate measurements taken for one reading had high variability. The measurement average of PDI and Z-average were not reproducible. However, the count rate yielded acceptable and reproducible results. These results were normalized to compensate for differences in initial count rates at the baseline reading (t = 5 h) and are illustrated in Figure 4.9.

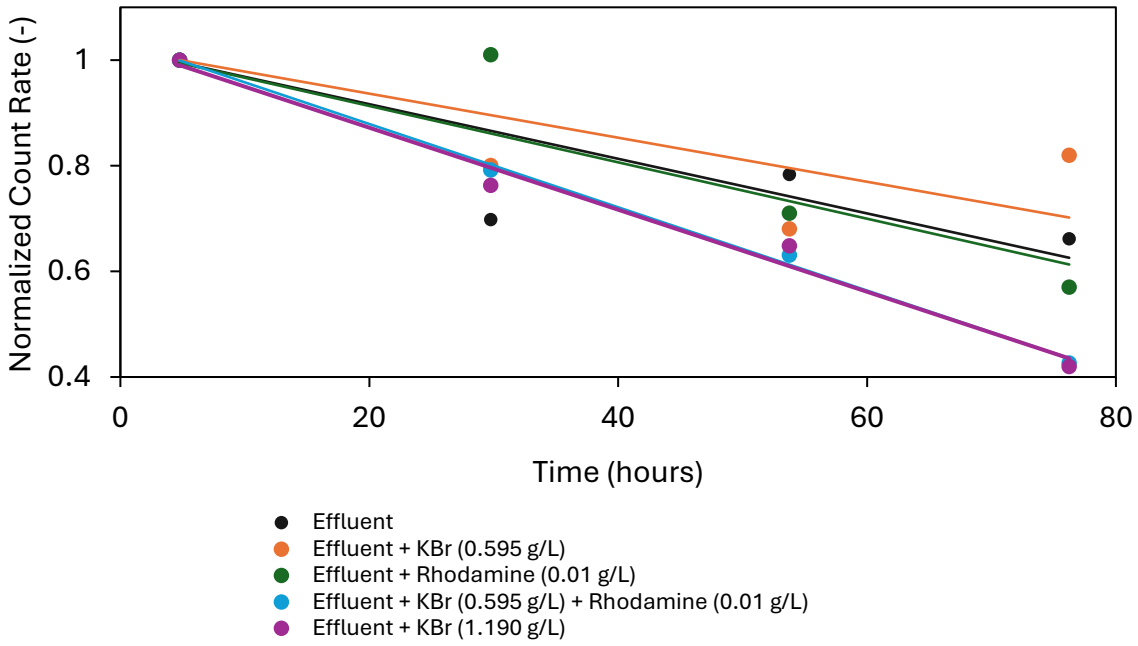


Figure 4.9: Variation in normalized count rate over time for different solutions. Fitted linear trendlines, forced to start from 1 at the baseline reading, are shown for each condition, with values normalized to the baseline reading at t=5 h.

A decrease of normalized count rate indicates that sedimentation occurred during measurements taken on subsequent days. The solution with 0.595 $g.L^{-1}$ (5 $mmol.L^{-1}$) KBr and Rhodamine showed the same declining trend as the the solution with 1.190 $g.L^{-1}$ (10 mM) KBr. Nevertheless, the slope of effluent alone was steeper than that of the solution with 0.595 $g.L^{-1}$ (5 $mmol.L^{-1}$) KBr. Due to these contradictions, no clear agglomeration trend related to KBr could be identified. Moreover, the solution with Rhodamine had near the same slope as effluent alone. In conclusion, withing the tested concentration range (Rhodamine: 0 – 0.01 $g.L^{-1}$; KBr: 0 – 1.190 $g.L^{-1}$), agglomeration of the fine soil particle fraction was not affected by KBr or Rhodamine, indicating that both tracers are safe to use in column tests within this range.

4.4 Laboratory Column Tests

The column experiments mainly consisted of three phases: saturation, the tracer test (tracer injection and flushing), and the imazamox leaching test. This section presents the results of each test. The overall behaviour of the primary column experiments, performed using two columns (U-M3S and U-M3D), is illustrated in Figure 4.10 and Figure 4.11. Under a constant water head of 3.5 cm at the top of both columns, the outflow rate continuously decreased until the end of the tracer elution. The discharge rate of U-M3S slightly increased toward the end of the imazamox leaching test without any external intervention. In contrast, the discharge rate of U-M3D during the imazamox leaching test fluctuated continuously due to organic matter agglomeration in the outflow pipe and its subsequent cleaning. The flow rate at each stage, saturated hydraulic conductivity, timestamps, concentrations of injected solutions, and maintained water head are summarized in Table 4.9 and Table 4.10. A detailed analysis and discussion of the breakthrough behaviour and solute transport parameters for each individual phase are presented in the following subsections.

Table 4.9: Experimental timeline, hydraulic boundary conditions, and solution parameters across all operational phases for column U-M3S

Phase	Test ID	Water head (cm)	Time interval (h)	Average Outflow rate (g/h)	K_S ($\times 10^{-6}$ ms^{-1})	Compound	Concentration (g/L)
Saturation	Sat-M3S	3.5	0-1.74	43.09	6.30	DW	-
Tracer Injection	KBr-M3S Rh-M3S	3.5	1.74-59.76	40.09	5.86	KBr Rhodamine	1.19 0.016
Tracer flushing	KBr-M3S Rh-M3S	3.5	59.76-202.31	-	-	-	-
Gravity Drainage	-	-	202.31-220.31	-	-	-	-
Imazamox Application	Im-M3S	-	220.31	-	-	Imazamox	0.04 g[a]
Incubation of Imazamox	IM-M3S	-	220.31-237.04	-	-	-	-
Imazamox flushing	Im-M3S	3.5	237.04-390.21	9.14	0.13	DW	-

Note. DW =deionized water

[a]Applied as a 20 ml pulse of a 2.0 g/L solution (Total mass:0.04 g)

Table 4.10: Experimental timeline, hydraulic boundary conditions, and solution parameters across all operational phases for column U-M3D.

Phase	Test ID	Water head (cm)	Time interval (h)	Average Outflow rate (g/h)	K_S ($\times 10^{-6}$ ms^{-1})	Compound	Concentration (g/L)
Saturation	Sat-M3D	3.5	0-1.47	76.57	11.20	DW	-
Tracer Injection	KBr-M3D Rh-M3D	3.5	1.47-26.55	64.15	9.14	KBr Rhodamine	1.19 0.016
Tracer flushing	KBr-M3D Rh-M3D	3.5	26.55-55.63	-	-	-	-
Gravity Drainage	-	-	55.63-73.63	-	-	-	-
Imazamox Application	Im-M3D	-	73.63	-	-	Imazamox	0.04 g[a]
Incubation of Imazamox	IM-M3D	-	73.63-92.47	-	-	-	-
Imazamox flushing	Im-M3D	3.5	92.47-144.42	22.27	0.32	DW	-

[a]*Applied as a 20 ml pulse of a 2.0 g/L solution (Total mass:0.04 g)*

Note. DW = deionized water

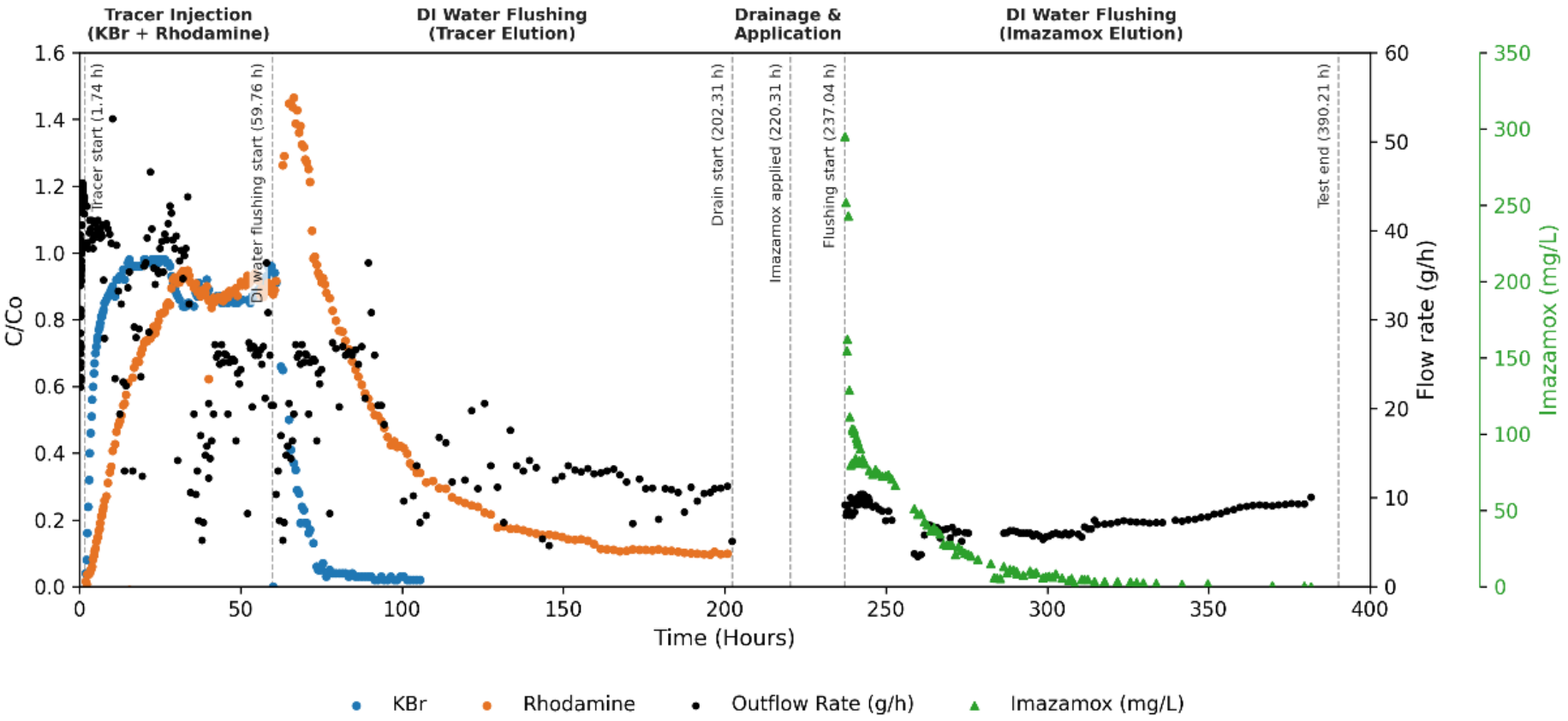


Figure 4.10: Complete breakthrough curves and effluent discharge dynamics during column experiment for U-M3S core. Left axis: normalized relative concentration (C/C_0); inner right axis: column effluent flow rate (g/h); outer right axis: Imazamox effluent concentration (mg/L).

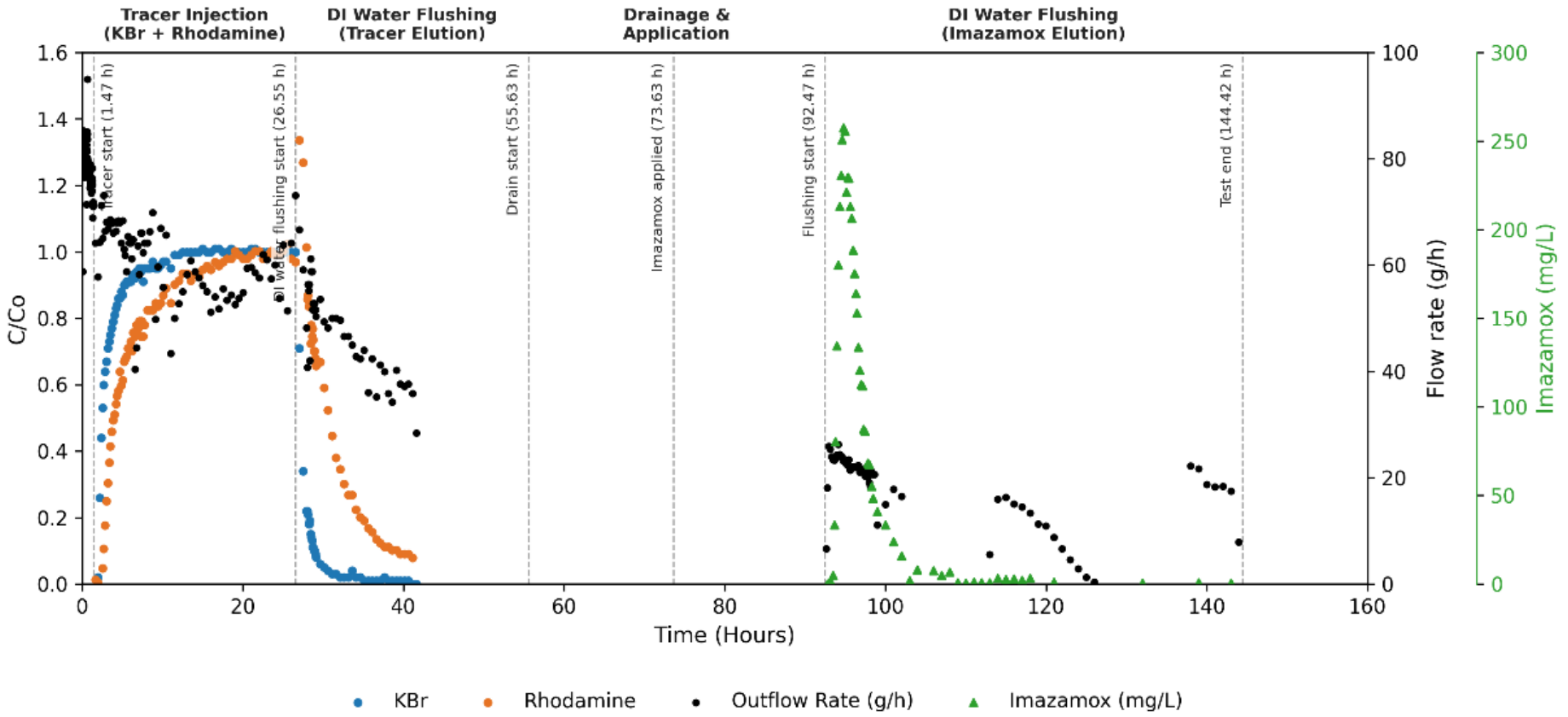


Figure 4.11: Complete breakthrough curves and effluent discharge dynamics during column experiment for U-M3D core. Left axis: normalized relative concentration (C/C_0); inner right axis: column effluent flow rate (g/h); outer right axis: Imazamox effluent concentration (mg/L).

4.4.1 Column Saturation and Tracer Tests

4.4.1.1 Saturation phase

The saturated hydraulic conductivity (K_s) was determined during the saturation phase using Equation (35):

$$q_s = K_s\left(\frac{H+L}{L}\right) \qquad (35)$$

where q_s, and K_s are the parameters defined for Equation (3), H [L] is the water head at the top of the column, L [L] is the length of the column. Steady state discharge Q_s [LT^{-1}] was obtained by the mass measurement of effluent over time. Consequently, q_s was determine by $q_s = Q_s/A$, where A is the cross- section area of the column. The saturated water content measured during saturation phase is summarized in Table 4.11:

Table 4.11: Hydraulic conductivity at the saturation phase

Test	Core sample	Flow rate ($\times 10^{-9}$ m^3/s)	Water head at the top ($\times 10^{-2}$ m)	K_s ($\times 10^{-6}$m/s)
Sat-M1A	U-M1A	2.68	5.5	1.3
Sat-M2A	U-M2A	1.09	5.5	0.5
Sat-M3S[a]	U-M3S	42.96	3.5	23.7
Sat-M3D[a]	U-M3D	59.73	3.5	30.6

[a]columns that underwent an initial separate saturation test; the reported data correspond to these dedicated tests for direct comparison with field data. A distinct saturation phase was conducted for the continuous column tests followed by the tracer tests, but those values are not reported here; instead, values reported in Table 4.9 and Table 4.10.

Soil cores from Mortara 1 and Mortara 2 were collected in spring, after the flooding of the previous season but prior to any mechanical soil preparation for the new crop. In contrast, cores from Mortara 3 (U-M3S and U-M3D) were collected after soil tillage. The significant increase of K_{fs} in soil cores at Mortara 3 is likely due to this land preparation, implying that extended period of flooding cause soil compaction. Even though the flow rate during the saturation phase was stable, the flow rate decreased in subsequent phases over time. Since we identified possible agglomeration of the fine soil particle fraction regardless of the compounds present in the water, particle clogging may be another possible reason for this flow reduction after flooding in winter.

The saturated hydraulic conductivity values obtained through laboratory experiments and those obtained from in-situ infiltration tests are summarized in Table 4.12.

Table 4.12: Summery of saturated hydraulic conductivity measured in the field and laboratory.

Location	Field Test			Laboratory Test	
	Test	Method (constant or falling head)	K_{fs} ($\times 10^{-6}$ m/s)	Test	K_s- ($\times 10^{-6}$ m/s)
Mortara 1				Sat-M1A	1.3
Mortara 2	IN-C-M2	Const.	31.5	Sat-M2A	0.5
Mortara 3 S	IN-F-M3S	Falling	16.1	Sat-M3S	23.7
Mortara 3 D	IN-F-M3D	Falling	7.8	Sat-M3D	30.6
Mortara 4 S	IN-F-M4S	Falling	16.5		
Mortara 4 D	IN-F-M4D	Faling	8.4		
Beinette 1	IN-C-B1	Const.	72.0		
Beinette 1	IN-F-B1	Falling	124		
Beinette 2	IN-F-B2	Falling	21.5		

The K_{fs} obtained from the constant head infiltration test at Mortara Location 2 (IN-C-M2; 31.5 $\times 10^{-6}$ ms^{-1}) result is 63 times higher than the K_s obtained by laboratory column test (Sat-M2A; 0.5 $\times 10^{-6}$ ms^{-1}). In contrast, for the falling-head infiltration tests at Mortara location 3 both shallow (IN-F-M3S) and deep (IN-F-M3D) results at Mortara Location 3 are lower than laboratory tests (Sat-M3S and Sat-M3D) values but fall withing the same order of magnitude. The relative difference in K_{fs} is 32% for the shallow test and 74% for the deep test. Hydraulic conductivity is relatively higher at elevated water content because a larger cross-sectional area of the soil matrix is available for flow, thereby reducing flow resistance. In the field, field-saturated conditions involve entrapped air within soil pores, which results in a lower effective water content and hydraulic conductivity compared to the fully saturated, degassed conditions achieved in laboratory column experiments. Because of these physical mechanisms, observing a slightly lower K_{fs} within the same order of magnitude is theoretically consistent and acceptable. Furthermore, agricultural

soil exhibits pronounced spatial heterogeneity due to macropores, such as earthworm burrows and root channels, alongside localized compaction from heavy machinery traffic. In conclusion, the falling-head infiltration method proved reliable and suitable for permeable sandy soils, whereas constant-head infiltration testing requires further investigation, particularly regarding the evaluation of steady-state flow regimes.

4.4.1.2 Preliminary tracer tests

The first preliminary column test was conducted on the U-M1A core, consisting of a saturation phase (duration: 15.4 h; Sat-M1A) followed by a tracer test (KBr-M1A) using only the conservative tracer KBr (11.90 g/L or 100 mmol/L). Both phases were performed under a constant water head of 5.5 cm at the top of the column. Because an automated fraction collector was not utilized for effluent collection, a significant number of measurement points were missed overnight (Figure 4.12, where time begins at the onset of tracer injection). Nevertheless, this preliminary test helped establish a realistic operational timeline for subsequent column experiments. Furthermore, organic matter agglomeration was observed in the effluent from this column, prompting the decision to reduce the KBr concentration in subsequent tracer tests. Due to the discontinuous sampling record, inverse modelling to determine dispersivity (α) and saturated volumetric water content was not performed on the tracer breakthrough data from this column.

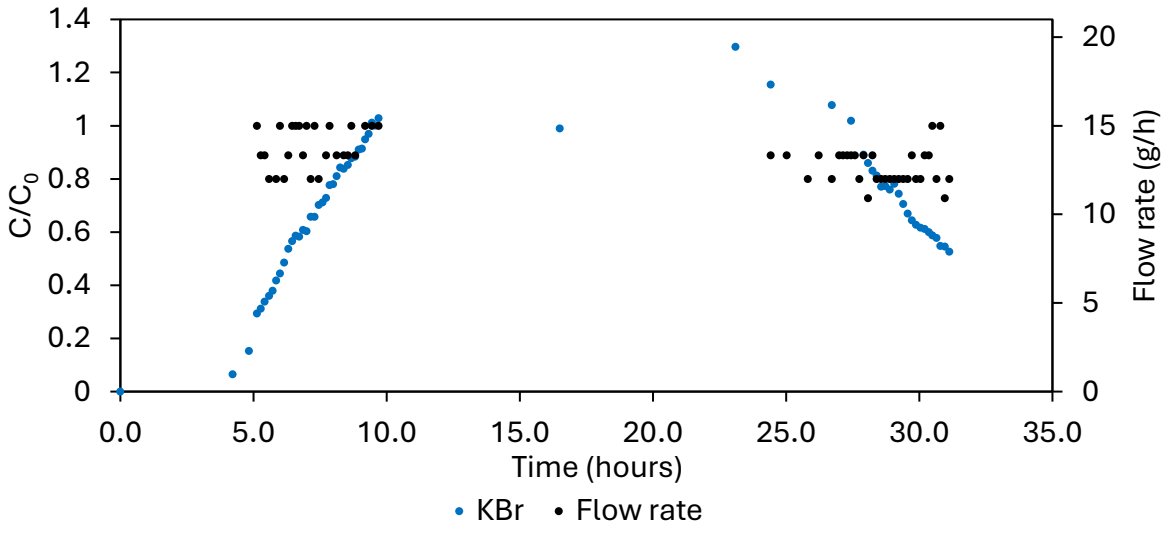


Figure 4.12: Relative concentration of KBr (C/C_0) and outflow rate during the preliminary tracer test KBr-M1A. The time scale begins at the onset of tracer injection

The second preliminary column test was performed on core U-M2A using an automated fraction collector. The saturation phase (Sat-M2A) was conducted for 16.18 h prior to the tracer test (KBr-M2A), with both phases maintained under a constant water head of 5.5 cm at the top of the column. Only the conservative tracer KBr was injected, at a reduced concentration of 3.31 g/L (27.8 mmol/L). The effluent flow rate and relative KBr concentration (C/C_0) are plotted in Figure 4.13, where the time scale begins at the onset of tracer injection.

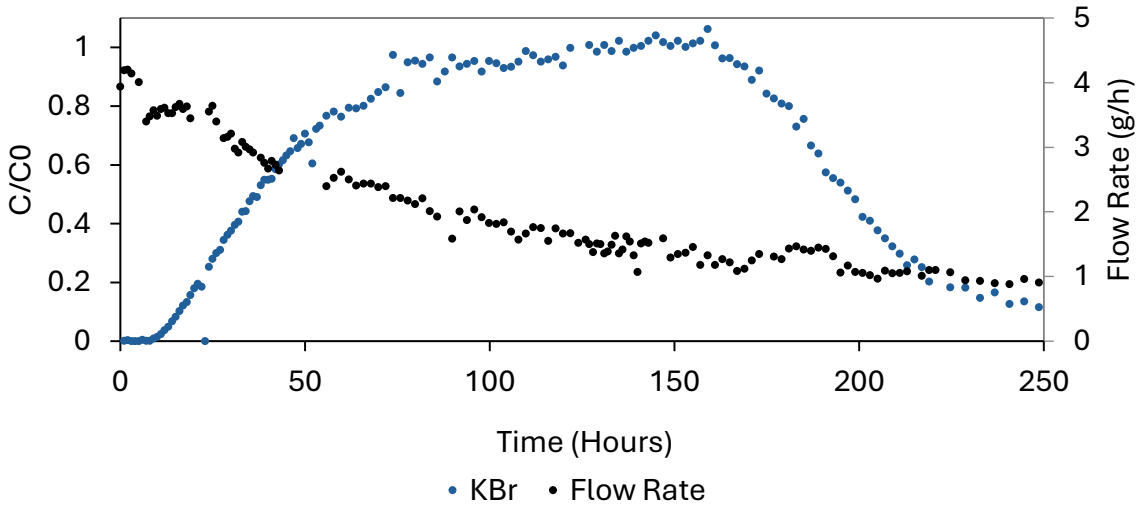


Figure 4.13: Relative concentration of KBr (C/C0) and outflow rate during the preliminary tracer test KBr-M2A. The time scale begins at the onset of tracer injection

The breakthrough curve of KBr was simulated using inverse modelling in HYDRUS-1D to estimate dispersivity (α) and saturated water content (θ_S). Because the flow rate varied over time, the average discharge during the rising limb (2.7 g/h) was used to determine the saturated hydraulic conductivity (K_S = 3.67 $\times 10^{-6}$ ms^{-1}) for the model; consequently, the simulation was fitted exclusively to the rising limb of the breakthrough curve (Figure 4.14). The calibrated parameters are summarized in Table 4.13.

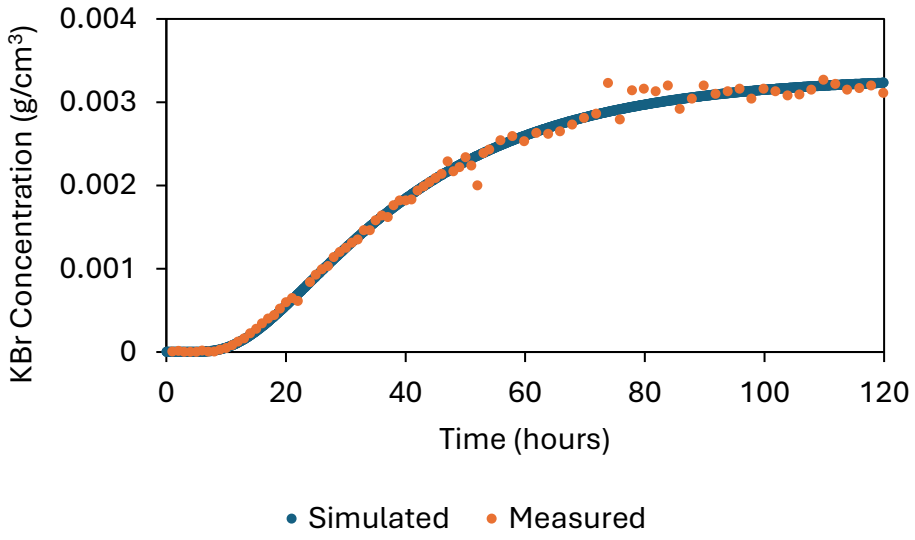


Figure 4.14: Observed and simulated KBr concentration breakthrough curves for preliminary column test KBr-M2A. Time zero corresponds to the start of tracer application.

Table 4.13: Calibrated saturated water content (θ_S) and longitudinal dispersivity (α) obtained from HYDRUS-1D inverse simulation for column U-M2A.

Parameter	Result
Saturated volumetric water content θ_S (%)	30.6
Dispersivity α (cm)	5.4

Because the flow rate became excessively low toward the end of the tracer test, no further experiments were conducted on this column core. In addition, the agglomeration test (AG-DLS) was designed to investigate whether pore-matrix clogging was directly associated with the tracer concentration used in this preliminary experiment.

4.4.1.3 Primary tracer tests

The primary tracer tests, performed simultaneously in parallel (KBr-M3S, KBr-M3D, Rh-M3S and Rh-M3D) on cores U-M3S and U-M3D, included both the conservative tracer KBr and the non-conservative tracer rhodamine. The Breakthrough Curves (BTC) for KBr and Rhodamine for core U-M3S are illustrated in Figure 4.15, along with the effluent flow rate. Corresponding curves for the U-M3D are illustrated in Figure 4.16. In both figures, the time scale begins at the onset of tracer injection (t =0 h). Tracer flushing with deionized water for the U-M3S and U-M3D columns started 58 and 25 hours after tracer injection,

respectively. The water head at the top of both columns was maintained 3.5 cm, identical to the head applied during the saturation phase.

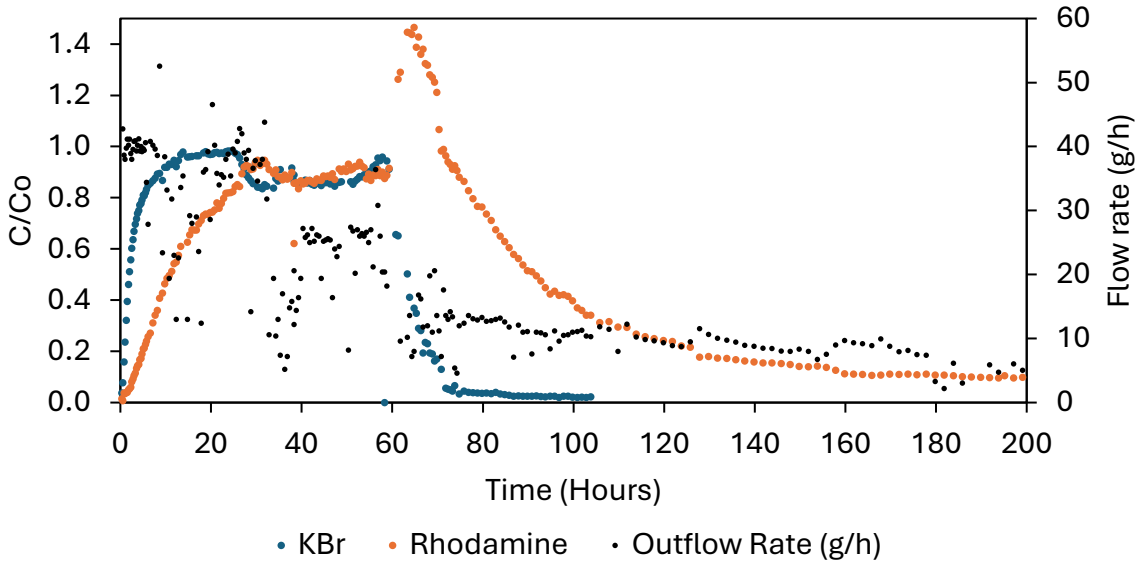


Figure 4.15: Breakthrough curves of relative concentration (C/C_0) and effluent flow rate over time for tracer tests conducted on the U-M3S core. The time scale begins at the onset of tracer injection (t = 0 h). and tracer flushing with deionized water was initiated at 58 hours.

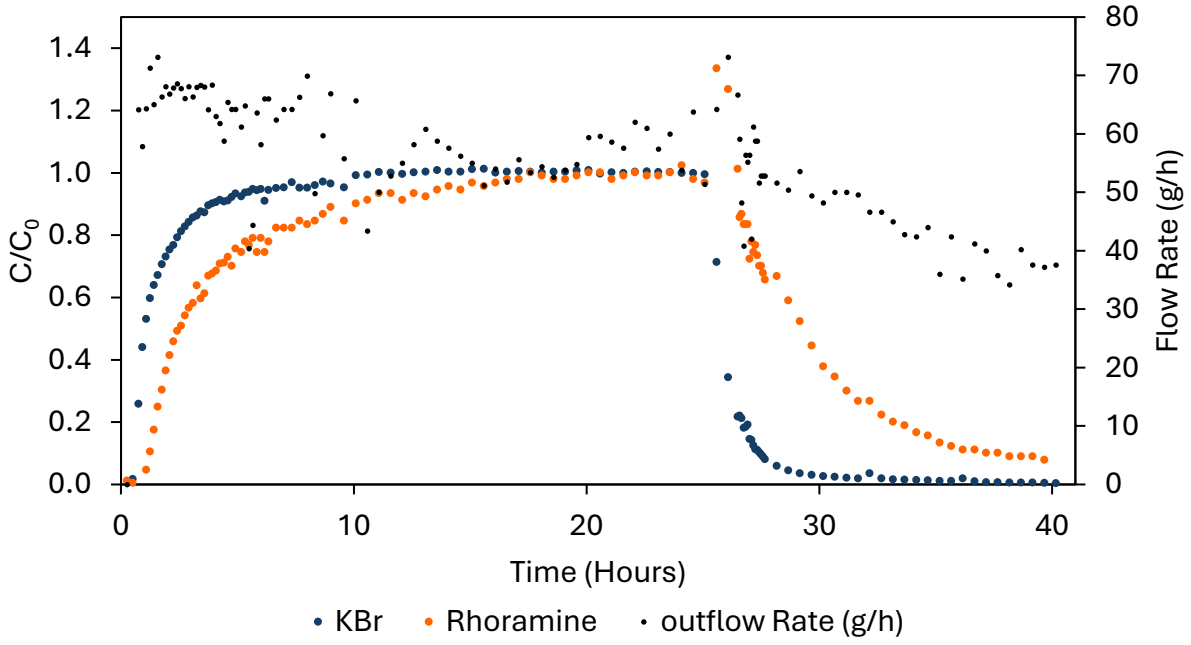


Figure 4.16: Breakthrough curves of relative concentration (C/C_0) and effluent flow rate over time for tracer tests conducted on the U-M3D core. The time scale begins at the onset of tracer injection (t = 0 h). and tracer flushing with deionized water was initiated at 25 hours.

Rhodamine showed retarded transport in both columns. Upon flushing the columns with deionized water, Rhodamine initially eluted at higher concentrations than the injected concentration ($C/C_0 > 1$) and then gradually decreased. These effects were less pronounced in the Deep column (U-M3D), possibly due to lower TOC (Table 4.6) and consequently lower affinity of rhodamine to the solid matrix. In contrast, KBr increased gradually until reaching a relative concentration of 1.0 upon starting injection. However, a decrease in relative concentration was observed for both tracers in the Shallow column (U-M3S) during the tracer injections. Furthermore, a greater variation of flow rate was observed in the Shallow column, which was caused by altered preferential flow paths due to migration of fine particles and organic matter agglomeration. Specifically, the agglomeration test (AG-DLS) verified that agglomeration occurs in the effluent itself. However, the AG-DLS test did not show any evidence of possible agglomeration caused by the injected tracer concentrations- which were identical for KBr (1.19 g/L or 10 mmol/L) and close to the rhodamine concentration (0.016 g/L for column tests verses 0.01 g/L for AG-DLS).

The BTC data of KBr were simulated using the HYDRUS-1D inverse modelling along with hydraulic conductivity calculated based exclusively on the rising limb using (36), where the input parameters specific to the rising limb of the BTC and resulting K_S values are summarized in Table 4.14:

Table 4.14: Water head, flow rate, and calculated K_S for tracer tests KBr-M3S and KBr-M3D.

Test	Water Head, H (cm)	Flow rate (g/h)	K_s ($\times 10^{-6}\ ms^{-1}$)
KBr-M3S	3.5	40.09	5.86
KBr-M3D	3.5	64.15	9.14

Saturated volumetric water content (θ_S) and dispersivity were evaluated by the model. The results are shown in Table 4.15, and the fitted models alongside the observed data are presented in Figure 4.17 and Figure 4.18. Because rhodamine BTC in both tracer tests Rh-M3S and Rh-M3D showed a lag, rhodamine was determined as a non-conservative tracer, hence those BTC were not take into account to determine K_S and θ_S. Instead,

rhodamine BTC were models using solute transport model following the procedure explained Section 3.6.

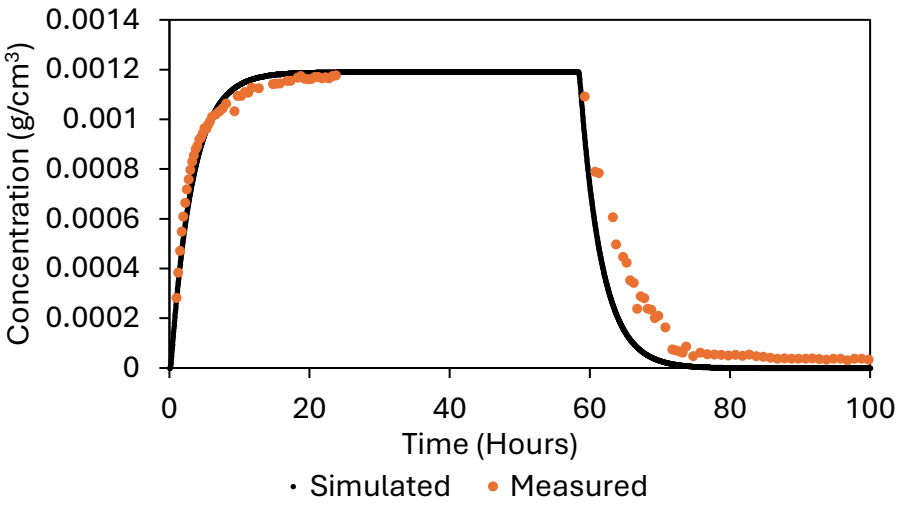


Figure 4.17: Measured and simulated KBr breakthrough curves obtained from inverse modelling for the KBr-M3S tracer test.

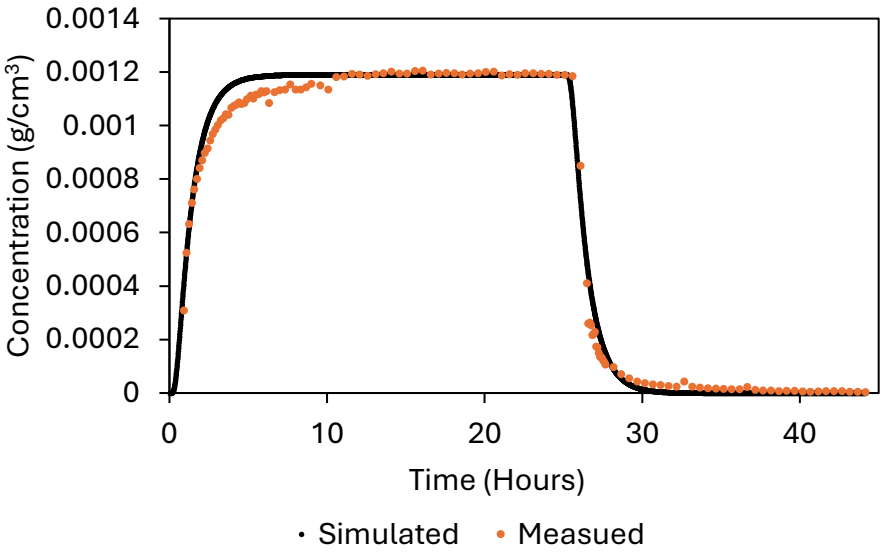


Figure 4.18: Measured and simulated KBr breakthrough curves obtained from inverse modelling for the KBr-M3D tracer test.

Table 4.15: Saturated volumetric water content (VWC) and Dispersivity of undisturbed soil samples from Mortara Location 3

Column	θ_s (%)	Dispersivity (cm)
U-M3S	38.4	60.0
U-M3D	29.8	5.7

The θs and the dispersivity of U-M3S column are high compared to that of U-M3D column. The dispersivity obtained from the inverse modelling for U-M3S was significantly high, which may have been caused by existing preferential paths. This phenomenon is very common in agricultural soils; for instance, the U-M1B column had a continuous path originating from brownish crop debris (Figure 4.19). Because of this, the void is likely a decayed root channel rather than an artificial sidewall leak. Moreover, agricultural soils can contain numerous preferential paths-such as wormholes and decayed fine roots-that are too small to be seen by the naked eye.

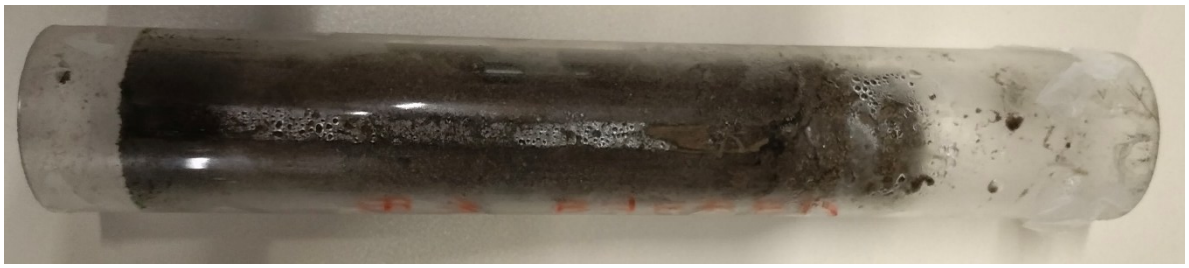


Figure 4.19: Natural preferential macropore identified in soil core U-M1B. (The right side corresponds to the top of the column.)

4.4.2 K_D Evaluation for Rhodamine

Because rhodamine was showed retarded transport compared to KBr, the BTC of rhodamine was modelled using solute transport model to determine soil distribution, coefficient (K_d) following the procedure described in Section 3.6.

Dispersivity and Saturated volumetric water content (θ_s) derived from KBr breakthrough curve (BTC) inverse modelling were used as fixed inputs parameters (Table 4.16) for the Rhodamine K_D evaluation, assuming a linear isotherm. The saturated hydraulic conductivity used for KBr BTC inverse modelling, which was corresponded to the rising limb, was also applied here. Consequently, only the rising limb was simulated (Figure 4.20 and Figure 4.21).

Table 4.16: Key input parameters for rhodamine breakthrough curve inverse modelling.

Test	K_S ($\times 10^{-6}$ m.s^{-1})	θ_s (%)	Dispersivity α (cm)
Rh-M3S	5.86	38.4	60.0
Rh-M3D	9.14	29.8	5.7

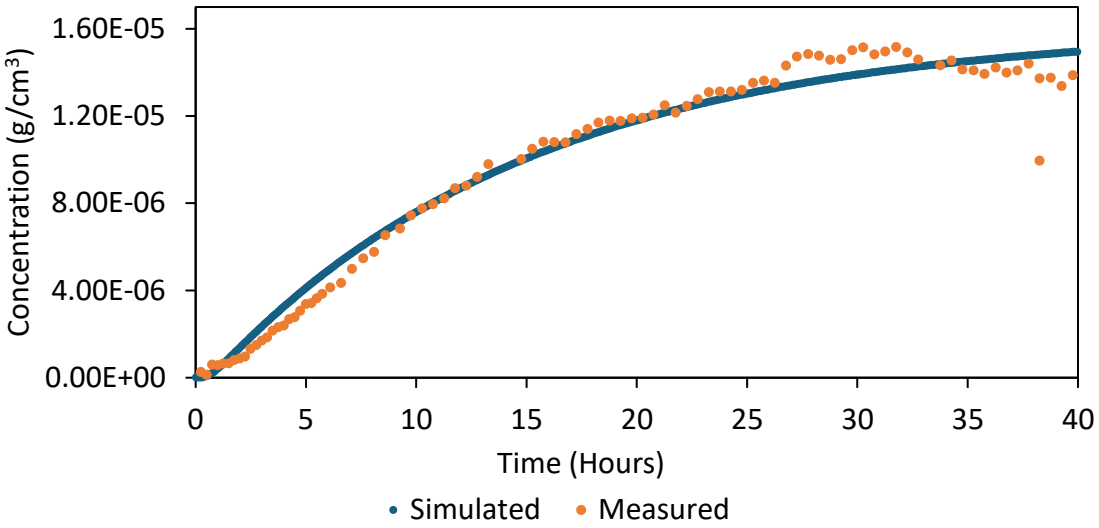


Figure 4.20: Simulated Rhodamine breakthrough curve using inverse modelling alongside measured data for the Rh-M3S.

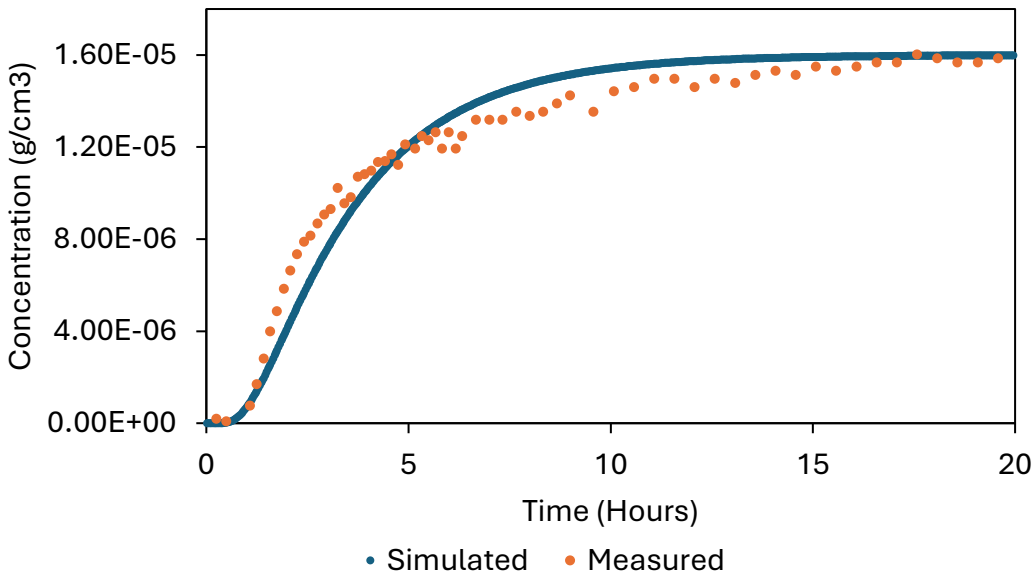


Figure 4.21: Simulated Imazamox breakthrough curve using inverse modelling alongside measured data for Rh-M3D

The soil distribution coefficients (K_d) obtained from inverse modelling are summarized in Table 4.16. The organic carbon-normalized adsorption coefficients (K_{oc}) were calculated utilizing Equation (12). Although, K_d exhibited higher variance across columns, the normalised K_{oc} values demonstrated lower variance.

Table 4.17: Estimated K_D and K_{oc} values for Rhodamine

Column	K_d (cm^3/g)	K_{oc} (cm^3/g)
Mortara 3 Shallow	0.90	0.55
Mortara 3 Deep	0.33	0.40

The AG-DLS test confirmed that there was no significant agglomeration caused by rhodamine. However, the inverse modelling of the Rhodamine BTC yielded $K_d>0$, which indicates that Rhodamine did not interact with mobile colloidal substances in the soil solution, but rather bound to the stationary soil particles.

4.4.3 Imazamox Transport Tests: Im-M3S and Im-M3D

A 20 ml volume of Imazamox solution at a concentration of 2 g/L (corresponding to a total mass of 40 mg) was applied to the drained columns. A small amount of effluent eluted upon imazamox application before flushing; no Imazamox was detected in this effluent for test Im-M3D, whereas it was detected at a high concentration of 342 mg/L for test Im-M3S. The elution of imazamox at a high concentration immediately upon application onto drained soil in core U-M3S implies the existence of preferential flow paths. The columns were subsequently flushed the following day with deionized water. The time elapsed before starting the flush was 17 hours for the shallow and 19 hours for the Deep column. The breakthrough curves for imazamox are illustrated in Figure 4.22 and Figure 4.23, with time (t=0) defined at application of imazamox.

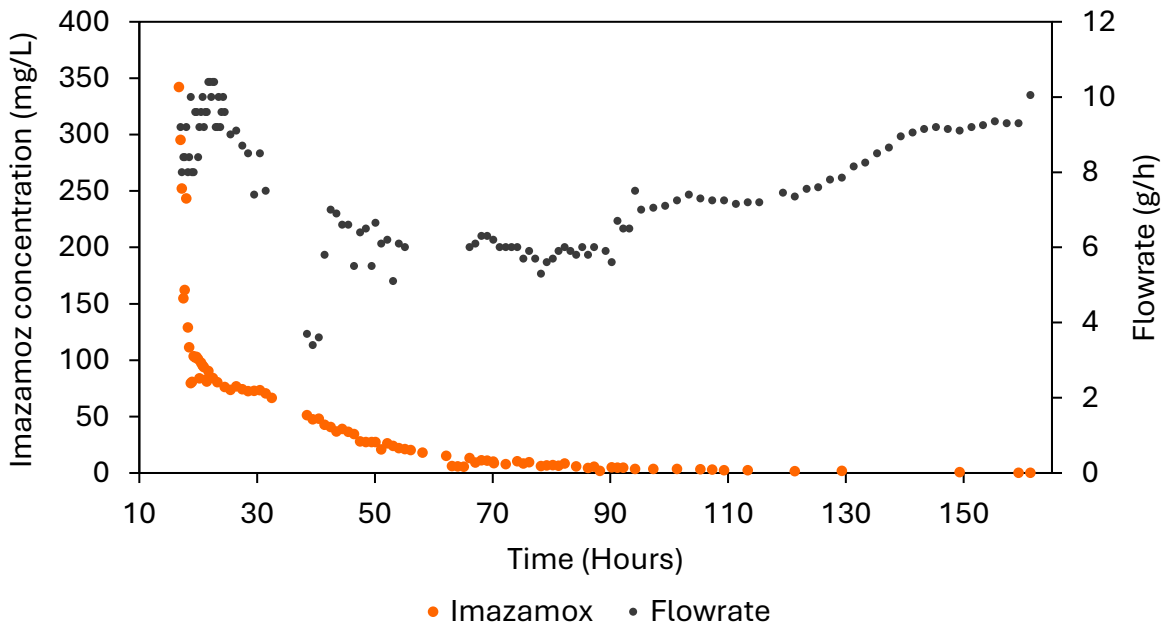


Figure 4.22: Breakthrough curve of imazamox and effluent flow rate over time for Im-M3S.

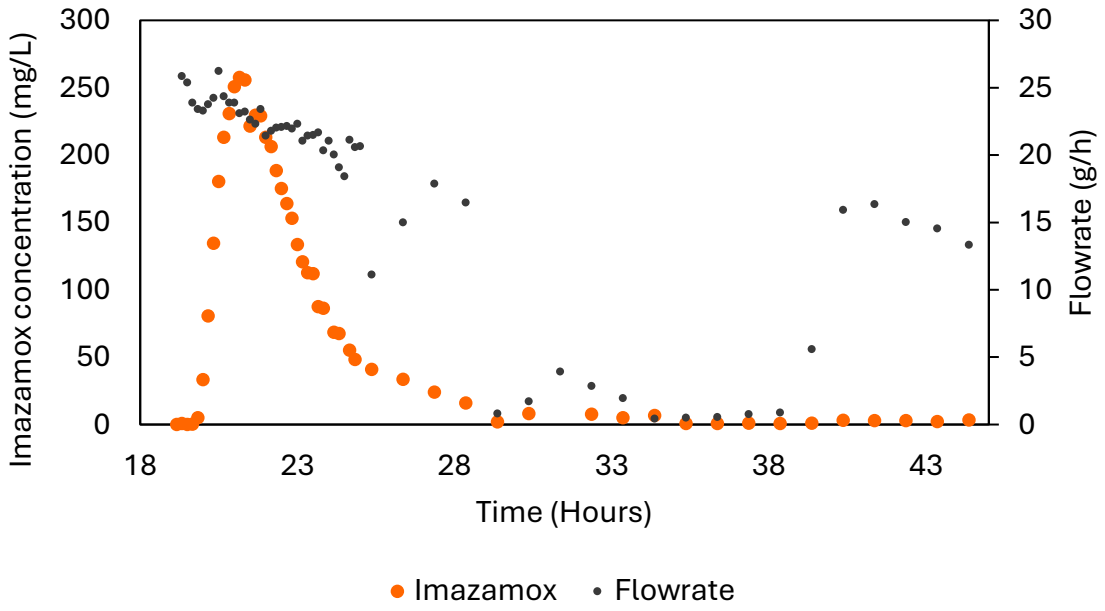


Figure 4.23: Breakthrough curve of imazamox and effluent flow rate over time for Im-M3D.

The flow rate of the Shallow column during the experiment decreased and then gradually increased without any intervention. The reduction of flow rate in the Deep column was due to partial blockage of outflow tube. Once the tube was cleaned, the flow rate recovered while maintaining the downward trend.

Holding the previously found parameters (θ_s and α) constant, and the adjusting saturated the saturated hydraulic conductivity, K_s, (Table 4.18) to match the average flow rate during the flushing stage, the distribution coefficients (K_d) of Imazamox in each column were estimated using the inverse model fitted to the BTCs. The simulations are illustrated alongside measured data in Figure 4.24 and Figure 4.25 .

Table 4.18: Flow rates during flushing phase of imazamox transport tests (Im-M3S and Im-M3D) and input parameters into inverse modelling of Imazamox BTC

Test	Outflow rate (g/h)	K_s ($\times 10^{-6}$ ms^{-1})	θ_s (%)	Dispersivity α (cm)
Im-M3S	9.14	0.13	38.4	60.0
Im-M3D	22.27	0.32	29.8	5.7

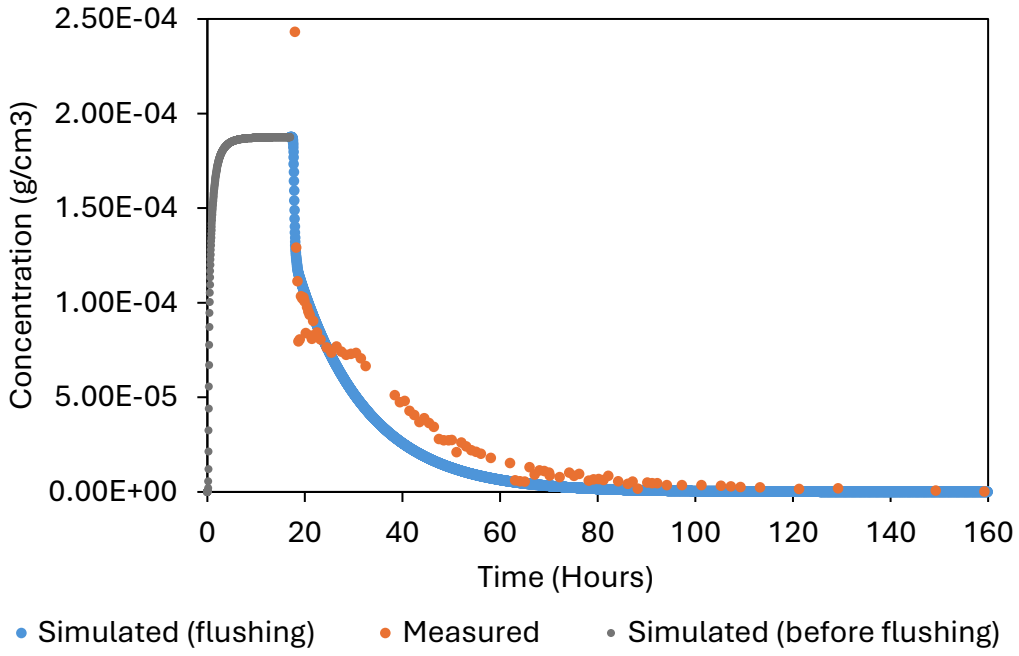


Figure 4.24: Simulated Imazamox breakthrough curve using inverse modelling alongside measured data of Im-M3S test.

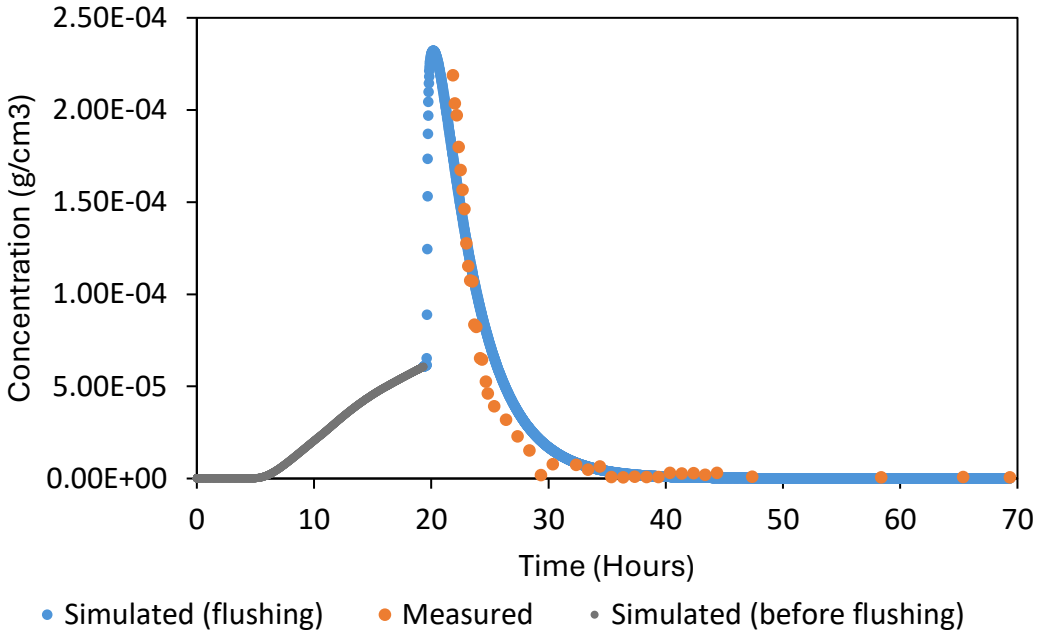


Figure 4.25: Simulated Imazamox breakthrough curve using inverse modelling alongside measured data for Im-3MD.

Because the outflow flux before starting flushing with water is very low, the cumulative effluent was collected and measured. Consequently, it was not possible to reconstruct correctly the experimental breakthrough curve of imazamox before flushing with water. Therefore, the model was not forced to fit with measured data of initial stage. Simulated BTCs before water flushing are reported in the graphs in grey just for completeness but comparison with experimental data is to be ignored. K_d was determined based on measurements taken after starting the flush. Then the organic carbon-normalized adsorption coefficient (K_{oc}) was evaluated utilizing Equation (12). Results are summarized in Table 4.18. Additionally, the mass balance calculation for imazamox showed that 93% and 94% of the applied imazamox were eluted with deionized water from U-M3S and U-M3D, respectively. Confirming these high percentages, no residual imazamox was found withing the sectioned soil profiles.

Table 4.19: Distribution Coefficient (K_D) and organic carbon-normalized adsorption coefficient (K_{oc})

Column	K_D (cm^3/g)	K_{oc} (cm^3/g)
U-M3S	0.010476	0.64
U-M3D	0.064261	7.84

K_{oc} for the parent compound of imazamox ranges from 2 to 130 cm^3/g (Buerge et al., 2019). The value determined for U-M3S was underestimated relative to this literature range while U-M3D fell withing the range. Because U-M3S was identified as a core containing preferential paths-as evidenced by the large dispersivity (60 cm) and the immediate leaching of Imazamox upon application onto drained soil-the results obtained from this column are likely biased. Consequently, the K_{OC} value derived from U-M3S is not reliable, and this underestimated value cannot be meaningfully compared with the result obtained from core U-M3D or literature value. However, the higher mass balance of eluted imazamox, the lack of residual withing the soil profile, and low K_{oc} values collectively confirm high compound mobility, highlighting the need for rigorous environmental management during the application of Imazamox in Ag-MAR.

5 Ag-MAR Modelling

Two types of simulations were performed to evaluate different scenarios: Type A (1D vadose zone modelling), representing groundwater table rise during flooding, and Type B (analytical mound modelling), representing groundwater mound (Figure 5.1) variation during and after the flooding event considering three-dimensional groundwater flow.

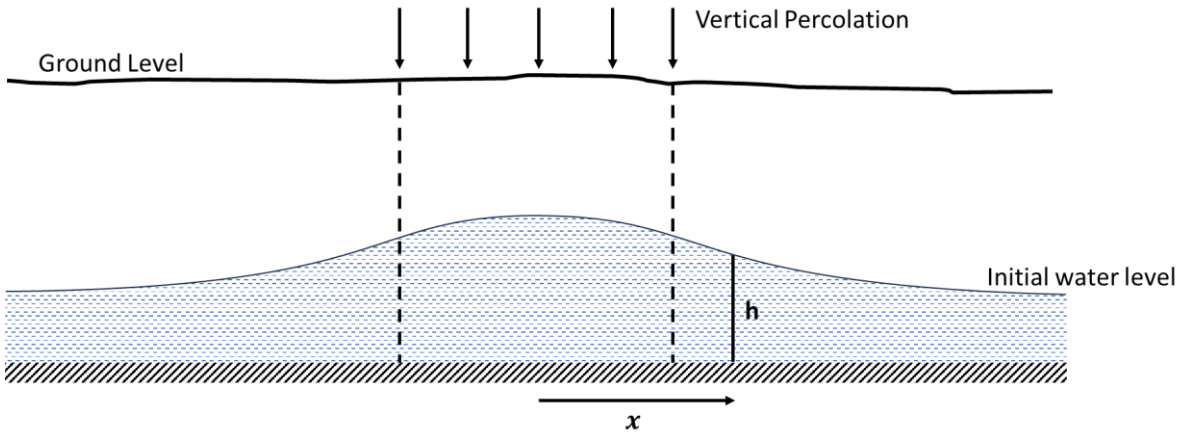


Figure 5.1: Schematic of transient groundwater mound formation during localized infiltration recharge (modified after (Hantush, 1967)

Each type of simulation was run under two ponding water layers (8 cm and 16 cm) for both the Mortara and Beinette study sites. For the Mortara site, four realizations were simulated for each type based on the combinations of the two ponding layers and the saturated hydraulic conductivity obtained from laboratory versus field tests. In contrast, simulations for the Beinette site were limited to two realizations for each type, using the saturated hydraulic conductivity obtained from field infiltration tests under the two ponding water layers. All simulations are summarized in Table 5.1.

Table 5.1: Summary of all simulations

Simulation ID	Site	Ponding depth (cm)	K_s source
Type A -groundwater table variation			
AM-8L	Mortara	8	Laboratory
AM-16L	Mortara	16	Laboratory
AM-8F	Mortara	8	Field
AM-16F	Mortara	16	Field
AB-8F	Beinette	8	Field
AB-16F	Beinette	16	Field
Type B- Groundwater mound variation			
BM-8L	Mortara	8	Laboratory
BM-16L	Mortara	16	Laboratory
BM-8F	Mortara	8	Field
BM-16F	Mortara	16	Field
BB-8F	Beinette	8	Field
BB-16F	Beinette	16	Field

Note. ID nomenclature: [Type][Site]-[Ponding Depth][Parameter Source] (e.g., AM-8L = Type A, Mortara, 8 cm ponding depth, Laboratory K_S).

Simulations for the Beinette site were evaluated considering a uniform soil profile (Soil 1). In contrast, the Mortara site was simulated using two soil layers: the first layer represented the soil down to 20 cm below the surface (Soil 2), while the layer below 20 cm depth was considered a uniform soil profile (Soil 3). The properties of each soil material are summarized in Table 5.2.

Table 5.2: Summary of physical and hydraulic properties of soil profiles

Site	Material ID	Depth interval (cm)	Initial water content θ_i [-]	Saturated water content θ_S [-]	Saturated hydraulic conductivity K_S ($\times 10^{-6}$ m/s)		Dry bulk density (g/cm^3)
					Laboratory	Field	
Beinette	Soil 1	0-50+	0.14	0.38	-	57.8	1.65
Mortara	Soil 2	0-20	0.285	0.345	2.49	21.4	1.63
Mortara	Soil 3	20-50+	0.076	0.298	30.6	8.09	1.55

Note. Initial water content refers to the measured water content of the soil when the samples were collected.

The initial groundwater table depth was set to 10.09 m for Beinette, based on the average groundwater level in November 2025, and to 2.3 m for Mortara, reflecting the average level observed over the 2020–2024 period.

5.1 Type A: 1D Vadose Zone Modelling

Water table rise under the ponding water layer was simulated in HYDRUS-1D using the variable pressure head (Equation 37) upper boundary condition and the deep drainage lower boundary condition (Equation 42; Hopmans & Stricker, 1989; Neto et al., 2016):

$$q_L(t) = A\, exp\left[-B\,|h_L - h_{gw}|\right] \qquad (42)$$

where $q_L(t)$ is the imposed lower boundary flux at time t, h_L is the transient pressure head at the lower boundary, h_{gw} is the long-term average groundwater level relative to the lower boundary, and A and B are site-specific empirical parameters, they and were not available for the study areas or neighbouring sites. Therefore, these values were adopted from (Neto et al., 2016), corresponding to fine- to medium-grained sand with an abundant clay matrix. As a result, the simulated water table rise carries higher uncertainty.

The saturated hydraulic conductivity was set to the average value obtained from either laboratory or field infiltration tests, depending on the simulation type. The initial water content, saturated water content, and van Genuchten parameters were kept identical across the all simulations in the same site. The van Genuchten-Mualem model (Equation 8) without hysteresis was selected to represent the unsaturated soil hydraulic properties.

At the upper boundary, a constant ponding layer was maintained throughout the entire simulation.

The soil profile for Beinette was configured as a single soil material down to a depth of 15 m. In contrast, Mortara had two soil materials: from the surface to 20 cm, and from 20 cm down to 5 m. The initial water content below the reference water table (2.3 m below the surface for Mortara and 10.09 m below the surface for Beinette) was set to the saturated water content (θ_s) for both sites. Above the water table, the initial moisture content for Beinette was assigned to decrease linearly up to the average water content measured during soil sample collection. For Mortara, the initial moisture content above the water table decreased linearly up to the water content specified at the layer interface (20 cm) to match the average water content measured during sampling (U-M3D and U-M4D), with a uniform initial water content then applied throughout the upper 0–20 cm layer.

Table 5.3: Summary of soil profile of Mortara for modelling type A.

Depth (cm)	Material ID	Initial Water content (-)
0-20	Soil 2	0.285
20-500	Soil 3	0.076–0.298 (from 20 cm to GWT) 0.298 (below GWT)

Note. GWT: Groundwater table (located at 2.3 m below ground surface.

Table 5.4: Summary of soil profile of Beinette for modelling type A

Depth (cm)	Material ID	Initial water content (-)
0-1500	Soil 1	0.14–0.38 (from surface to GWT) 0.38 (below GWT)

Note. GWT: Groundwater table (located at 10.09 m below ground surface.

The results obtained by numerical simulations with above initial conditions, soil profiles and boundary conditions are summarized in Figure 5.2.

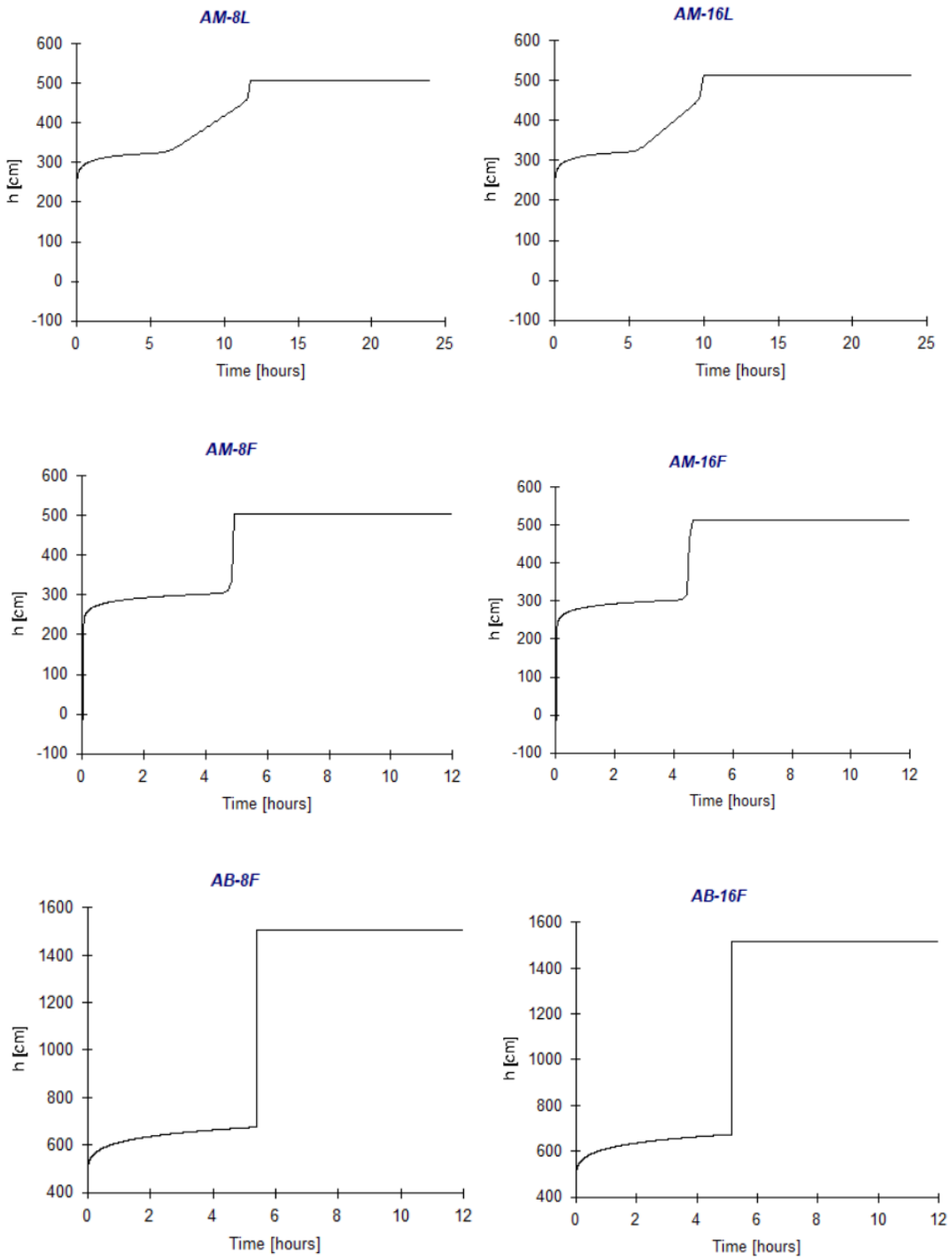


Figure 5.2: Water pressure head variation at the bottom of the simulated soil profile (AM-8L, AM-16L, AM-8F, and AM-16F: 5 m depth; AB-8F and AB-16F: 15 m depth) under deep drainage lower boundary conditions.

The lower boundary of the simulated soil profile remained continuously saturated, as the initial groundwater table was located well above it (2.7 m above the bottom for Mortara; 4.91 m for Beinette). Therefore, other pressure components are negligible compared to hydrostatic pressure, making the pressure head at the bottom equal to the saturated water column. The sharp rise observed between 4 and 6 hours in AM-8F, AM-16F, AB-8F, and AB-16F occurs because the wetting front from the surface meets the bottom water table, forming a continuous saturated layer from the bottom boundary to the ponded surface and suddenly transmitting the full hydrostatic pressure.

Comparing the 16 cm ponding water depth simulations with their corresponding 8 cm scenarios (AM-8L vs. AM-16L, AM-8F vs. AM-16F and AB-8F Vs. AB-16F), the time required for the groundwater table to reach the ground surface (h = 500 cm for AM-8L, AM-16L, AM-8F, and AM-16F; h = 1500 cm for AB-8F and AB-16F) is nearly identical, being only slightly shorter under the 16 cm ponding depth. However, a significant difference in time is observed between simulations parameterized using laboratory-derived versus field-measured saturated hydraulic conductivity values (AM-8L vs. AM-8F and AM-16L vs. AM-16F).

In conclusion, the testing methodology adopted to determine input parameters significantly affects the reliability and certainty of the model results, whereas the ponding water depth exerts a negligible impact on the rate of water table rise under deep drainage lower boundary conditions.

5.2 Type B: Analytical Mound Modelling

The groundwater mound was simulated in two steps. In the first step, the steady-state downward flux q [LT^{-1}] was obtained through HYDRUS-1D considering a 50 cm soil profile for both sites. The upper and lower boundary conditions were set to a variable pressure head (Equation 37) and free drainage (Equation 38), respectively. Beinette was simulated considering a single, uniform soil material (Soil 1). In contrast, the Mortara site was simulated considering two layers: from the surface to 20 cm (Soil 2), and from 20 cm down to 50 cm (Soil 2). The initial water content of each soil material was set to the average water content measured during soil sample collection (Table 5.5 and Table 5.6).

Table 5.5: Summary of infiltration soil profile of Mortara for modelling type B.

Depth (cm)	Material ID	Initial Water content θ_i (-)
0-20	Soil 2	0.285
20-50	Soil 3	0.076

Table 5.6: Summary of infiltration soil profile of Beinette for modelling type B.

Depth (cm)	Material ID	Initial water content θ_i (-)
0-50	Soil 1	0.14

Using these soil profiles and the boundary conditions described above, the steady-state downward percolation fluxes were obtained via one-dimensional numerical simulations in HYDRUS-1D; they are summarized in Table 5.7.

Table 5.7: Simulated steady-state infiltration fluxes (q).

Simulation	q ($\times 10^{-6}$ m/s)
BM-8L	5.78
BM-16L	6.83
BM-8F	8.08
BM-16F	8.08
BB-8F	57.8
BB-16F	57.8

The steady-state infiltration fluxes (q) for simulations BM-8F, BM-16F, BB-8F, and BB-16F were strictly equal to the saturated hydraulic conductivity of the bottom layer, as the free drainage boundary condition enforces a unit hydraulic head gradient $(\partial H/\partial z = 1,)$. In contrast, BM-8L and BM-16L yielded different flux values because the less permeable topsoil layer acted as a hydraulic bottleneck, limiting the downward flux through the upper stratum rather than the lower boundary condition.

The second step of the simulation evaluated the growth and decay of the water table mound Figure 5.1 in response to the steady-state vertical flux q obtained from the HYDRUS-1D model, using the analytical solution developed by Hantush (1967). The mathematical solution was solved numerically using a dedicated MATLAB script developed by the Groundwater Engineering Research group at DIATI, Politecnico di Torino, ready for execution upon updating the geometric dimensions and hydrogeological parameters of each site. This analytical solution was developed to represent three-dimensional groundwater flow both during the active flooding stage and following the cessation of infiltration, assuming an unconfined, homogeneous, and isotropic aquifer resting on a horizontal impermeable base (Hantush 1967). The recharge area was assumed to be square to ensure symmetry along both principal horizontal axes. Furthermore, an identical recharge area was applied to both sites to enable a direct comparison between them.

The thickness of the shallow aquifer in Beinette is taken as 30 m according to field tests performed by the Groundwater Engineering Group at DIATI (2026). The effective porosity was adopted as 0.20 according to the lithology (clean coarse gravel and sandy gravel alluvium (Johnson, 1967) reported by Taramasso et al., (2025). In Mortara, the height of the saturated unconfined layer is 60.0 m (Comune di Mortara, 2023), and the effective porosity was set to 0.15 for unconsolidated alluvial sands (Johnson, 1967). The hydraulic conductivities for Beinette and Mortara are in the order of magnitude of 10^{-3} m/s (field experiments by DIATI, 2026) and 10^{-5} m/s (Regione Piemonte, 2018), respectively. Both two sites were simulate considering 1-hectare recharging plot (100 × 100 m). Active recharge was simulated as a 1-day recharge pulse followed by post-loading dissipation. All the input parameters of the model are summarized in Table 5.8.

Table 5.8:Input hydrogeological and geometrical parameters for the Hantush analytical mound model.

Parameter	Unit	Beinette	Mortara
Water table depth (m)	m	10.09	2.30
Aquifer initial thickness (h_i)	m	30	60
Hydraulic conductivity (K)	m/s	1E-3	1E-5
Effective porosity (ϵ)	-	0.20	0.15
Basin width	m	100	100
Basin length	m	100	100
Recharge duration	days	1	1
Simulation total duration	days	4	4

Using these parameters, the water table mound growth and dissipation were simulated. The resulting spatial distributions of the groundwater mound profiles along one principal axis is presented in Figure 5.3.

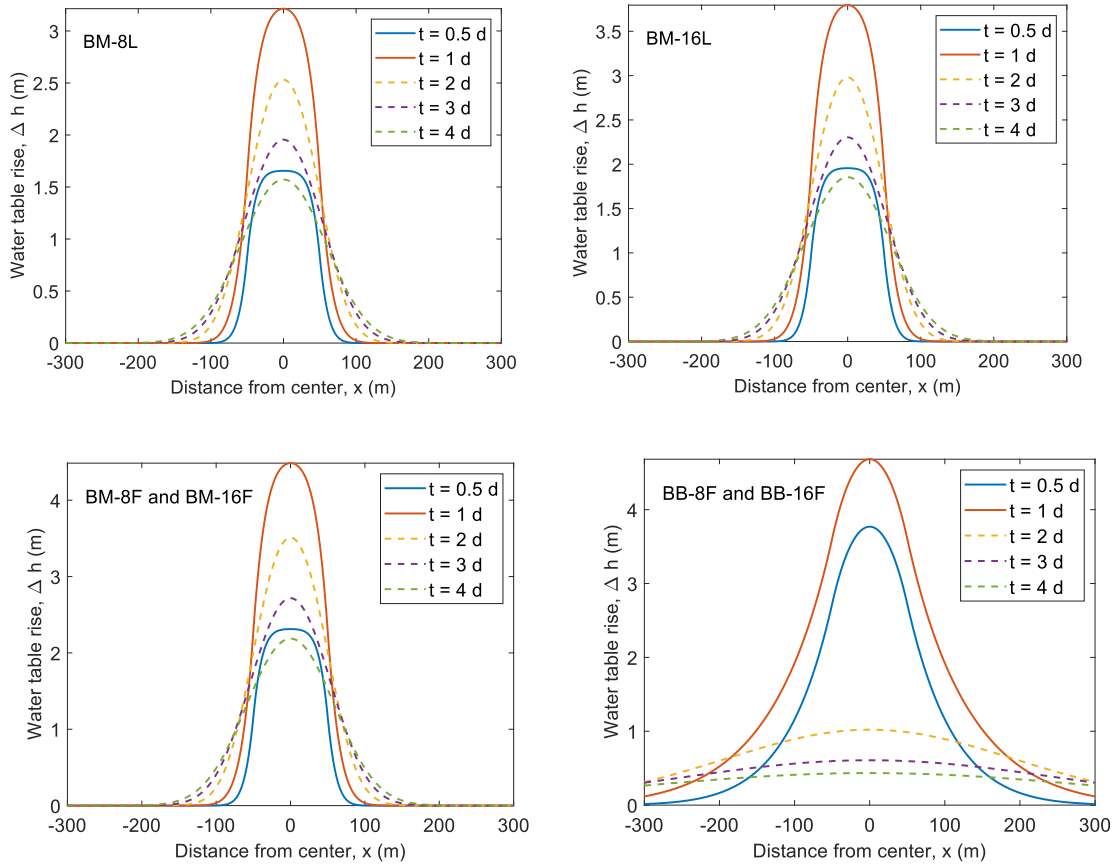


Figure 5.3:Simulated groundwater mounds (Δh) under a 1-day pulse recharge event. Solid curves denote active infiltration, and dashed curves illustrate post-recharge dissipation relative to the initial water table (Δh = 0 m).

From the perspective of physical boundaries, the simulations for Mortara (BM-8L, BM-16L, BM-8F, and BM-16F) exceed both the lower boundary of the infiltration layer (Δh = 1.8 m) and the ground surface elevation (Δh = 2.30 m). However, critical hydrogeological insights can still be derived under the theoretical assumption that the water table remains sufficiently deep to avoid intersecting these upper boundaries.

BM-8L and BM-16L differ by their ponding water layers of 8 cm and 16 cm, respectively. The mound difference at 1 day is about 0.5 cm, which is significant considering the total volume infiltrated over the area. In contrast, BM-8F and BM-16F are identical due to having the same downward percolation rate even with different ponding layers. Furthermore, BM-8L and BM-16L were simulated using saturated hydraulic conductivity obtained from laboratory experiments, whereas BM-8F and BM-16F were simulated considering values obtained from field tests. The simulations based on field data show a significant difference compared to those based on laboratory values, highlighting that the testing method used for input parameters has a very significant effect on the modelling results.

For the Beinette site, BB-8F and BB-16F are likewise identical because downward percolation rates remain uniform between them. Throughout all time steps, the simulated mounds remain well below the ground surface (Δh < 10.09 m). Driven by the aquifer's high hydraulic conductivity (K = 1 $\times 10^{-3}$ m/s) and effective porosity (0.2), the mound spreads laterally over a wide footprint. Consequently, despite a considerably higher percolation rate (q = 57.8 $\times 10^{-6}$ m/s), the peak water table rise is of a comparable magnitude to BM-8F and BM-16F (q = 8.08 $\times 10^{-6}$ m/s). However following the active recharge pulse, the mound declines sharply, dissipating rapidly through lateral drainage.

These results indicate that surface ponding depth exerts minimal control over groundwater recharge when rate-limiting strata govern the lower profile. Moreover, high aquifer hydraulic conductivity accommodates substantial recharge volumes with modest water table rises—fostering favourable conditions for compact recharge plots while accelerating lateral discharge toward downstream drainage boundaries, reducing resident time which is not good in the point of storage.

6 Conclusions

One of the major problems in the world is groundwater depletion induced by climate change. Northern Italy is a water-intensive crop-growing region dominated by rice and maize, which amplifies the effect through a positive feedback loop. A promising solution to address groundwater depletion is Agricultural Managed Aquifer Recharge (Ag-MAR), supported by the abundant water availability in the off-growing season and the dense, well-organized irrigation canal system in the area. In particular, Ag-MAR requires neither dedicated land nor additional infrastructure to be implemented. However, numerous challenges are encountered during modelling, planning, and operational management due to a substantial lack of standardized characterization methodologies and regulatory frameworks (Alam et al., 2021; Levintal, Kniffin, et al., 2023). This study obtained notable different results between field infiltration tests and laboratory experiments, which were performed under different controlled boundary conditions.

Granulometry analysis classified the soil at both sites as sand, with the sand particle percentage exceeding 96% across all soil samples. The permeability is significantly high, creating practical difficulties when performing single-ring constant-head infiltration tests due to the significant cumulative infiltration that occurred before the initial reading—which prevented obtaining reliable measurements in the transient flow regime. However, this method could still be used to evaluate the steady-state flow regime, although the duration of the steady-state period was limited by the volume capacity of the Mariotte reservoir, especially in such permeable soils. In contrast, the falling-head infiltration experiments yielded field-saturated hydraulic conductivity (K_{fs}) values within the same order of magnitude (10^{-6} to 10^{-5} $m.s^{-1}$) as the saturated hydraulic conductivity evaluated in the laboratory, implying that the single-ring falling-head infiltration method is more suitable for highly permeable sandy soils. Moreover, the constant-head single-ring test in the steady-state flow regime and the falling-head infiltration test yielded the same order of magnitude for K_{fs} at the same location, implying that they are practically interchangeable. However, further studies are suggested to verify this comparability.

Furthermore, saturated hydraulic conductivity (K_s) measurements on undisturbed soil cores showed a significantly reduced hydraulic conductivity after winter flooding

compared to the values after soil preparation. This implies that the soil matrix may clog due to prolonged flooding, as also supported by the gradual reduction in effluent flow rate observed over time during the column tests.

One analyzed column was identified as having preferential paths within its soil matrix, introducing bias into the measurements; therefore, for comparison with literature values, the results obtained from the other column were used. The organic carbon-normalized partition coefficient (K_{OC}) of imazamox (7.84 cm^3g^{-1}) was near the lower boundary of reported literature values. In fact, a high percentage of applied imazamox was eluted with deionized water (93% in the shallow and 94% in the deep column). Additionally, no residual imazamox was detected in the sectioned soil profiles. These findings demonstrate high compound mobility and a strong susceptibility to leaching through the vadose zone.

Additionally, Ag-MAR numerical modelling demonstrated that ponding water depth does not significantly affect downward infiltration rates under free-drainage conditions when the groundwater table remains deep, especially given the lower permeability of underlying stratigraphical layers relative to the surface soil. Under these conditions, infiltration is governed primarily by a unit hydraulic gradient and limited by those less permeable layers. Furthermore, the simulation outputs showed high variability depending on the input parameters, proving that the experimental methods chosen to obtain these parameters are crucial for reliable predictions.

In conclusion, while highly permeable sandy soil and the regional irrigation network support efficient Ag-MAR operations, the feasibility study should be completed by means of pilot tests and a more detailed hydrogeological assessment would be necessary to build a numerical 3D model to simulate the impacts of the MAR system.

7 Bibliography**Cook**

AdbPo. (2020). *Piano di Assetto Idrogeologico (PAI) – Delimitazione delle fasce fluviali*. Autorità di Bacino Distrettuale del Fiume Po. https://www.adbpo.it/

AIPo & Regione Lombardia. (2022). *Reticolo Idrografico Principale di Competenza AIPo (Corsi_acqua_AIPO)*. Agenzia Interregionale per il fiume Po & Geoportale della Lombardia. https://www.geoportale.regione.lombardia.it/

Alam, S., Borthakur, A., Ravi, S., Gebremichael, M., & Mohanty, S. K. (2021). Managed aquifer recharge implementation criteria to achieve water sustainability. *Science of The Total Environment*, *768*, 144992. https://doi.org/10.1016/j.scitotenv.2021.144992

AQUASTAT. (n.d.). *AQUASTAT Core Database*. Food and Agriculture Organization of the United Nations. Retrieved 1 May 2024, from https://www.fao.org/aquastat/en/databases/maindatabase/

ARPA Piemonte. (2025). *Rete di Monitoraggio Piezometrico delle Acque Sotterranee – Stazione 00401610001 (Beinette, GWB-S7)*. Agenzia Regionale per la Protezione Ambientale del Piemonte. https://www.arpa.piemonte.it/

Autorità di Bacino Distrettuale del Fiume Po. (2021). *Piano di Gestione del Distretto Idrografico del Fiume Po: Riesame e aggiornamento al 2021 – Tavola 1.7: Corpi idrici sotterranei – Sistema superficiale di pianura, sistema collinare-montano e fondovalle*. https://pianoacque.adbpo.it/

Battegazzore, M., & Morisi, A. (n.d.). *Environmental Evaluation of Springs in the Intensely Cultivated and Industrialized Inland Plain of Cuneo (Northwest Italy)*.

Bear, J. (1988). *Dynamics of fluids in porous media*. Dover publications.

Beretta, G. P., La Vigna, F., Camera, C. A. S., Gafà, R. M., Citrini, A., Martarelli, L., Monti, G. M., Roma, M., Silvi, A., Vitale, V., Fiori, C., Masetti, M., Pascarella, F., & Proietti, R. (2021). *Carta Idrogeologica d'Italia / Hydrogeological Map of Italy (Scala 1:500.000) – Foglio 01* [Map]. ISPRA (Istituto Superiore per la Protezione e la Ricerca Ambientale) and Università degli Studi di Milano.

Buerge, I. J., Bächli, A., Kasteel, R., Portmann, R., López-Cabeza, R., Schwab, L. F., & Poiger, T. (2019). Behavior of the Chiral Herbicide Imazamox in Soils: pH-Dependent, Enantioselective Degradation, Formation and Degradation of Several Chiral Metabolites. *Environmental Science & Technology*, *53*(10), 5725–5732. https://doi.org/10.1021/acs.est.8b07209

Colombo, P., Mazzon, P., & Alberti, L. (2024). Off-season irrigation as a climate adaptation strategy for future groundwater management in Northern Italy. *Advances in Geosciences*, *64*, 27–31. https://doi.org/10.5194/adgeo-64-27-2024

Comune di Mortara. (2023). *Documentazione tecnica e allegati ambientali per la pianificazione e gestione delle acque*. Comune di Mortara. https://www.comune.mortara.pv.it/amministrazione/trasparenza/pubblicazioni/allegati/allegato_2923.html

Cook, B. I., Mankin, J. S., Marvel, K., Williams, A. P., Smerdon, J. E., & Anchukaitis, K. J. (2020). Twenty-First Century Drought Projections in the CMIP6 Forcing Scenarios. *Earth's Future*, *8*(6), e2019EF001461. https://doi.org/10.1029/2019EF001461

Dahlke, H. E., Brown, A. G., Orloff, S., Putnam, D., & O'Geen, T. (2018). Managed winter flooding of alfalfa recharges groundwater with minimal crop damage. *California Agriculture*, *72*(1), 1–11. https://doi.org/10.3733/ca.2018a0001

Dane, J. H., Topp, G. C., & Campbell, G. S. (Eds). (2002). *Methods of soil analysis: Part 4: Physical methods*. Soil Science Society of America. https://doi.org/10.2136/sssabookser5.4.frontmatter

Dillon, P., Pavelic, P., Page, D., Beringen, H., & Ward, J. (2009). Managed aquifer recharge: An introduction. *Waterlines Report*, *13*.

Egidio, E., De Luca, D. A., Cocca, D., & Lasagna, M. (2025). Spatio–Temporal Dynamics of Groundwater Levels in the Piedmont Po Plain (NW Italy): Impacts of Climate Change and Land Use. *Water*, *17*(18), 2712. https://doi.org/10.3390/w17182712

ERSAF & Regione Lombardia. (2010). *Carta Pedologica della Lombardia in scala 1:250.000 (WIZ_U32WG_VS_SIT_PACSI_CARTA_PED_250K)*. Ente Regionale per i Servizi all'Agricoltura e alle Foreste & Geoportale della Lombardia. https://www.geoportale.regione.lombardia.it/

ERSAF & Regione Lombardia. (2021). *DUSAF 7.0 – Destinazione d'Uso dei Suoli Agricoli e Forestali*. Ente Regionale per i Servizi all'Agricoltura e alle Foreste & Geoportale della Lombardia. https://www.geoportale.regione.lombardia.it/

Eurostat. (n.d.). *Water Abstraction by Source and Sector* (Dataset: Env_wat_abs). Statistical Office of the European Union, European Commission. Retrieved 1 May 2024, from https://ec.europa.eu/eurostat/databrowser/view/env_wat_abs/default/table

FAO. (2020). *The State of Food and Agriculture 2020*. FAO. https://doi.org/10.4060/cb1447en

Hantush, M. S. (1967). Growth and decay of groundwater-mounds in response to uniform percolation. *Water Resources Research*, *3*(1), 227–234. https://doi.org/10.1029/WR003i001p00227

Hopmans, J. W., & Stricker, J. N. M. (1989). STOCHASTIC ANALYSIS OF SOIL WATER REGIME IN A WATERSHED. *Journal of Hydrology*, *105*(1–2), 57–84. https://doi.org/10.1016/0022-1694(89)90097-4

IPCC. (2023). *SYNTHESIS REPORT OF THE IPCC SIXTH ASSESSMENT REPORT (AR6)*.

ISTAT. (2023). *Confini delle unità amministrative a fini statistici (Regioni e Province)*. https://www.istat.it/it/archivio/104317

Jasechko, S., Seybold, H., Perrone, D., Fan, Y., Shamsudduha, M., Taylor, R. G., Fallatah, O., & Kirchner, J. W. (2024). Rapid groundwater decline and some cases of recovery in aquifers globally. *Nature*, *625*(7996), 715–721. https://doi.org/10.1038/s41586-023-06879-8

Jia, Z., Li, J., Gao, L., Yang, D., & Kanaev, A. (2023). Dynamic Light Scattering: A Powerful Tool for In Situ Nanoparticle Sizing. *Colloids and Interfaces*, *7*(1), 15. https://doi.org/10.3390/colloids7010015

Johnson. (1967). *Specific yield: Compilation of specific yields for various materials* (Nos 1662-D; Water Supply Paper). U.S. Geological Survey. https://doi.org/10.3133/wsp1662D

Karickhoff, S., Brown, D., & Scott, T. (1979). Sorption of hydrophobic pollutants on natural sediments. *Water Research*, *13*(3), 241–248. https://doi.org/10.1016/0043-1354(79)90201-X

Kummu, M., Guillaume, J. H. A., De Moel, H., Eisner, S., Flörke, M., Porkka, M., Siebert, S., Veldkamp, T. I. E., & Ward, P. J. (2016). The world's road to water scarcity: Shortage and stress in the 20th century and pathways towards sustainability. *Scientific Reports*, *6*(1), 38495. https://doi.org/10.1038/srep38495

Lasagna, M., Mancini, S., De Luca, D. A., & Cravero, M. (2019). Piezometric levels in the Piedmont plain (NW Italy): Trend and hydrodynamic behaviour of the shallow aquifer. *Rendiconti Online Della Società Geologica Italiana*, *48*, 2–9. https://doi.org/10.3301/ROL.2019.30

Levintal, E., Huang, L., Prieto García, C., Coyotl, A., Fidelibus, M. W., Horwath, W. R., Mazza Rodrigues, J. L., & Dahlke, H. E. (2023). Nitrogen fate during agricultural managed aquifer recharge: Linking plant response, hydrologic, and geochemical processes. *Science of The Total Environment*, *864*, 161206. https://doi.org/10.1016/j.scitotenv.2022.161206

Levintal, E., Kniffin, M. L., Ganot, Y., Marwaha, N., Murphy, N. P., & Dahlke, H. E. (2023). Agricultural managed aquifer recharge (Ag-MAR)—a method for sustainable groundwater management: A review. *Critical Reviews in Environmental Science and Technology*, *53*(3), 291–314. https://doi.org/10.1080/10643389.2022.2050160

Margat, J., & van der Gun, J. (2013). *Groundwater around the World: A Geographic Synopsis*. CRC Press / Balkema. https://doi.org/10.1201/b13977

Mekonnen, M. M., & Hoekstra, A. Y. (2016). Four billion people facing severe water scarcity. *Science Advances*, *2*(2), e1500323. https://doi.org/10.1126/sciadv.1500323

Mualem, Y. (1976). A new model for predicting the hydraulic conductivity of unsaturated porous media. *Water Resources Research*, *12*(3), 513–522. https://doi.org/10.1029/WR012i003p00513

Negri, C., Chiaradia, E., Rienzner, M., Mayer, A., Gandolfi, C., Romani, M., & Facchi, A. (2020). On the effects of winter flooding on the hydrological balance of rice areas

in northern Italy. *Journal of Hydrology*, *590*, 125401. https://doi.org/10.1016/j.jhydrol.2020.125401

Neto, D. C., Chang, H. K., & Van Genuchten, M. Th. (2016). A Mathematical View of Water Table Fluctuations in a Shallow Aquifer in Brazil. *Groundwater*, *54*(1), 82–91. https://doi.org/10.1111/gwat.12329

Nimmo, J. R., Schmidt, K. M., Perkins, K. S., & Stock, J. D. (2009). Rapid Measurement of Field-Saturated Hydraulic Conductivity for Areal Characterization. *Vadose Zone Journal*, *8*(1), 142–149. https://doi.org/10.2136/vzj2007.0159

Odell, B. P., Groenevelt, P. H., & Elrick, D. E. (1998). Rapid Determination of Hydraulic Conductivity in Clay Liners by Early-Time Analysis. *Soil Science Society of America Journal*, *62*(1), 56–62. https://doi.org/10.2136/sssaj1998.03615995006200010008x

Oki, T., & Kanae, S. (2006). Global Hydrological Cycles and World Water Resources. *Science*, *313*(5790), 1068–1072. https://doi.org/10.1126/science.1128845

Regione Lombardia. (2022). *Database Topografico (DBCDT) – Tratti Idrici e Reticolo Idrico Regionale*. Direzione Generale Territorio e Sistemi Verdi, Geoportale della Lombardia. https://www.geoportale.regione.lombardia.it/

Regione Lombardia & ARPA Lombardia. (2016). *Piezometria dell'Acquifero Superficiale della Pianura Lombarda (PTUA 2016 – WIZ_U32WG_TL_PZ_201405_S)*. Direzione Generale Territorio e Sistemi Verdi & Geoportale della Lombardia. https://www.geoportale.regione.lombardia.it/

Regione Piemonte. (2018). *Aggiornamento del Piano di Tutela delle Acque—Monografia MP1: Pianura Novarese*. Direzione Ambiente, Governo e Tutela del Territorio, Settore Tutela delle Acque, Regione Piemonte.

https://www.regione.piemonte.it/web/sites/default/files/media/documenti/2018-11/mp1_pianura_novarese_0.pdf

Regione Piemonte & IPLA. (2017). *Carta dei Suoli del Piemonte in scala 1:50.000*. Istituto per le Piante da Legno e l'Ambiente & Geoportale Piemonte. https://www.geoportale.piemonte.it/

Reynolds, W. D., & Elrick, D. E. (1990). Ponded Infiltration From a Single Ring: I. Analysis of Steady Flow. *Soil Science Society of America Journal*, *54*(5), 1233–1241. https://doi.org/10.2136/sssaj1990.03615995005400050006x

Rodríguez-Escales, P., Canelles, A., Sanchez-Vila, X., Folch, A., Kurtzman, D., Rossetto, R., Fernández-Escalante, E., Lobo-Ferreira, J.-P., Sapiano, M., San-Sebastián, J., & Schüth, C. (2018). A risk assessment methodology to evaluate the risk failure of managed aquifer recharge in the Mediterranean Basin. *Hydrology and Earth System Sciences*, *22*(6), 3213–3227. https://doi.org/10.5194/hess-22-3213-2018

Scarabel, L., Cenghialta, C., Manuello, D., & Sattin, M. (2012). Monitoring and Management of Imidazolinone-Resistant Red Rice (Oryza sativa L., var. Sylvatica) in Clearfield® Italian Paddy Rice. *Agronomy*, *2*(4), 371–383. https://doi.org/10.3390/agronomy2040371

Sethi, R., & Di Molfetta, A. (2019). *Groundwater Engineering: A Technical Approach to Hydrogeology, Contaminant Transport and Groundwater Remediation*. Springer International Publishing. https://doi.org/10.1007/978-3-030-20516-4

Siebert, S., Henrich, V., Frenken, K., & Burke, J. (2013). *Global Map of Irrigation Areas Version 5*. Rheinische Friedrich-Wilhelms-University, Bonn, Germany / Food and Agriculture Organization of the United Nations (FAO).

https://www.fao.org/aquastat/en/geospatial-information/global-maps-irrigated-areas/latest-version/

Soil Science Division Staff. (2017). *Soil Survey Manual*. (Original work published U.S. Department of Agriculture)

Stetefeld, J., McKenna, S. A., & Patel, T. R. (2016). Dynamic light scattering: A practical guide and applications in biomedical sciences. *Biophysical Reviews*, *8*(4), 409–427. https://doi.org/10.1007/s12551-016-0218-6

Sufyan, M., Martelli, G., Teatini, P., Cherubini, C., & Goi, D. (2024). Managed Aquifer Recharge for Sustainable Groundwater Management: New Developments, Challenges, and Future Prospects. *Water*, *16*(22), 3216. https://doi.org/10.3390/w16223216

Tanaka, M. (2023, November). *Measuring the Carbon Content in Fly Ash* [Application News]. Shimadzu Corporation.

Taramasso, M. A., Secco, E., Mellano, L., Gandolfo, M., Algarotti, P., Vigna, B., Fiorucci, A., Tosco, T., Sethi, R., & Casasso, A. (2025). Feasibility study of Managed Aquifer Recharge (MAR) in the areas of drainage trenches “fontanili” of the alluvial plain of Cuneo (NW Italy): First results from the SeTe-ALCOTRA project. *Rendiconti Online Della Società Geologica Italiana*, *67*, 44–53. https://doi.org/10.3301/ROL.2025.23

Tosco, T. (2024a). *Managed Aquifer Recharge* [Lecture notes]. Politecnico di Torino.

Tosco, T. (2024b). *Transport and Fate of Chemical Substances in the Subsoil* [Lecture notes]. Politecnico di Torino.

Tosco, T. (2024c). *Water in the Subsoil: Key Concepts and Models* [Lecture notes]. Politecnico di Torino.

Tosco, T. (2025). *Aquifer and Soil Hydrodynamic Characterization* [Lecture notes]. Politecnico di Torino.

UNESCO. (2022). *The United Nations World Water Development Report 2022 – Groundwater: Making the Invisible Visible*. UNESCO. https://doi.org/10.54679/CAOS3862

Van Genuchten, M. Th. (1980). A Closed-form Equation for Predicting the Hydraulic Conductivity of Unsaturated Soils. *Soil Science Society of America Journal*, *44*(5), 892–898. https://doi.org/10.2136/sssaj1980.03615995004400050002x

Van Genuchten, M. Th., & Wierenga, P. J. (1976). Mass Transfer Studies in Sorbing Porous Media I. Analytical Solutions. *Soil Science Society of America Journal*, *40*(4), 473–480. https://doi.org/10.2136/sssaj1976.03615995004000040011x

Van Lear, M. (2024). *Soil texture calculator (MultiPoint Triangle version 100pt)* [Computer software]. USDA Natural Resources Conservation Service. https://www.nrcs.usda.gov/sites/default/files/2024-10/MultiPointTriangle_100pt_508.xlsx

Vörösmarty, C. J., McIntyre, P. B., Gessner, M. O., Dudgeon, D., Prusevich, A., Green, P., Glidden, S., Bunn, S. E., Sullivan, C. A., Liermann, C. R., & Davies, P. M. (2010). Global threats to human water security and river biodiversity. *Nature*, *467*(7315), 555–561. https://doi.org/10.1038/nature09440

White, I., & Sully, M. J. (1987). Macroscopic and microscopic capillary length and time scales from field infiltration. *Water Resources Research*, *23*(8), 1514–1522. https://doi.org/10.1029/WR023i008p01514

Wösten, J. H. M., Lilly, A., Nemes, A., & Le Bas, C. (1999). Development and use of a database of hydraulic properties of European soils. *Geoderma*, *90*(3–4), 169–185. https://doi.org/10.1016/S0016-7061(98)00132-3

Zhang, H., Xu, Y., & Kanyerere, T. (2020). A review of the managed aquifer recharge: Historical development, current situation and perspectives. *Physics and Chemistry of the Earth, Parts A/B/C*, *118–119*, 102887. https://doi.org/10.1016/j.pce.2020.102887